FRACTURE OF FERROELECTRIC MATERIALS

A Thesis
Presented to
The Academic Faculty

By

William Sumner Oates

In Partial Fulfillment

Of the Requirements for the Degree

Doctor of Philosophy in Mechanical Engineering

Georgia Institute of Technology

July, 2004

FRACTURE OF FERROELECTRIC MATERIALS

Approved:

Dr. Christopher S. Lynch, Chairman

Dr. D. Stefan Dancila

Dr. Sathya V. Hanagud

Dr. Marc E. Levenston

Dr. Jianmin Qu

Date approved: July 19, 2004

ACKNOWLEDGEMENT

This work would not have been completed without the support and guidance of several people over the course of completing my Ph.D. I would like to sincerely thank Dr. Christopher S. Lynch for his immense help in shaping this work. I am forever indebted for his contribution in influencing my career. I would also like to thank many colleagues at Darmstadt University for their support in this work and their hospitality during my many visits to their University. I thank Drs. Alain Kounga, Doru Lupascu, Jürgen Rödel, as well as Emil Aulbach for our many interesting discussions on material science as well as politics and life in general. I also gratefully acknowledge Drs. Jianmin Qu, Marc Levenston, D. Stefan Dancila, and Sathya Hanagud for serving on my committee. I sincerely thank my many colleagues in our mechanics of materials research group for their support and encouragement during my course of study.

Lastly and most importantly, I would like to thank God and my family. I could not have achieved this goal without their love and support. I thank my wife, son and both sets of parents for their role in helping me attain this goal.

TABLE OF CONTENTS

ACKNOWLEDGEMENT iii

LIST OF TABLES viii

LIST OF FIGURES x

SUMMARY xiv

CHAPTER I 1

INTRODUCTION 1

What Are Ferroelectric Materials? 3

Comparison of Ferroelectric Ceramics and Single Crystal Relaxors 8

Closure 12

CHAPTER II 13

FERROELECTRIC FRACTURE BEHAVIOR: LITERATURE REVIEW 13

Anisotropic Elasticity Techniques for Piezoelectric Fracture 16

Energy Release Rate and Crack Face Boundary Conditions 18

Microfracture 23

Fracture Characterization 26

Crack Kinetics in PZT 27

Anisotropic Fracture in Single Crystal PZN-4.5%PT 29

Closure 31

CHAPTER III 33

ANISOTROPIC ELASTICITY TECHNIQUES FOR PIEZOELECTRIC MATERIALS 33

Governing Equations 34

Material Property Considerations 39

Orthotropic Rescaling for Piezoelectric Materials 41
Stress Governing Equations 41
Electrical Field and Electric Displacement Governing Equations 46
Stroh's Formalism 48
Fracture Problem 52
Orthotropic Rescaling Details 54
Stress Fields 54
Electric Displacement Fields 56
Stroh Approach 60
Comparison of Results 63
Conclusions 71
CHAPTER IV 73
MICROFRACTURE OF PIEZOELECTRIC MATERIALS UNDER ELECTRIC FIELD 73
Piezoelectric Microfracture 74
Elliptic Piezoelectric Inclusion Subjected to Remote Loading 77
Governing Equations and Useful Identities 77
Piezoelectric Inclusion 83
Piezoelectric Weight Functions 89
Crack Face Boundary Conditions 92
Numerical Results 95
Discussion 102
Conclusions 104

CHAPTER V 106
SUBCRITICAL CRACK GROWTH IN FERROELECTRIC CERAMICS 106
Measurement Procedure 106
Electrical Boundary Conditions 109
Relative Humidity 109
Results and Discussion 112
General Observations 112
Electrical Boundary Conditions 114
Relative Humidity 117
Conclusions 119
CHAPTER VI 120
ANISOTROPIC FRACTURE OF FERROELECTRIC SINGLE CRYSTALS 120
Experimental Methods 121
Crack Opening Profile Measurements 121
R-Curve Measurement Technique 122
Experimental Results 127
Crack Tip Toughness 127
SEVNB Measurements 127
Analysis 131
Crystal Anisotropy 131
Fracture Mechanics 135
Discussion 141
Conclusions 143

CHAPTER VII 144
Conclusions 144
Open Issues 147
APPENDIX A 149
Plane strain coefficients 149
Stroh eigensolution 150
APPENDIX B 153
SEVNB angled Crack Geometric Functions 153
REFERENCES 155

LIST OF TABLES

Table 3.1: Piezoelectric material properties (plane strain coefficients) used to plot stress fields using the orthotropic rescaling technique. The material coefficients (s_{66}^{D}, g_{16}, and β_{11}^{σ}) have been adjusted to meet the necessary ratios given by the decoupling coefficient and $\rho' = 1$. The decoupling ratio has been given for the plane strain case. 64

Table 3.2: Material properties related to the coefficients in Table 3.1 which are used to calculate stress fields using the Stroh formalism. The material coefficients (c_{66}^{E}, e_{16} and $\kappa_{11}^{\varepsilon}$) correspond to the boldface coefficients that were adjusted in Table 3.1.... 65

Table 4.1: Material properties used in evaluating microfracture under applied electric fields. The matrix properties are assumed to possess 48% $PbZrO_3$ and the inclusion contains 52% $PbZrO_3$. Permittivity of free space is defined by κ_o 96

Table 5.1: Test matrix for the v-K measurements conducted on poled and unpoled PZT compact tension specimens. 112

Table 5.2: Measurement uncertainty using a linear regression model in log space for the power law dependence, $v(K) = AK^n$. 114

Table 6.1: Comparison between the elastic tensor at constant electric field in PZN-4.5%PT single crystal. The elastic coefficients are given in GPa units, the piezoelectric coefficients (pm/V), and the dielectric coefficients are multiplied by permittivity of free space, ε_o. The orthorhombic material properties have been rotated by 45° around [001] to directly compare with the tetragonal case, (Yin and Cao 2002). 134

Table 6.2: Irwin matrix computed for *mm2* and *4mm* crystal symmetry properties is given in Table 4.2. The units are N, mm, MV. The Irwin matrix for the poled material was computed using open circuit elastic coefficients, while the short circuit modulus was used for the unpoled specimens. 140

Table 6.3: Comparison of the global critical energy release rate for PZN-4.5%PT assuming pseudo-tetragonal crystal symmetry (*4mm*) and effective orthorhombic symmetry (*mm2*). The units are given in N/m. 141

Table B1: Geometric functions determined using FRANCD2D for the 45° crack orientation in the SEVNB specimens..... 154

LIST OF FIGURES

Figure 1.1: Schematic of the phase transformation at the unit cell level for lead titanate ($PbTiO_3$) from cubic (left) to tetragonal (right). T_c is the Curie temperature. The unit cell extends along the c-direction and contracts in the two orthogonal directions. A spontaneous polarization is induced as the titanium ion shifts from the central location. 4

Figure 1.2: Relevant length scales in unpoled ferroelectric ceramics. 6

Figure 1.3: Schematic of ferroelectric and ferroelastic switching at the unit cell level (tetragonal crystal structure) from applied electric field and stress. 7

Figure 1.4: Crystal structure and polarization variants representing the rhombohedral phase of PZN-4.5%PT. (a) the unpoled state with eight variants, (b) resulting four polarization variants from [001] electric field loading, (c) two variant state from [110] electric field loading, (d) single variant state from [111] electric field loading. The dotted arrow represents the applied electric field (E_a) and corresponding poling direction for each crystal cut. 10

Figure 2.1: Process zone evolution from mechanical loading in ferroelectric ceramics. The gray region in (a) is the initial process zone at the onset of fracture. As the crack propagates forward, a residual stress zone develops in the crack wake which shields the crack tip from external loading. For constant velocity crack propagation, the load is continuously increased until the wake affects saturate leading to steady-state toughness. 15

Figure 2.2: Impermeable crack face boundary conditions where ω_+^∞ and ω_-^∞ are the positive and negative applied surface charges. Under electrical loading, (a) assumes zero surface charge on the crack face. From linear superposition, (b) gives the uniform electric displacement and electric field and (c) gives the contribution to the K-field. 21

Figure 2.3: Permeable crack face boundary conditions, where ω_+^c and ω_-^c is the positive and negative surface charge on the crack face given by a non-conducting fluid.

From linear superposition, (c) gives a lower contribution to the K-field relative to the impermeable crack. 22

Figure 3.1: Crack geometry used in the contour plots. A crack length of 2c=10 mm, constant radius of 100 μm around the crack tip are used in all plots. 53

Figure 3.2: Stress contour around the crack tip for the maximum principal stress, σ_1, from $\theta = \pi$ to $\theta = -\pi$ when r=100 μm when rescaling conditions are met. 67

Figure 3.3: Resulting stress contour for the maximum principal stress, σ_1, when the actual material parameters are used; $\theta = \pi$ to $\theta = -\pi$ when r=100 μm. 68

Figure 3.4: Parametric study describing the effects of the decoupling ratio on the maximum principal stress (σ_1) near the crack tip when K_{IV}= 0.002 $C/m^2\sqrt{m}$. The decoupling ratio, $\beta_{11}^{\sigma}/\beta_{22}^{\sigma}$, was modified while holding the piezoelectric coefficients constant. 69

Figure 3.5: Vector plot of electric displacement for TRS600 material properties under Mode I and Mode IV loading (K_I= 1 $MPa\sqrt{m}$, K_{IV}= 0.001 $C/m^2\sqrt{m}$). The solutions are practically identical. The Stroh formalism is shown by dotted arrows; the orthotropic rescaling result is shown by solid arrows. 71

Figure 4.1: Piezoelectric microfracture problem model using an inhomogeneous elliptic inclusion. A crack of outer radius c (c>a) extends from the inclusion edge. 75

Figure 4.2: Linear superposition of the field components applied along the crack face. The superscript *o* on the stress and electric displacement refers to the field solution from the inclusion problem. Charges must also be applied to the crack face although not shown. 76

Figure 4.3: Piezoelectric elliptical inclusion problem. The inclusion and matrix contain differing piezoelectric material properties. Arbitrary electro-mechanical loading is represented by some far-field change in electric potential $(\phi_+^{\infty} - \phi_-^{\infty})$ and traction $\mathbf{t}^{\infty}$ boundary conditions. 78

Figure 4.4: Normalized Mode I stress intensity factor vs. relative crack length given in Figure 4.1. The external loading consists of constant mechanical loading σ_{22}^{∞} while varying the electric field E_2^{∞}. 97

Figure 4.5: Driving force for crack propagation relative to crack length for the impermeable crack. Only electrical loading is considered. The applied energy release rate is always less than zero. 99

Figure 4.6: Driving force for crack propagation under electrical loading for the permeable crack. The applied energy release rate gives a positive driving force near the inclusion. 100

Figure 4.7: Change in energy release rate when the piezoelectric coefficients are varied in the inclusion. The coefficients were varied from 75% to 125% from the tabulated values given in Table 4.1. An electric field of 1 MV/m was used. 101

Figure 4.8: Effect of aspect ratio (b/a) on the critical inclusion size for cracks to form under an electric field of 1 MV/m. 102

Figure 5.1: Custom design loading frame used to characterize subcritical crack growth in PZT PIC 151. Label (1) is the compact tension specimen, label (2) is the load cell, and label (3) is a piezoelectric stack actuator used to load the specimen. The outer casing was used to control the environmental conditions. 108

Figure 5.2: Sealed container and microscope set-up used to characterize environmental sensitivity on the contact tension specimens. Argon flowed through the device to control the relative humidity. 111

Figure 5.3: This graph quantifies the method to obtain a steady state process zone. The crack was made to propagate at a constant velocity up to the point where this did not require changes in applied stress intensity factor. Each new chosen velocity required attainment of a new steady state process zone. The data represents toughening behavior measured during a v-K measurement on one unpoled PZT compact tension specimen exposed to ambient laboratory conditions (T=23°C and RH=35%). 113

Figure 5.4: Crack velocity curves for poled (thickness direction) PZT compact tension specimens exposed to open and short circuit boundary conditions (T=23°C and RH=35%). Regression curves are provided as fits through the data. 115

Figure 5.5: Crack velocity curves for unpoled PZT compact tension specimens exposed to ambient laboratory conditions (T=23°C and RH=35%) and "dry" air conditions (T=23°C and RH≅0.02%). The "dry" air specimens and one ambient specimen were heat treated at 400°C before testing. Regression curves are fit through the data. . 118

Figure 6.1: Configuration of the single crystal and Vickers indentation orientation used in quantifying the crack tip toughness and local energy release rate. The diagonals of the Vickers indentation were aligned along the [110] and [100] directions. 122

Figure 6.2: Four point loading device used in conducting fracture experiments on PZN-4.5%PT. The specimen is preloaded with a mechanical screw located underneath the piezoelectric stack actuator. The stack actuator controls the load applied to the bend bar. 124

Figure 6.3: Experimental set-up for the SEVNB method. The four point bending device was placed on its side to view crack propagation in the bend bar specimens under the optical microscope using transmitted polarized light. 124

Figure 6.4: Finite element model used in determining the stress intensity factors K_I and K_{II} under four point bending. 126

Figure 5.5: Scanning electron micrographs of Vickers indentations in PZN-4.5%PT single crystals. A 9.8 N load was applied to the indentation in (a) with the diagonal aligned in the [100] direction. In (b), a 4.9 N load was applied with the diagonals aligned in the [110] direction. 127

Figure 6.6: PZN-4.5%PT poled single crystal SEVNB specimen with a crack formed at 45° ([110] plane). 128

Figure 6.7: Unpoled PZN-4.5%PT single crystal SEVNB specimen with a crack formed at 0° ([010] plane). 129

Figure 6.8: Mode I fracture resistance for SEVNB PZN-4.5%PT single crystal specimens. The angle represents the direction of crack propagation. The data includes two poled and one unpoled specimen with cracks growing at an angle of 45°. One poled and unpoled specimen formed cracks that propagated at 0°..... 130

Figure 6.9: Mode II fracture resistance for SEVNB PZN-4.5%PT single crystal specimens. The data includes the two poled and one unpoled specimen previously shown in Figure 5.8 with cracks growing at an angle of 45°..... 131

Figure 6.10: Crack profile predictions for pseudo-tetragonal (4mm) and effective orthorhombic (mm2) material properties under the same K_I. A large difference was observed between the anisotropic material properties and the isotropic solution due to the difference in the shear modulus. 137

Figure 6.11: Crack tip toughness (K_{tip}) prediction using Stroh's formalism. The Vickers indentation diagonals were aligned in the [110] direction in specimen 1 and in the [100] direction in specimen 2. K_{tip} was predicted to be 0.46 $MPa\sqrt{m}$ assuming mm2 symmetry and 0.52 $MPa\sqrt{m}$ assuming 4mm symmetry. 138

SUMMARY

In this dissertation, the fracture mechanics of ferroelectric materials is evaluated by employing several analytical techniques and experimental methodologies. The theoretical work is focused on linear piezoelectric coupling that accounts for the influence of anisotropy and heterogeneity on fracture. The experimental section describes how environmental effects and electric boundary conditions influence fracture in the ferroelectric ceramic, lead zirconate titanate (PZT). Additionally, characterization of crack tip toughness and toughness from external loads in single crystal ferroelectric relaxor PZN-4.5%PT is given.

A new orthotropic rescaling technique is presented that solves the anisotropic linear elastic piezoelectric crack problem. The new technique rescales the coordinate system in a way that allows isotropic elasticity solutions to be applied to anisotropic piezoelectric materials. The asymptotic field components in poled piezoelectric materials are determined explicitly in terms of material properties. A certain ratio of piezoelectric and dielectric material properties are found to decouple stress concentrations generated from applied electric fields near the crack tip. The solution technique is validated using a different anisotropic elasticity technique called Stroh's formalism. Recommendations for when and when not to use the orthotropic rescaling are discussed.

The effects of heterogeneities on microfracture of piezoelectric materials are analyzed by implementing a crack at the edge of a heterogeneous piezoelectric inclusion. The difference in PZT material properties between the matrix and inclusion were based on a 4% local variation in the Zr / Ti ratio (Jaffe et al. 1971). Field concentrations from applied electric fields emanating from the inclusion are applied along the crack face using the piezoelectric weight function. It is determined that the impermeable and permeable crack face boundary conditions give significantly different driving forces for crack propagation under electric field loading. The model is compared to previous experimental results available in the literature on microscopic / macroscopic strain vs. electric field, composition variation, and microfracture.

The experimental investigations have focused on characterizing fracture toughness of ferroelectric ceramics (lead zirconate titanate—PZT) and ferroelectric relaxor single crystals (lead zinc niobate/lead titanate—PZN-4.5%PT). Subcritical crack growth in PZT was characterized using compact tension specimens (PZT 151, PI Ceramics, $Pb_{0.99}[Zr_{0.45}Ti_{0.47}(Ni_{0.33}Sb_{0.66})_{0.08}]O_3$). The experiments resulted in different fracture toughness under open or short circuit conditions and different relative humidity conditions. Single Edge V-Notch Beam (SEVNB) method was used to characterize fracture toughness of PZN-4.5%PT under four point bending. The measurements identified a weak cleavage plane in the [110] direction. The crack tip opening profile was measured from SEM micrographs on Vickers indentations to determine the crack tip toughness. This value was used to compute the local energy release rate (G_{tip}) and

compared to the global energy release rate (G_c) from SEVNB measurements. G_{tip} was found to be reasonably close to G_c along the weak cleavage plane.

CHAPTER I

INTRODUCTION

The performance of active materials has influenced technological advances over the past several decades. A considerable amount of attention has focused on exploiting the electro-mechanical coupling of piezoelectric materials to develop novel devices. Field coupled material properties provide an opportunity to develop innovative devices that are compact and efficient. Moreover, these type devices can eliminate complex mechanical designs by utilizing the multifunctional material capability.

The broad range of current ferroelectric device applications fall into three major categories: sensors, actuators, and transducers. The electromechanical constitutive behavior has afforded the potential for developing devices that range in size from the macro to nano scale. Macro scale device development has included morphing aircraft control surfaces (Mani et al. 2003; Oates 2001; Reich and Sanders 2003), vibration control (Cunefare and Graf 2002), structural health monitoring (Bechet 2003), and fuel injection (Christoffel 2002; Schuh et al. 2000). On the micro scale, recent research has lead to ferroelectric MEMS-based devices such as ultrahigh-density data storage (Cho et al. 2003), piezo-hydraulic energy harvesting devices for power generation (Roberts et al. 2000), microcantilevers for biosensing (Yi et al. 2003; Zhang et al. 2003) and nano-

positioning stages for atomic force microscopy (AFM) (Gruverman and Tokumoto 2001; Schneider et al. 2003).

Many applications have implemented ceramic lead zirconate titanate (PZT), which produces about 0.1% strain from an applied electric field of approximately 2 MV/m. PZT is difficult to grow in single crystal form. This has limited the progress in developing devices in applications where large strain and large charge generation is desired. Performance enhancement has been realized through the development of relaxor rhombohedral single crystal lead zinc niobate-lead titanate (PZN-PT) and lead magnesium niobate-lead titanate (PMN-PT). The actuation performance has increased by an order magnitude with minimal hysteresis. Experiments have shown that the crystal cut significantly affects the material response. The material is highly anisotropic with large piezoelectric coupling in certain directions, while other crystal cuts have only marginal piezoelectric coupling and large hysteresis (Liu et al. 1999).

The field coupling capability comes with added complexity of predicting material behavior under excessive loading, fatigue and hostile environments. Large electro-mechanical loading at high frequency is often required to compete with conventional high power applications which have impeded the progress of device implementation. This difficulty is in part due to a lack of understanding the material's failure mechanisms. In addition, the dramatic difference in size of a particular device (meters down to nanometers) requires knowledge of the critical failure mechanisms at several different length and time scales.

This dissertation extends the current state of the art in failure of ferroelectric ceramics and single crystals by focusing on critical mechanisms contributing to fracture. Theoretical development focuses on the influence of anisotropic electro-mechanical material properties and heterogeneities on the fracture behavior in ferroelectrics. The experimental section sheds light on the influence of electrical boundary conditions and relative humidity on the fracture behavior. Differences in toughening mechanisms observed in ferroelectric ceramics (PZT) and ferroelectric relaxor single crystals (PZN-4.5%PT) are assessed.

What Are Ferroelectric Materials?

Piezoelectric materials possess the ability to generate charge under applied stress. This material behavior was first discovered by J. Curie and P. Curie in 1880. The converse piezoelectric effect is defined by a shape change from applied voltage. It was later discovered that certain piezoelectric materials possess dielectric hysteretic behavior (Jaffe et al. 1971; Lines and Glass 1977; Valasek 1921). These type materials were classified as ferroelectric. The polarization reorientation observed during large electric field loading can also be generated from applied stress. This phenomenon is defined as ferroelastic behavior. Ferroelectric and ferroelastic behavior is typically highly coupled; therefore unless otherwise stated, the term *ferroelectric* will be used throughout the dissertation to describe materials possessing polarization reorientation from either applied electric field or stress.

Ferroelectric materials are predominately characterized by ionic bonds. The ions within the atomic lattice orient into a configuration that minimizes the internal energy. This orientation is strongly dependent on temperature and composition. Ferroelectric materials are paraelectric above the Curie temperature and ferroelectric below the Curie temperature. Slight changes in the composition near the morphotropic phase boundary can change the crystal structure into tetragonal, monoclinic, orthorhombic or rhombohedral phase. As the material cools, spontaneous strain and polarization form at the unit cell level as illustrated in Figure 1.1. For simplicity, the tetragonal phase of lead titanate is shown.

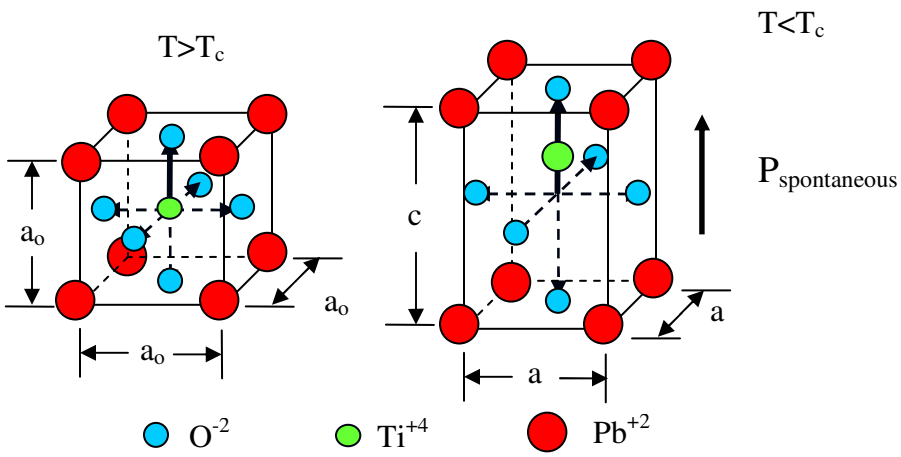

Figure 1.1: Schematic of the phase transformation at the unit cell level for lead titanate ($PbTiO_3$) from cubic (left) to tetragonal (right). T_c is the Curie temperature. The unit cell extends along the c-direction and contracts in the two orthogonal directions. A spontaneous polarization is induced as the titanium ion shifts from the central location.

The macroscopic electromechanical behavior in ferroelectric ceramics is the result of material behavior at several length scales. The ceramic consists of a conglomerate of randomly oriented grains that are fused together forming regions of continuous electric potential, mechanical displacement, and normal traction boundary conditions along the grain boundaries. To complicate matters, these boundaries may also have microcracks, pores, and foreign constituents (Tan and Shang 2002). Each grain has regions of like polarization called domains. The domains are separated by domain walls across which the spontaneous polarization is discontinuous. For tetragonal structures, domain walls may give rise to either 180° or 90° polarization orientations. The rhombohedral crystal structure gives rise to 71° or 109° domain walls. At one length scale lower, the unit cell previously shown in Figure 1.1 is found. A schematic of the relevant length scales are shown in Figure 1.2.

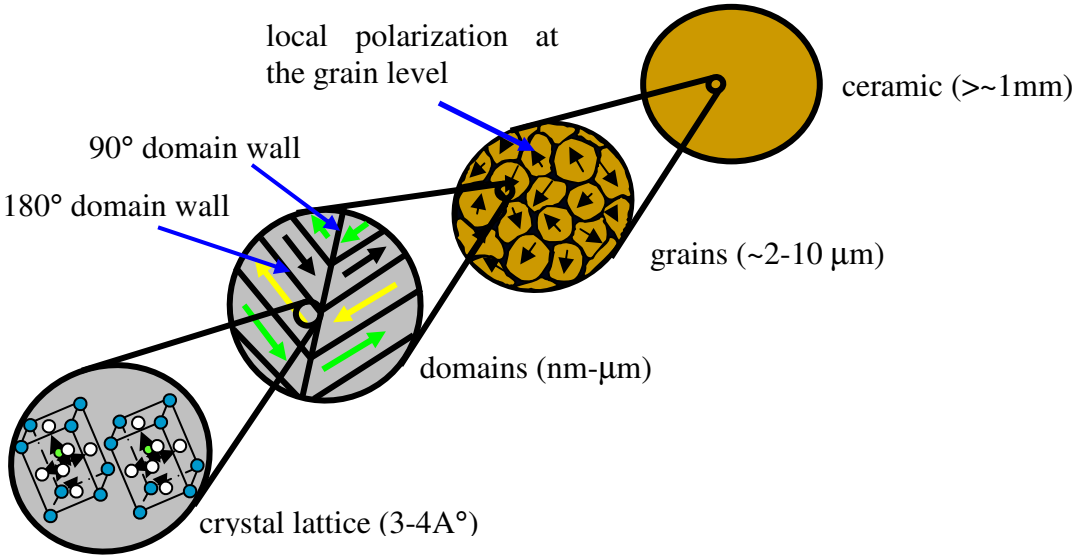

Figure 1.2: Relevant length scales in unpoled ferroelectric ceramics.

The phase transformation from paraelectric to ferroelectric results in a local domain structure with zero net polarization. The ferroelectric ceramic is isotropic elastic / dielectric with no piezoelectricity. When a large electric field that is above some coercive field is applied, domains contained within each grain partially align with the external electric field resulting in a net remanent polarization and strain. The polarization reorientation (ferroelectric switching) transforms the material from isotropic elastic / dielectric to a transverse isotropic material with piezoelectric coupling. A large stress can also drive polarization reorientation (ferroelastic switching). A large compressive stress parallel to the poling direction can significantly depolarize the material and practically eliminate the piezoelectric effect. A schematic of this behavior at the unit cell level is shown in Figure 1.3 again for tetragonal crystal structures.

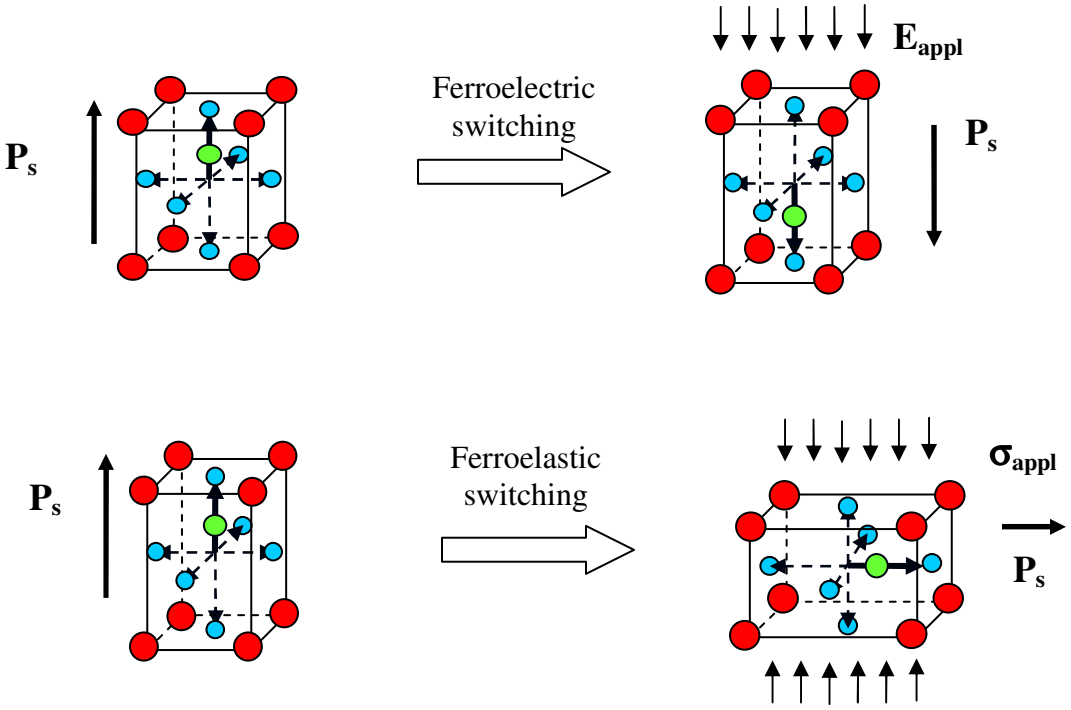

Figure 1.3: Schematic of ferroelectric and ferroelastic switching at the unit cell level (tetragonal crystal structure) from applied electric field and stress.

Ferroelectric switching results in the majority of the dipoles aligned with the external field. On the other hand, ferroelastic switching under compressive loading gives rise to an equal volume fraction of electric dipoles aligned approximately perpendicular to the compressive load. The amount of dipole reorientation depends on local residual effects (such as grain boundaries and free charge carriers) opposing polarization reorientation. Ferroelastic switching results in inelastic mechanical deformation (remanent strain) and significant reduction in polarization. Similar behavior takes place under large tensile loading, assuming the material does not fracture. In this case,

domains will switch to align with the tensile load in an alternating "up-down" orientation such that no remanent polarization is induced but remanent strain develops.

Comparison of Ferroelectric Ceramics and Single Crystal Relaxors

In the experimental section of this dissertation, the fracture toughnesses of the ferroelectric ceramic PZT and relaxor single crystal [001] cut PZN-4.5%PT are characterized. A comparison of the differences in the constitutive behavior of each material is first given to provide insight into the critical mechanisms affecting fracture.

Ferroelectric relaxor single crystals have recently received much attention due to their enhanced piezoelectric coupling and high efficiency relative to ferroelectric ceramics such as PZT (Park and Shrout 1997). The major distinction contributing to differences in constitutive behavior between ceramics and single crystals is the absence of grain boundaries in the latter. Domain formation and evolution within ferroelectric ceramics is more complex than the single crystal due to the complicated stress state contained within each grain. The complex heterogeneous material properties and localized stress/electric field state at the grain level are typically homogenized by some averaging scheme to obtain macroscopic material properties. An extensive number of theoretical analyses using micromechanics have addressed the heterogeneity issue in piezoelectric ceramics (Benveniste 1994; Dunn and Wienecke 1996; Hwang et al. 1998; Xiao and Bai 1999).

Grain boundaries inhibit the level of poling. In ceramic tetragonal $BaTiO_3$, the saturation polarization is about half the single crystal value (Moulson and Herbert 1990). To reduce this limitation, PZT is typically processed near the morphotropic phase boundary which results in a mixture of the tetragonal, rhombohedral and monoclinic A phases. There are six variants in the tetragonal crystal phase and eight variants in the rhombohedral structure. Additional variants exist in the monoclinic phase. This composition results in a more fully poled ceramic due to the increased number of variants. This typically leads to higher piezoelectric coupling.

The constitutive behavior has been well documented in the literature for PZT under uniaxial electro-mechanical loading. A good description of the typical macroscopic constitutive behavior based on 8/65/35 PLZT (6% lanthanum, 65% lead zirconate, 35% lead titanate) is given by Lynch (1996). Ferroelectric and ferroelastic switching is observed when the external electric field or stress reaches some coercive limit. Above this limit the material becomes linear / elastic dielectric. When the direction of the load changes, local switching can occur leading to macroscopic hysteretic behavior.

Ferroelectric relaxor single crystals are inherently free of grain boundary influences on the constitutive and fracture behavior. The constitutive behavior primarily depends on the crystal structure, domain orientation and loading direction. PZN-4.5%PT contains the rhombohedral phase below the Curie temperature (Noheda et al. 2002). In the unpoled state, the material consists of eight variants; each one pointed towards a corner of the unit cell. Each unit cell consists of one variant, but on a volume average all

eight variants exists in the material, although some combinations of adjacent variants can lead to incompatible states (Erhart and Cao 2003). The polarization variants for several crystal cuts and corresponding poling directions are shown in Figure 1.4.

The [001] crystal cut in PZN-4.5%PT has received the most attention due to its high piezoelectric coupling and minimal hysteresis. This configuration results in a stable engineered domain state after poling. As shown in Figure 1.4b, the poled state results in four variants partially aligned with the external field.

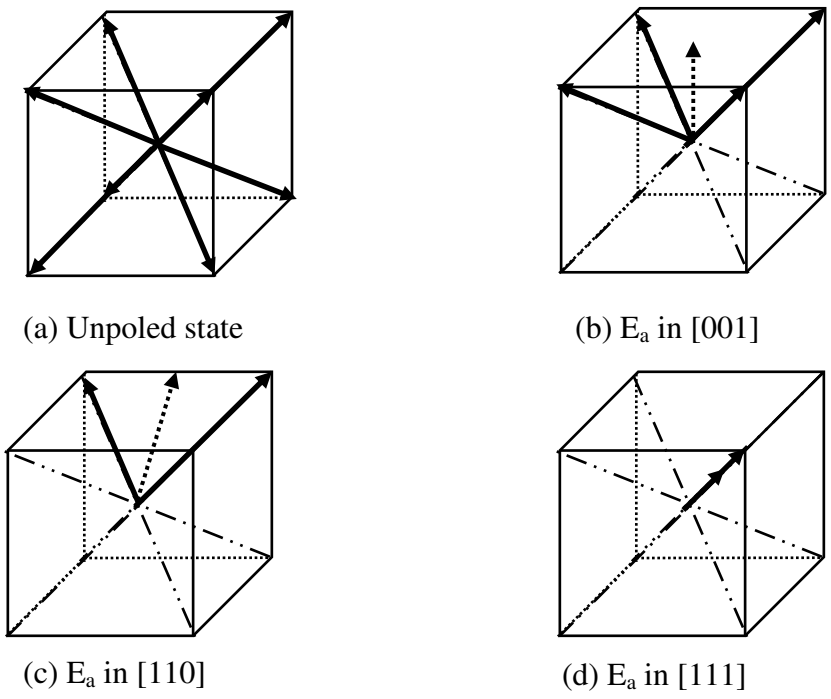

(a) Unpoled state (b) E_a in [001]

(c) E_a in [110] (d) E_a in [111]

Figure 1.4: Crystal structure and polarization variants representing the rhombohedral phase of PZN-4.5%PT. (a) the unpoled state with eight variants, (b) resulting four polarization variants from [001] electric field loading, (c) two variant state from [110] electric field loading, (d) single variant state from [111] electric field loading. The dotted arrow represents the applied electric field (E_a) direction.

A substantial amount of literature is available that describes the nonlinear constitutive behavior of PZN-4.5%PT under electric field loading (Liu and Lynch 2003; Noheda et al. 2002; Park and Shrout 1997) and others. It was observed that when the loading is above a certain electric field, the constitutive response becomes nonlinear suggesting a phase transformation occurred. Park and Shrout (1997) proposed a phase transformation from rhombohedral to tetragonal took place under large electric field loading in the [001] direction. In the work by Liu and Lynch (2003), the phase was assumed to transform from rhombohedral to orthorhombic since the electric field loading was in the [110] direction. In both cases, the phase transformation was observed to be unstable. During unloading, a minor hysteresis loop first developed and then returned to the same linear response at low field levels. Similar material behavior has been observed in single crystal PMN-32%PT (McLaughlin et al. 2004) under both electrical and mechanical loading.

In the [111] cut, a large electric field above some coercive field will orient all the polarization variants into a single domain state. This configuration results in large depolarization energy which creates an unstable state. The instability results in large hysteresis and lower piezoelectric coupling (Liu et al. 1999).

Closure

Ferroelectric materials continue to provide significant advantages in certain device applications due to large force generation and fast response time. These advantages can only be realized when reliability issues are addressed. To compete with conventional actuators and sensors, ferroelectric materials must be able to operate in hostile environments under long-term cyclic electro-mechanical loading. The brittle nature of ferroelectric materials requires an understanding of the critical mechanisms affecting fracture. The following chapter presents a review of the current knowledge of material reliability focusing on fracture of ferroelectric materials.

CHAPTER II

FERROELECTRIC FRACTURE BEHAVIOR: LITERATURE REVIEW

Although ferroelectric materials continue to find increasing use in actuator, sensor and transducer design, questions regarding lifetime and reliability remain a concern due to the inherent low fracture toughness and complex material behavior. The poling procedure required for use in device applications introduces anisotropy in elastic and dielectric coefficients as well as piezoelectric coupling between the mechanical and electrical fields. This introduces complex fracture behavior which necessitates advanced analytical techniques and fracture characterization.

Ceramic materials possess strong atomic bonds which limit plastic deformation and increase brittleness. Once the material is poled, the constitutive response can be approximated as linear under low drive regimes. This behavior allows linear elastic-dielectric fracture mechanics to be applied to ferroelectric materials by focusing on the piezoelectric coupling. Anisotropic elasticity techniques can be adopted to determine the K-fields in the linear regime. As the crack tip is approached, careful considerations of nonlinear ferroelectric and ferroelastic switching must be considered.

Although ferroelectric materials possess low fracture toughness, it was illustrated in Chapter I that these materials undergo inelastic deformation and irreversible

polarization reorientation. This can lead to R-curve behavior, which describes a functional dependence on toughness as the crack grows. The toughening mechanism in ferroelectric ceramics has been predominantly attributed to domain switching (Lucato et al. 2000). A process zone develops during loading. The size of the zone depends on the geometry, composition, loading, polarization direction, crack tip velocity, environment and various other parameters.

At the onset of crack propagation, the initial process zone reaches a critical limit and the crack tip moves forward. This splits the original process zone into two halves. A local compressive residual stress state is created in the crack wake from the misfit between the transformed region and the bulk material. This shields the new crack tip from the applied K-field. A larger external load is required for the crack to continue propagating at some constant velocity, hence higher toughness. This process is depicted in Figure 2.1. The toughness reaches a steady-state value when the wake effects relatively far from the crack tip no longer contribute to crack tip shielding. When an applied electric field is present, ferroelectric switching can change the size and shape of the process zone which will also affect toughness.

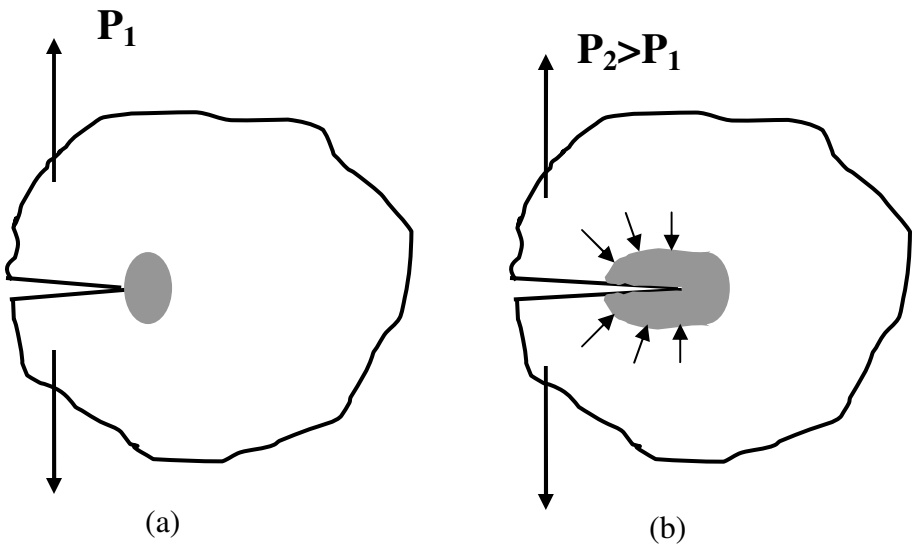

Figure 2.1: Process zone evolution from mechanical loading in ferroelectric ceramics. The gray region in (a) is the initial process zone at the onset of fracture. As the crack propagates forward (b), a residual stress zone develops in the crack wake which shields the crack tip from external loading.

Identification of the critical mechanisms contributing to fracture in ferroelectric materials is difficult due to the number of active coupled phenomena. These mechanisms include poling direction, crystal structure, phase transformations, residual stress, electrical boundary conditions, and environmental effects. These issues will be addressed in subsequent chapters using both theoretical and experimental methods. First, the current state of the art in ferroelectric fracture will be presented.

Anisotropic Elasticity Techniques for Piezoelectric Fracture

A substantial amount of theoretical work has helped form a theoretical framework for determining the field quantities near a crack tip in piezoelectric materials. An extensive number of analytical solutions have been developed using the Stroh formalism to solve anisotropic elasticity boundary value problems for piezoelectric materials (McMeeking 1999; Park and Sun 1995; Suo et al. 1992; Ting 1996; Zhang et al. 2001) and several others. When these analyses are applied to ferroelectric materials, a poled state is assumed and the nonlinear switching zone is limited to a highly localized region such that the small scale yielding assumption is valid. This is suitable in most cases for mechanical loading since the process zone is relatively small (~<1 mm), (Lupascu et al. 2001). Electric field loading must be limited to low field levels to avoid large scale ferroelectric switching.

Ting (1996) gave a thorough discussion of the mathematical relationships that form the Stroh formalism. He extended the theory beyond anisotropic elastic materials to include thermal and piezoelectric effects. Details of the elliptical inclusion problem are discussed. Suo et al. (1992) worked through the anisotropic field equations for the piezoelectric crack problem and determined the energy release rate for electro-mechanical loading. McMeeking (1999) evaluated stress and displacement fields in a compact tension geometry using Stroh's formalism and finite element analysis. The influence of crack opening profile on the electric field near the crack tip was considered.

The Stroh formalism relies on an eigenvector solution which represents the directions of both displacement and traction in the anisotropic solid. This relation can be extended to include electric displacement and electric field directions in piezoelectric materials. Although the Stroh eigenvectors represent the material properties, they are complex quantities that must be individually solved for each material by using a numerical routine. Explicit solutions of the anisotropic piezoelectric boundary value problem are desired to gain insight into how these properties may affect the fracture behavior.

An orthotropic rescaling technique has been adopted to explicitly solve the field components in terms of the electro-elastic material coefficients. Suo et al. (1991) determined the stress fields in elastic composite materials by employing the orthotropic rescaling technique. In orthotropic elastic solids, the coordinate axes are rescaled to obtain the biharmonic solution when a certain ratio of elastic coefficients equals unity. In the case of piezoelectric materials, an additional constraint is necessary. The identification of a certain ratio of piezoelectric and dielectric coefficients decouples the mechanical and electrical terms prior to rescaling the coordinate axes. When the decoupling ratio holds and the biharmonic equation is attained, an exact stress field solution is determined. It was also determined that when decoupling holds, the electric field and electric displacement can also be found in closed form by solving Poisson's equation (Lynch and Oates 2004).

Energy Release Rate and Crack Face Boundary Conditions

One of the building blocks for all brittle fracture theory is rooted in the concept of the *Griffith energy-balance*. Griffith applied reversible thermodynamics to model crack systems which required minimization of the total free energy of the system. An energy balance between mechanical and surface energy was proposed. Once the applied energy reaches twice the surface energy, the crack propagates. However, in 'real materials' irreversible processes are inevitable which requires modifications to the reversible thermodynamic concept. Additional work is required in this case to propagate the crack forward.

This concept can be extended to linear elastic-dielectric materials by considering the influence of electrical energy on the crack. Under electric field loading, piezoelectric coupling augments the stress field in front of the crack tip, while electric charge present on the crack surface tends to pull the crack shut. This complex material state is first described for crack systems containing isotropic elastic-dielectric material properties. When no piezoelectric coupling exists, the energy release rate can be represented in terms of the applied K and the elastic and dielectric material properties. For Mode I and Mode E (electric field intensity) in-plane strain, the following relation can be determined,

$$G = \frac{1-\nu^2}{E} K_I^2 - \frac{\kappa}{2} K_E^2 \qquad (2.1)$$

where E is the modulus, ν is the Poisson ratio, κ is the dielectric permittivity, K_I is the Mode I intensity factor, K_E is the electric field intensity. Obviously, electric loading provides a negative driving force since the dielectric permittivity is always greater than zero.

The energy release rate in piezoelectric materials is often determined using anisotropic elasticity. Stroh's formalism is frequently adopted to represent in the energy release rate in terms of an eigenvector solution. Once the eigenvectors are found, a real matrix representing material coefficients is used. This matrix is called the Irwin matrix (McMeeking 2003) and is given by,

$$\mathbf{H} = \frac{1}{2}\mathrm{Re}\left\{i\mathbf{A}\mathbf{B}^{-1}\right\} \tag{2.2}$$

H is a 3 X 3 matrix for two-dimensional deformation (neglecting anti-plane coupling) where the off-diagonal terms account for elastic-dielectric anisotropy and piezoelectric coupling. The imaginary number is given by $i = \sqrt{-1}$. Using indicial notation, the coefficient H_{33}, is related to the dielectric coefficients and is typically negative. This results in a similar negative electrical driving force in comparison to Equation (2.1). The matrices, **A** and **B**, are the Stroh eigenvectors which will be discussed in detail in subsequent chapters. They are related to material properties.

Using the Irwin matrix, the energy release rate can be determined by shrinking the piezoelectric elliptic hole solution down to a crack and determining the amount of work required for an infinitesimal increase in crack length, (Suo et al. 1992; Ting 1996). This results in the following relation,

$$G = \mathbf{k}^T \mathbf{H} \mathbf{k} \tag{2.3}$$

where $\mathbf{k}^T = \begin{bmatrix} K_{II} & K_I & K_{IV} \end{bmatrix}$ is the intensity factors for Mode II, Mode I and Mode IV, respectively. The Mode IV intensity follows common notation in the literature which defines the intensity in terms of electric displacement. This can be directly related to K_E through the piezoelectric constitutive law.

For mathematical simplicity, the electrical intensity (K_E and K_{IV}) in Equations (2.1) and (2.3) typically assume the crack face is impermeable. This is analogous to the mechanical case where zero traction boundary conditions on the crack face are assumed, but this assumption for electrical boundary conditions is in violation of electrostatics. The normal component of electric displacement must be continuous across an interface when free charge density is zero (Panofsky and Phillips 1962). Impermeable crack face conditions assume the electric displacement normal to the crack face is zero which creates a jump in electric displacement just underneath the crystal surface. It provides the largest negative driving force for crack propagation and is not physically realistic since a

field can be present even in a vacuum. This is elucidated by considering the center crack panel illustrated in Figure 2.2. By linear superposition, the total fields can be described by a uniform part (b) and the field intensity part (c). The charge at the external boundary is distributed along the crack face in (c). The negative and positive charges tend to pull the crack shut which provides a negative driving force which resists crack growth.

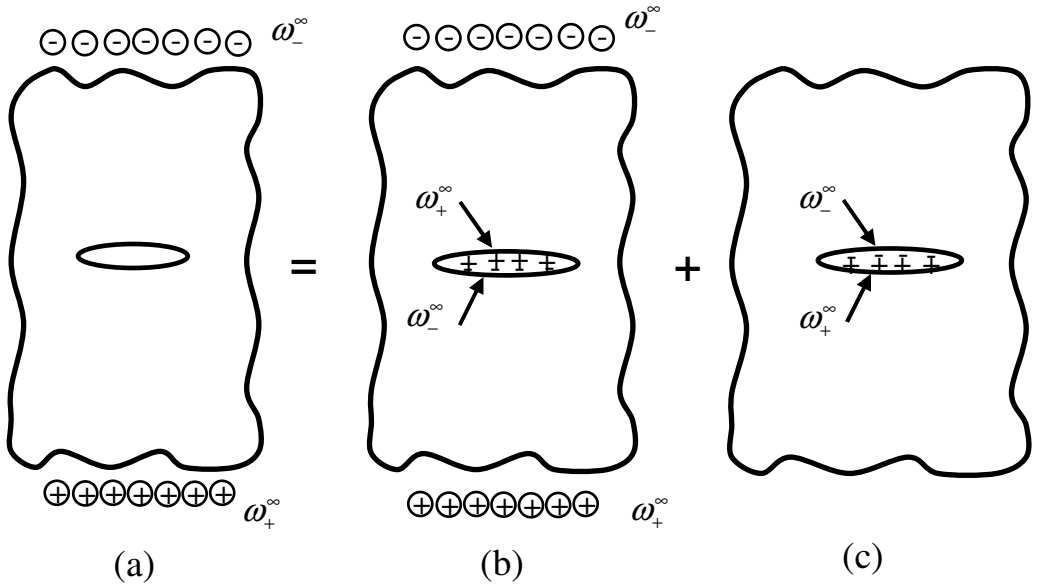

Figure 2.2: Impermeable crack face boundary conditions where ω_+^∞ and ω_-^∞ are the positive and negative applied surface charges. Under electrical loading, (a) assumes zero surface charge on the crack face. From linear superposition, (b) gives the uniform electric displacement and electric field and (c) gives the contribution to the K-field.

In real materials, the cracked region contains some non-conducting fluid such as gas or silicone oil that is at least able to sustain a small electric displacement. Even in the case of a vacuum, the volume within the crack can contain an effective electric displacement of $\kappa_o E_2$ where κ_o is the permittivity of free space. This reduces the amount

of charge capable of pulling the crack shut and reduces the negative driving force, see Figure 2.3.

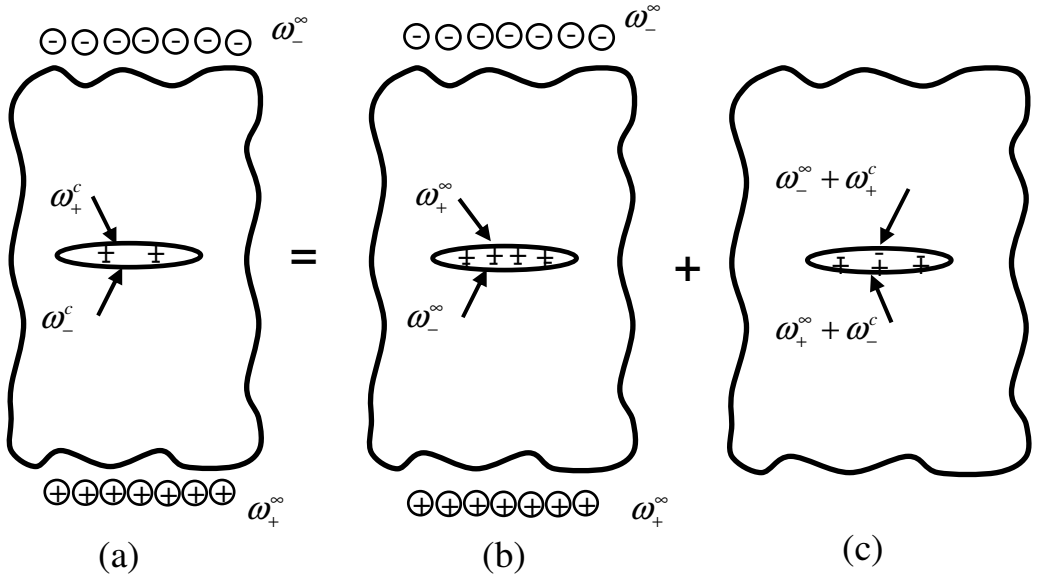

Figure 2.3: Permeable crack face boundary conditions, where ω_+^c and ω_-^c are the positive and negative surface charges on the crack face given by a non-conducting fluid. From linear superposition, (c) gives a lower contribution to the K-field relative to the impermeable crack.

A more accurate electric displacement intensity factor (K_{IV}) for the permeable crack requires determining the free charge present in the interior of the crack volume. This can be achieved by solving the boundary value problem for the crack geometry in terms of the unknown electric displacement in the crack interior. The change in potential and crack opening profile is first determined which leads to the electric field developed inside the crack. If the permittivity in the crack volume is known, the electric

displacement can then be determined. This is a simplified approach that neglects several contributions that may be present. Complications arise in real materials due to asperities, electrostatic discharge and nonlinear Maxwell stresses (Kamlah 2001; Maugin and Epstein 1991). Approximations to the boundary conditions along the crack face have been previously considered (Hao and Shen 1994; McMeeking 1999). This technique will be discussed in more detail in Chapter IV on microfracture.

Microfracture

Microstructural variables present in ferroelectric ceramics interact with incipient crack formation and growth. The attendance of heterogeneities in elastic, thermal expansion, and piezoelectric coefficients at the grain level can affect localized stress and electric fields. To complicate matters, these materials are anisotropic and undergo phase transformations from paraelectric cubic to ferroelectric tetragonal, rhombohedral, orthorhombic, or monoclinic. Techniques that account for localized anisotropic heterogeneities near cracks are important to guard against fatigue and failure.

Previous theoretical and experimental work has led to reasonable predictions of the critical grain size for fracture in single phase elastic polycrystals (Cleveland and Bradt 1978; Evans 1978; Rice and Phohanka 1978) and others. High thermal expansion anisotropy has been shown to influence microcracking along grain boundaries in several brittle ceramics. Microcrack formation is more prevalent in large grain-size materials. An energy based model was developed by Cleveland and Bradt (1978) to predict spontaneous microcracking in pseudobrookite oxides. Similar work was carried out by

Rice and Phohanka (1978) by comparing three different energy based and stress based models. The work was extended to include grain orientation and facet size effects to determine the maximum stress intensification at boundary located defects (Evans 1978).

In ferroelectric materials, experimental results and theoretical modeling of microcracking in ferroelectric ceramics have led to a stronger understanding of how piezoelectric coupling affects the microfracture process. Jiang et al. (1994) characterized electric fatigue in PLZT 7/68/32 (mole ratio of La/Zr/Ti) under bipolar electric fields. Both intergranular and transgranular fracture were observed. An energy based model similar to the thermal expansion models was extended to piezoelectric materials by approximating the strain energy through certain piezoelectric coefficients. Reasonable predictions on critical grain size relative to fatigue were determined. Lynch (1998) applied Vickers indentations to two compositions of PLZT (8/65/35 ferroelectric and 9.4/65/35 relaxor). Static electric fields perpendicular to the crack increased crack growth in the ferroelectric composition. An energy balance based on surface energy, irreversible ferroelastic twinning, and residual stress lead to a description of the energy release rate. The residual stress was not quantified, although the final result suggested larger grain size would lead to spontaneous microfracture. Based on Lynch's model, the critical grain diameter was,

$$d_c = \frac{E}{\sigma_R^2}\left(2\gamma_S + \frac{\gamma_t}{1+n}\right) \tag{2.4}$$

where E is the Young's modulus, σ_R is the residual stress, γ_S is the surface energy, γ_t is the work done in ferroelastic twinning, and *n* is the area increase of microcracks in front of the macro crack.

Recent work by Hoffman et al. (2001) characterized microstructural properties in lead zironate titanate. Three compositions were prepared to compare the strain vs. electric field behavior at the macroscopic and microscopic levels in different ferroelectric phases. The compositions contained the rhombohedral phase (Zr/Ti-60/40), tetragonal phase (Zr/Ti-54/46) or morphotropic (Zr/Ti-45/55). High resolution X-ray diffraction measurements showed over a 40% change in the local piezoelectric coupling between the rhombohedral and tetragonal phases. Similar results were found from macroscopic measurements.

Additionally, they observed local material property variations in SEM micrographs of the morphotropic PZT composition. Material property variations were on the length scale of grains (1.8-3.3 μm). Different crystal structures were determined from domain formation. Compositions rich in $PbTiO_3$ tend to form 90°/180° domain walls (tetragonal phase) while compositions rich in $PbZrO_3$ tend to form 71°/109° domain walls (rhombohedral phase). This gives a strong indication that microcracking from material inhomogeneities is possible; however it was pointed out that the amount of heterogeneity in the specimens may have been above normal.

Chapter IV extends the current work on residual stress influences on fracture of piezoelectric materials by evaluating flaw-localized driving forces from inhomogeneities. The interaction between an piezoelectric elliptic inclusion and an edge crack is developed. Changes in intensity factors and energy release rate are determined for a certain fluctuation in piezoelectric material properties between the material and inclusion.

Fracture Characterization

An extensive amount of experimental work can be found in the literature on fracture of ceramic ferroelectric materials. A large amount of fracture experiments have been conducted using Vickers indentations (Lynch 1998; Wang and Singh 1997; Weitzing et al. 1999). A number of experiments have been conducted using a four point bend apparatus (Chen et al. 2001; Karastamatis et al. 2002), a double torsion technique (McHenry and Koepke 1983) and compact tension device (Kolleck et al. 2000; Lucato et al. 2000). Wang and Singh (1997) observed that positive electric fields in poled piezoelectric material (PZT EC-65) generated shorter cracks perpendicular to the applied electric field than negative electric fields. The cracks were created using Vickers indentations. Tobin and Pak (1993) evaluated PZT-8 under similar experimental conditions and observed opposite trends in fracture toughness.

Although a good understanding of the effects of electric field on the fracture behavior has not yet been developed, considerable progress has been made toward determining the complexities of R-curve behavior in ferroelectric ceramics. As previously mentioned, polarization direction (Lucato et al. 2000) and electrical boundary

conditions (Förderreuther et al. 2002; Kolleck et al. 2000; Oates et al. 2004) next to crack velocity (Lucato 2003) have been shown to affect R-curve behavior.

Crack Kinetics in PZT

Crack kinetics or subcritical crack growth is defined as crack propagation at measurable velocities (m/s to ~nm/s) where inertial affects are considered negligible. Crack propagation normally occurs in chemically interactive environments which often lead to materials failing under lower stress intensity than the K_{Ic} value. In ferroelectric ceramics, subcritical crack growth is sensitive to applied load, environment, electrical boundary conditions and other extraneous variables. Characterization of crack kinetics in ferroelectric materials is critical to develop reliable actuators and sensors exposed to various environmental conditions.

A reasonable amount of data on environmental effects of subcritical crack growth in soda-lime—silica glass can be found in the literature (Wiederhorn et al. 1982; Wiederhorn et al. 1980). Wiederhorn characterized how relative humidity affects crack-growth rates in soda-lime glass. The velocity vs. applied stress intensity curves (v-K curves) were broken down into three distinct regions. It was suggested that in region I (lowest velocity region) the crack propagation rates were driven by both stress intensity and chemical reactions at the crack tip. In region II, the rate of transport of water molecules to the crack tip was the driving factor for crack propagation. In region III (upper velocity region), stress intensity was the key factor in determining crack-growth rates.

Extensive discussion of the effects of chemistry on crack kinetics has been summarized by Lawn (1975). Silicate glasses possess an open network structure that allows water molecules to penetrate the crack tip leading to strong chemical interactions from the lack of steric barriers. Crystal structure plays a significant role in shielding chemical reactions based on the amount of crystal lattice strain allowable relative to the size of the water molecule. When ferroelectricity is present, the strong electrical interaction can influence water molecules approaching the crack tip. This requires careful considerations of material-environment systems in electro-mechanical coupled materials.

Limited data is available for environmental effects on subcritical crack growth in ferroelectric material. The author is only aware of two sources that have explored these effects. Van der Laag et al. (2002) observed a sharp decrease in fracture toughness between 2 and 10% relative humidity in PZT at several different crack velocities using Single Edge Notched Beam (SENB) specimens. Freiman et al. (1974) measured v-K relations for PZT 5800 and observed an order of magnitude increase in velocity for each stress intensity measured when the material was submersed in liquid water in comparison to 40%RH.

An inadequate amount of fracture data is currently available that isolates the effects of open and short circuit boundary conditions. Tensile strength measurements were published by Fett et al. (2000) on open and short circuit boundary conditions for poled ceramics. Specimens of dimension 3 x 4 x 45 mm^3 were poled in the 3 mm

direction and loaded in the 45 mm direction. Limited success was obtained for open circuit boundary conditions due to specimen failures near the grips. It was proposed that short circuit boundary conditions would lead to more domains switching, which would increase toughness.

Kolleck et al. (2000) measured R-curve behavior of $BaTiO_3$ and PZT under electric field parallel to the crack face in compact tension specimens. The initial value and the steady-state toughness increased as the electric field increased. It was suggested from stress strain data obtained from bend bar experiments that the energy barrier to switch domains increased under an electric field parallel to the poling direction, which increased the toughness.

Anisotropic Fracture in Single Crystal PZN-4.5%PT

New interest in ferroelectric single crystal actuators and sensors has motivated the need to assess the material's fracture behavior. The identification of key fracture mechanisms that differ from ferroelectric ceramics is important to guard against unexpected device failures. The key to strong and tough brittle *ceramics* is the "microstructural shielding" behavior which manifest from residual stress in the crack wake (Budiansky et al. 1983; McMeeking and Evans 1981) as previously shown in Figure 2.1. Grain boundaries play an integral role in the formation of residual stresses. The lack of grain boundaries in ferroelectric single crystals requires identifying critical mechanisms that describe how and when cracks form and propagate in these materials.

Recent work has focused on quantifying single crystal fracture toughness in PZN-4.5%PT, barium titanate ($BaTiO_3$), and PMN-35%PT using Vickers indentions (Fang and Yang 2002; Hosono et al. 1999; Shang and Tan 2001). The crystal cut and local domain switching was found to contribute to toughening in directions perpendicular to domain walls. Local effects at the domain level have been quantified in single crystal PMN-PT using transmission electron microscopy (TEM) (Tan et al. 2000; Xu et al. 2000). It was observed that cracks tend to form and propagate along domain walls in TEM specimens. More recently, Liu et al. (2004) have evaluated the effects of electric field concentrations at partial electrodes in PZN-4.5%PT. Specimen thickness, electrode coverage and field level contributed to the fracture behavior.

Indentation methodology has provided a versatile and simple technique for characterizing fracture toughness. It provides useful information in materials that exhibit a single valued toughness, although the complex crack formation requires some sort of calibration to obtain a material-dependent proportionality constant (Anstis et al. 1981). This technique also assumes the crack patterns remain well behaved and the material underneath the indenter deforms at constant volume. Complications in determining the calibration constants can arise when electro-mechanical coupling is present. In addition, when R-curve behavior is present the toughness requires additional numerical and experimental analysis (Braun et al. 1992; Lawn 1975).

More recently, techniques have been adopted that use bend bar specimens with machined notches or pre-cracks to characterize fracture toughness in ceramics. Nominal bend bar geometry is typically 3 X 4 X 25 mm^3 although the lengths may vary for a

specific loading device or material availability. The Single-Edge-Notched Beam (SENB) method is a simple method that contains a machined notch on the 3 X 25 mm^2 side of a bend bar. The results of this test may be influenced by the notch radius, particularly when the crack tip is close to the notch. The Surface Crack in Flexure (SCF) method has also been used in ferroelectric ceramics (Chen et al. 2001; Karastamatis et al. 2002). In this technique, a Knoop indentation is placed on the 4 X 25 mm^2 side of the bend bar and the specimen is loading in four point bending. Although this method more closely represents actual flaws potentially present in ceramic materials, the indentation residual stresses must be polished away for obtaining accurate initial toughness measurements. Calibration is also required to account for the nonlinear stress field through the bend bar thickness and the semi-elliptical indentation geometry.

Fracture toughness versus crack length has also been characterized using the Single-Edge-V-Notched Beam (SEVNB) method (Kübler 1997; Moon et al. 2000; Stech and Rödel 1996). This method is similar to the SENB except a V-notch is machined into the material with a razor blade. This technique minimizes specimen preparation and eliminates calibration procedures relative to indentation techniques and the SCF method. This technique is adopted in Chapter VI to quantify R-curve behavior in PZN-4.5%PT.

Closure

The following two chapters discuss theoretical techniques in solving the anisotropic electro-elastic K-fields in piezoelectric materials. An orthotropic rescaling

technique is developed which directly identifies how material properties affect the field solution near the crack tip. The technique is compared to Stroh's formalism for poled piezoelectric materials under electro-mechanical loading. Stroh's formalism is then adopted to assess the effects of inhomogeneities on microfracture in piezoelectric solids. Crack face boundary conditions and energy release rate are evaluated to determine driving forces for microfracture.

In Chapters V and VI, the toughness of ferroelectric ceramic PZT and single crystal PZN-4.5%PT are characterized. The influence of relative humidity and electrical boundary conditions on crack kinetics in PZT is experimentally determined using compact tension specimens. The fracture behavior of single crystal PZN-4.5%PT is characterized using the SEVNB method. The single crystal crack profile is measured very close to the crack tip using scanning electron micrographs. The global and local energy release rates are determined by using the applied K from the SEVNB experiments and the crack tip toughness from the crack opening profile measurements, respectively.

CHAPTER III

ANISOTROPIC ELASTICITY TECHNIQUES FOR PIEZOELECTRIC MATERIALS

Analysis of stress fields in a linear elastic-piezoelectric-dielectric medium requires use of anisotropic elasticity theory. Many researchers employ the Stroh formalism, which requires the solution of a sixth order characteristic equation involving material coefficients. This equation must be solved numerically for each material composition to obtain the eigenvalues and eigenvectors that give the resulting field quantities. The eigenvector problem can be circumvented by employing the Barnett-Lothe tensors (Barnett and Lothe 1973), but these tensors must also be computed numerically (Grunderson and Lothe 1987).

The focus of this chapter is on the development of a closed form solution for the electromechanical crack tip fields in piezoelectric materials using orthotropic rescaling. The orthotropic rescaling technique reduces the governing field equations to the biharmonic equation and the Poisson equation. Solutions for an isotropic linear elastic material are utilized to obtain solutions for the anisotropic piezoelectric material. This leads to closed form solutions for the fields in terms of ratios of certain elastic, dielectric, and piezoelectric coefficients. Orthotropic rescaling and the Stroh formalism are

compared and recommendations are made for when and when not to use the orthotropic rescaling approach.

Governing Equations

The governing equations are presented in indicial notation, with summation implied over repeated indices. The small strain assumption is used since the results are to be applied to piezoelectric ceramics and crystals that strain less than 1%. The effect of a polar medium inducing a non-symmetric stress tensor is neglected. Kamlah (2001) showed that the stress induced by the polarity of the medium is on the order of 1 MPa, negligible relative to the far higher stresses found in the elastic problem. Under these assumptions, the following field equations govern linear piezoelectric solids.

Mechanical equilibrium of stress is given by the divergence of the second order stress tensor when body forces are negligible.

$$\sigma_{ji,j} = 0 \tag{3.1}$$

The mechanical equilibrium equation is satisfied when the stress is given by the double curl of a second order potential,

$$\sigma_{ij} = -\Phi_{mn,kl} \in_{ikm} \in_{jnl} \tag{3.2}$$

where Φ_{ij} is the second order stress potential and $\in_{pki}$ is the components of the permutation symbol. For two-dimensional problems, the second order stress potential reduces to the Airy stress potential given by Equation (3.3).

$$\Phi = \Phi_{33}(x_1, x_2) \tag{3.3}$$

In this case the stress field is represented by the following equation,

$$\sigma_{ij} = \Phi_{,kk}\delta_{ij} - \Phi_{,ij} \tag{3.4}$$

where δ_{ij} is the Kronecker delta.

The small strain – displacement relation is given by

$$\varepsilon_{ij} = \frac{1}{2}\left(u_{i,j} + u_{j,i}\right) \tag{3.5}$$

where ε_{ij} is the strain and u_i is the displacement vector.

Compatibility conditions must hold to ensure three displacements can be determined from the six strain components. The compatibility condition is given by Equation (3.6)

$$\in_{pki} \in_{mjl} \varepsilon_{ij,kl} = 0 \tag{3.6}$$

Quasi-static charge balance in the absence of free charge is given by

$$D_{i,i} = 0 \tag{3.7}$$

where D_i is the electric displacement vector.

Equation (3.7) is satisfied when the electric displacement is found from the curl of a vector potential,

$$D_p = \Psi_{i,k} \in_{pki} \tag{3.8}$$

For two-dimensional problems, the electric displacement vector potential reduces to the following scalar potential,

$$\Psi_3 = \Psi_3(x_1, x_2) \tag{3.9}$$

In quasi-static problems the curl of the electric field is zero.

$$E_{i,k} \in_{pki} = 0 \tag{3.10}$$

This condition is satisfied when the electric field vector is represented by the gradient of the electric potential.

$$E_i = -\phi_{,i} \tag{3.11}$$

The coupled form of the electro-mechanical constitutive law can be written in several forms. The Stroh formalism typically uses the form given by Eqs. (3.12a, b).

$$\sigma_{ij} = C^E_{ijkl}\varepsilon_{kl} - e_{kij}E_k \tag{3.12a}$$

$$D_i = e_{ikl}\varepsilon_{kl} + \kappa^{\varepsilon}_{ik}E_k \tag{3.12b}$$

where C_{ijkl}^{E} are the stiffness coefficients at constant electric field, e_{kij} are the piezoelectric coefficients, and $\kappa_{ik}^{\varepsilon}$ are the dielectric coefficients at fixed strain.

The orthotropic rescaling technique may use one of two forms of the constitutive law given below,

$$\varepsilon_{ij} = s_{ijkl}^{E}\sigma_{kl} + d_{kij}E_{k} \tag{3.13a}$$

$$D_{i} = d_{ikl}\sigma_{kl} + \kappa_{ik}^{\sigma}E_{k} \tag{3.13b}$$

$$\varepsilon_{ij} = s_{ijkl}^{D}\sigma_{kl} + g_{kij}D_{k} \tag{3.14a}$$

$$E_{i} = -g_{ikl}\sigma_{kl} + \beta_{ik}^{\sigma}D_{k} \tag{3.14b}$$

where s_{ijkl}^{D} and s_{ijkl}^{E} are the open circuit and short circuit compliance coefficients, respectively, g_{kij} and d_{kij} are the piezoelectric coefficients, and β_{ik}^{σ} and κ_{ik}^{σ} are the dielectric impermittivity and permittivity coefficients at fixed stress, respectively.

Solutions to certain boundary value problems are more easily attained by satisfying traction and surface charge boundary conditions which are more readily applied using Eqs. (3.14a, b) and applying Eqs. (3.6) and (3.10). For example, the impermeable crack problem requires applying zero electric displacement normal to the crack face. This is achieved by using the electric displacement vector potential given by

Equation (3.8). If electric potential boundary conditions are preferred (such as a conducting crack which requires a zero electric potential across the crack face), the constitutive law given by Eqs. (3.13a, b) can be used by applying Eqs. (3.6) and (3.7).

Relations between the internal fields and the surface quantities are given by Eqs. (3.15) and (3.16)

$$t_i = \sigma_{ji} n_j \tag{3.15}$$

$$\omega = -D_i n_i \tag{3.16}$$

where t_i is the traction vector on the surface, n_j is a unit vector normal to the surface, and ω is the surface charge density. The mechanical displacement and the electric potential are continuous from the specified surface value to the material just beneath the surface. These boundary conditions will be used in solving the crack problem.

Material Property Considerations

The general solutions presented here using the orthotropic rescaling and the Stroh formalism technique focuses on two-dimensional problems. The determination of plane stress and plane strain field quantities requires decoupling the plane and anti-plane problems. For the case of the anisotropic elastic medium, symmetry in the elastic

coefficients and a few minimal restrictions on the coefficients leads to uncoupled anti-plane and in-plane deformation, (Ting 1996). Uncoupled anti-plane deformation requires the out-of-plane shear coupling elastic coefficients to be zero. Using Voigt notation (Malvern 1969), the elastic shear coupling coefficients that must be zero are given by Equation (3.17).

$$C_{14} = C_{15} = C_{24} = C_{25} = C_{46} = C_{56} = 0 \tag{3.17}$$

Poled piezoelectric ceramic materials and some piezoelectric single crystal cuts are transverse isotropic and no shear coupling exists; therefore, in-plane loading does not induce any anti-plane deformation. The non-zero elastic, piezoelectric and dielectric coefficients are given in Voight notation in Appendix A. A comment on notation: although the polarization direction is typically taken to be the x_3 direction in the piezoelectric literature, the two-dimensional problems discussed in the following sections take the polarization direction to be in the x_2 direction for consistency with the fracture mechanics literature. This requires a change of subscripts on all published piezoelectric material coefficients.

Orthotropic Rescaling for Piezoelectric Materials

The absence of shear coupling in transversely isotropic piezoelectric materials allows the orthotropic rescaling technique discussed by Suo et al. (1991) for elastic materials to be extended to piezoelectric materials. This class of piezoelectric materials (poled in the x_2 direction) has transverse isotropic symmetry about the poling axis.

Stress Governing Equations

The equations for the plane piezoelectric problem poled in the x_2 direction are developed assuming plane stress. The plane strain case requires some additional algebra to determine the material coefficients. This is done in Appendix A. The constitutive law governing strain, Equation (3.14a), is substituted into strain compatibility, Equation (3.6), and reduced using the Airy stress function, Equation (3.3), and the electric displacement potential, Equation (3.9).

$$s_{1111}^{D}\Phi_{,2222} + 2(s_{1122}^{D} + 2s_{1212}^{D})\Phi_{,1122} + s_{2222}^{D}\Phi_{,1111} = (2g_{112} + g_{211})\Psi_{3,122} + g_{222}\Psi_{3,111} \tag{3.18}$$

The electric displacement potential terms in Equation (3.18) must be eliminated using rescaling to further reduce Equation (3.18) to the biharmonic equation governing the stress field in rescaled coordinates. The curl-free electric field is applied to Equation

(3.14b) and the result is used to eliminate these terms. It is expanded for the in-plane piezoelectric problem and given by Equation (3.19).

$$-(g_{211}+2g_{112})\Phi_{,122}-g_{222}\Phi_{,111}=\beta_{11}^{\sigma}\Psi_{3,22}+\beta_{22}^{\sigma}\Psi_{3,11} \tag{3.19}$$

A fourth-order partial differential equation is obtained by differentiating Equation (3.19) with respect to x_1. The resulting equation is then multiplied by a decoupling coefficient B.

$$B\left[-(g_{211}+2g_{112})\Phi_{,1122}-g_{222}\Phi_{,1111}=\beta_{11}^{\sigma}\Psi_{3,122}+\beta_{22}^{\sigma}\Psi_{3,111}\right] \tag{3.20}$$

The electric displacement potential is eliminated by adding Equation (3.20) to Equation (3.18) and determining the necessary conditions to impose on the decoupling coefficient B. This gives Equation (3.21).

$$(s_{2222}^{D}-Bg_{222})\Phi_{,1111}+\left[2(s_{1122}^{D}+2s_{1212}^{D})-B(g_{211}+2g_{112})\right]\Phi_{,1122}+s_{1111}^{D}\Phi_{,2222}=$$

$$\left(2g_{112}+g_{211}+B\beta_{11}^{\sigma}\right)\Psi_{3,122}+\left(g_{222}+B\beta_{22}^{\sigma}\right)\Psi_{3,111} \tag{3.21}$$

The decoupling coefficient, B, must simultaneously satisfy two different conditions (typically exclusive), which are given by Equation (3.22).

$$B = -\frac{\left(g_{211} + 2g_{112}\right)}{\beta_{11}^{\sigma}} = -\frac{g_{222}}{\beta_{22}^{\sigma}} \tag{3.22}$$

The constraint given by Equation (3.22) can be cast into the following ratio of piezoelectric and permittivity ratios.

$$\frac{\beta_{11}^{\sigma}}{\beta_{22}^{\sigma}} = \frac{g_{211} + 2g_{112}}{g_{222}} \tag{3.23}$$

When Equation (3.23) is satisfied, a rescaling parameter can be introduced.

$$\tilde{x}_1 = x_1 \tag{3.24}$$

$$\tilde{x}_2 = ax_2 \tag{3.25}$$

where,

$$\frac{\partial}{\partial x_1} = \frac{\partial}{\partial \tilde{x}_1}\frac{\partial \tilde{x}_1}{\partial x_1} = \frac{\partial}{\partial \tilde{x}_1} \tag{3.26}$$

and

$$\frac{\partial}{\partial x_2} = \frac{\partial}{\partial \tilde{x}_2}\frac{\partial \tilde{x}_2}{\partial x_2} = a\frac{\partial}{\partial \tilde{x}_2} \tag{3.27}$$

By using the rescaled coordinate system $(\tilde{x}_1, \tilde{x}_2)$, Equation (3.21) is transformed to Equation (3.28).

$$\Phi_{,1111} + a^2\left[\frac{2(s^D_{1122} + 2s^D_{1212}) - B(g_{211} + 2g_{112})}{s^D_{2222} - Bg_{222}}\right]\Phi_{,11\tilde{2}\tilde{2}} + \frac{a^4 s^D_{1111}}{s^D_{2222} - Bg_{222}}\Phi_{,\tilde{2}\tilde{2}\tilde{2}\tilde{2}} = 0 \tag{3.28}$$

To reduce Equation (3.28) to the biharmonic equation in the rescaled coordinates, the rescaling parameter is defined as,

$$a^2 = \sqrt{\frac{s^D_{2222} - Bg_{222}}{s^D_{1111}}} \tag{3.29}$$

Substituting Equation (3.29) into Equation (3.28) gives

$$\Phi_{,1111} + 2\rho' \Phi_{,11\tilde{2}\tilde{2}} + \Phi_{,\tilde{2}\tilde{2}\tilde{2}\tilde{2}} = 0 \tag{3.30}$$

where,

$$\rho' = \frac{2(s^D_{1122} + 2s^D_{1212}) - B(g_{211} + 2g_{112})}{2\sqrt{s^D_{1111}(s^D_{2222} - Bg_{222})}} \tag{3.31}$$

When $\rho' = 1$ Equation (3.30) reduces to the biharmonic equation in the rescaled coordinates. This result allows previously determined elasticity solutions to be utilized to solve orthotropic piezoelectric problems. The factor, ρ', typically ranges between 0.77 and 1.31 for poled PZT materials. Numerical examples will be given which compare the "idealized" case, to real material coefficients by use of the Stroh formalism.

The rescaled governing equation is thus given by Equation (3.32).

$$\nabla^4 \Phi = 0 \tag{3.32}$$

To solve Equation (3.32), the boundary conditions must be mapped into the $(\tilde{x}_1, \tilde{x}_2)$ coordinates. This will be addressed in the Orthotropic Rescaling Details Section.

Electrical Field and Electric Displacement Governing Equations

The electrical components cannot be decoupled from the stress field. They must be directly determined by solving Equation (3.19). This equation is an inhomogeneous partial differential equation that can be simplified by employing the decoupling coefficient given by Equation (3.23).

Equation (3.19) is normalized with respect to the permittivity in the x_2 direction.

$$\Psi_{3,11} + \frac{\beta_{11}^{\sigma}}{\beta_{22}^{\sigma}}\Psi_{3,22} = -\left(\frac{g_{211} + 2g_{112}}{\beta_{22}^{\sigma}}\right)\Phi_{,221} - \frac{g_{222}}{\beta_{22}^{\sigma}}\Phi_{,111} \tag{3.33}$$

The particular solution that satisfies Equation (3.33) is given by Equation (3.34). This solution is valid when the decoupling ratio holds. The particular solution was simplified using a different form of the piezoelectric coefficients (IEEE 1987), $-g_{222}/\beta_{22}^{\sigma} = d_{222}$

$$\Psi_3^p = -d_{222}\Phi_{,1} \tag{3.34}$$

where the superscript *p* defines the particular component of the solution.

The homogeneous solution is found by setting Equation (3.33) equal to zero and rescaling the coordinates using the following equations,

$$\bar{x}_1 = x_1 \tag{3.35}$$

$$\bar{x}_2 = bx_2 \tag{3.36}$$

$$b = \sqrt{\frac{\beta_{22}^{\sigma}}{\beta_{11}^{\sigma}}} \tag{3.37}$$

This gives Laplace's equation in the rescaled coordinate system where the superscript *h* defines the homogeneous component of the solution.

$$\nabla^2 \Psi_{\bar{3}}^h = 0 \tag{3.38}$$

To determine the electric displacement components, the homogeneous solution is rescaled to the original coordinate system and the particular solution is added to the final result.

$$\Psi_3 = \Psi_3^h + \Psi_3^p \tag{3.39}$$

The boundary conditions are then applied in the original coordinate system to determine the electric displacement components. The boundary conditions for the asymptotic crack problem will be given in the Fracture Problem section.

Stroh's Formalism

The Stroh formalism solves the governing equations by assuming a generalized two dimensional displacement field that is a function of (x_1, x_2) only. The displacement field is introduced by utilizing a set of complex planes (z_j) where i=1 to 3 for the two dimensional case.

$$u_i = 2\,\mathrm{Re}\left\{\sum_{j=1}^{3} A_{ij} f(z_j) q_j\right\} \tag{3.40}$$

$$z_j = x_1 + p_j x_2 \tag{3.41}$$

The complex coefficients A_{ij}, q_j, and p_j are constants to be determined.

The electric field is included in Equation (3.40) by defining u_3 as the electric potential.

$$E_i = -u_{3,i} \tag{3.42}$$

The stress and electric displacement components are rewritten in matrix form to make use of the formulation developed by Stroh.

$$\Sigma_{i1} = \sigma_{i1} \quad \text{for } i=1,2 \quad \text{and} \quad \Sigma_{i1} = D_1 \quad \text{for } i=3 \tag{3.43a}$$

$$\Sigma_{i2} = \sigma_{i2} \quad \text{for } i=1,2 \quad \text{and} \quad \Sigma_{i2} = D_2 \quad \text{for } i=3 \tag{3.44b}$$

The stress tensor and electric displacement vector can be represented by a generalized vector potential, φ_i. By comparing Eqs. (3.2) and (3.8), the Airy stress potential and electric displacement potential can be related to the generalized stress vector potential.

$$\Sigma_{i1} = -\varphi_{i,2} = \Phi_{,k2} \in_{ik3} \qquad (i,k=1,2) \tag{3.45a}$$

$$\Sigma_{i2} = \varphi_{i,1} = -\Phi_{,k1} \in_{ik3} \qquad (i,k=1,2) \tag{3.45b}$$

$$\Sigma_{i1} = -\varphi_{i,2} = \Psi_{3,2} \qquad (i=3) \tag{3.46a}$$

$$\Sigma_{i2} = \varphi_{i,1} = -\Psi_{3,1} \qquad (i=3) \tag{3.46b}$$

The generalized vector potential can be related to the complex function given by Equation (3.40) through substitution into the constitutive law, Eqs. (3.12a, b).

$$\varphi_i = 2\,\mathrm{Re}\left\{\sum_{j=1}^{3} B_{ij} f(z_j) q_j\right\} \tag{3.47}$$

The complex constants, B_{ij}, are related to A_{ij} and material coefficients, (Ting 1996).

Upon substituting displacements and the electric potential into the constitutive relation, an eigenvector problem is developed by applying Eqs. (3.1) and (3.7).

$$\left(C^{E}_{ijkl} a_k + e_{lij} a_3\right)\left(\delta_{j1} + p\delta_{j2}\right)\left(\delta_{l1} + p\delta_{l2}\right) = 0 \tag{3.48a}$$

$$\left(e_{ikl} a_k - \kappa^{\varepsilon}_{il} a_3\right)\left(\delta_{i1} + p\delta_{i2}\right)\left(\delta_{l1} + p\delta_{l2}\right) = 0 \tag{3.48b}$$

This provides a means for determining the eigenvectors, A_{ij}, and the eigenvalues, p_i. The eigenvectors, B_{ij}, are found through constitutive relations or reformulating the eigenvector problem to solve A_{ij}, B_{ij}, and p_i simultaneously, (Ting 1996).

The final form of the generalized stress potential given by Equation (3.47) and the generalized displacement field given by Equation (3.40) is written in terms of the Stroh eigenvectors (a_i, b_i), the complex function ($f(z_i)$), and a set of boundary condition constants (q_j). The eigenvectors are given in matrix form where only three of the six eigenvectors are utilized in the solution.

$$\mathbf{A} = \begin{bmatrix} \mathbf{a}_1 & \mathbf{a}_2 & \mathbf{a}_3 \end{bmatrix} \tag{3.49}$$

$$\mathbf{B} = \begin{bmatrix} \mathbf{b}_1 & \mathbf{b}_2 & \mathbf{b}_3 \end{bmatrix} \tag{3.50}$$

The solution utilizes three eigenvectors which are chosen to have positive imaginary components. The other three vectors are linearly dependent in three dimensional space; therefore, are not necessary to uniquely solve the problem (Stroh 1958).

Fracture Problem

Asymptotic crack tip fields are found using orthotropic rescaling and compared to fields using the Stroh formalism. The crack is assumed to be contained within an infinite piezoelectric medium with impermeable crack faces. The origin of the coordinate system is located at the crack tip as shown in Figure 3.1. A closed form solution is obtained for the stress and electric displacement fields using the orthotropic rescaling given by Eqs. (3.51) and (3.52) when $\rho' = 1$ and decoupling holds,

$$\begin{bmatrix} \sigma_{11} \\ \sigma_{12} \\ \sigma_{22} \end{bmatrix} = \frac{K_I}{\sqrt{2\pi\tilde{r}}} \cos\left(\frac{\tilde{\theta}}{2}\right) \begin{bmatrix} a^2\left(1-\sin\left(\frac{\tilde{\theta}}{2}\right)\sin\left(\frac{3\tilde{\theta}}{2}\right)\right) \\ a\sin\left(\frac{\tilde{\theta}}{2}\right)\cos\left(\frac{3\tilde{\theta}}{2}\right) \\ \left(1+\sin\left(\frac{\tilde{\theta}}{2}\right)\sin\left(\frac{3\tilde{\theta}}{2}\right)\right) \end{bmatrix} \tag{3.51}$$

$$\begin{bmatrix} D_1 \\ D_2 \end{bmatrix} = \begin{bmatrix} \frac{-bK_{IV}}{\sqrt{2\pi\bar{r}}}\sin\left(\frac{\bar{\theta}}{2}\right) + d_{222}\frac{K_I}{\sqrt{2\pi}}\left[\frac{b}{\sqrt{\bar{r}}}\sin\left(\frac{\bar{\theta}}{2}\right) + \frac{a}{\sqrt{\tilde{r}}}\cos\left(\frac{\tilde{\theta}}{2}\right)\sin\left(\frac{\tilde{\theta}}{2}\right)\sin\left(\frac{3\tilde{\theta}}{2}\right)\right] \\ \frac{K_{IV}}{\sqrt{2\pi\bar{r}}}\cos\left(\frac{\bar{\theta}}{2}\right) + d_{222}\frac{K_I}{\sqrt{2\pi}}\left[\frac{1}{\sqrt{\tilde{r}}}\cos\left(\frac{\tilde{\theta}}{2}\right)\left\{1+\sin\left(\frac{\tilde{\theta}}{2}\right)\sin\left(\frac{3\tilde{\theta}}{2}\right)\right\} - \frac{1}{\sqrt{\bar{r}}}\cos\left(\frac{\bar{\theta}}{2}\right)\right] \end{bmatrix} \tag{3.52}$$

where a and b are rescaling coefficients from Eqs. (3.29) and (3.37), d_{222} is the piezoelectric coefficient and $(\tilde{r},\tilde{\theta})$ and $(\bar{r},\bar{\theta})$ are the rescaled coordinate systems, and

the strain and electric field are determined from the constitutive law. Details of the solution will be presently shown.

The definitions of stress and electric displacement intensity factors are given by,

$$K_I = \lim_{r\to 0} \sqrt{2\pi r}\,\sigma_{22}\big|_{\theta=0} \tag{3.53}$$

$$K_{IV} = \lim_{r\to 0} \sqrt{2\pi r}\,D_2\big|_{\theta=0} \tag{3.54}$$

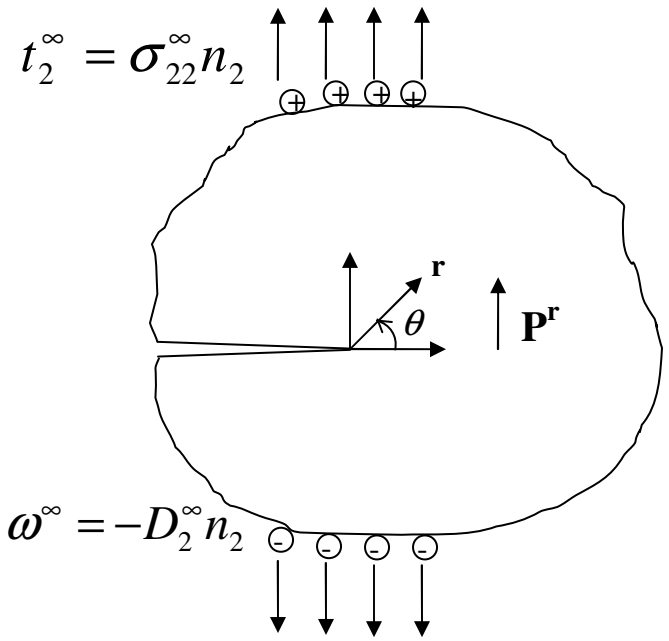

Figure 3.1: Crack geometry used in the contour plots. A crack length of 2c=10 mm and a constant radius of 100 μm around the crack tip are used in all plots.

It will be shown that the Mode I and Mode IV intensity factors are not affected by the coordinate rescaling, therefore standard solutions for Mode I intensity factors can be readily applied to Equation (3.51) since stress is independent of applied electric fields. Special consideration must be taken to determine the Mode IV intensity factor. The center crack panel is a special case of decoupling, $K_{IV} = D_2^{\infty}\sqrt{\pi c}$, where D_2^{∞} is the electric displacement applied at the far-field boundary and $2c$ is the crack length. This is not automatically satisfied in fracture problems with other geometries. Other crack geometries require determining the electric displacement at $\theta = 0^{\circ}$ near the crack tip to determine K_{IV}. This can be achieved analtically for certain geometries, otherwise finite element analysis is typically employed.

Orthotropic Rescaling Details

Stress Fields

The advantage of the orthotropic rescaling technique is that it allows existing isotropic elastic and isotropic dielectric solutions to be applied to orthotropic materials in the rescaled coordinate system. For special classes of piezoelectric material, the relations provided by the decoupling coefficient and $\rho' = 1$ results in the biharmonic equation. This constraint decouples applied electric field from affecting stress concentrations. The electric displacement is determined from the particular and homogeneous solution given

in the Electrical Field and Electric Displacement Governing Equations Section. The electric field is then determined from the constitutive law.

The stress components are presented first in terms of the rescaled coordinates and then scaled back to the original coordinate system. An "idealized" set of material properties is presented to show that stress contours from the orthotropic rescaling and the Stroh formalism are equivalent in this case. It is also shown that the electric field does not induce stress near the crack tip for the "idealized" case.

To apply the isotropic Mode I elasticity solution, the boundary conditions on the crack surface are evaluated in the rescaled coordinates. The following equations relate the rescaled coordinate plane $(\tilde{r}, \tilde{\theta})$ to the original coordinates (x_1, x_2),

$$\tilde{r}^2 = x_1^2 + a^2 x_2^2 \tag{3.55a}$$

$$\tilde{\theta} = \tan^{-1}\left(\frac{a x_2}{x_1}\right) \tag{3.55b}$$

From Equation (3.55b), $\tilde{\theta}$ and θ are equivalent at $\pm\pi$. This provides the necessary condition to satisfy the zero traction boundary condition on the crack surface.

The asymptotic stress fields are given in the rescaled coordinates for Mode I loading by analogy with the isotropic solution.

$$\begin{bmatrix} \sigma_{\tilde{1}\tilde{1}} \\ \sigma_{\tilde{1}\tilde{2}} \\ \sigma_{\tilde{2}\tilde{2}} \end{bmatrix} = \frac{K_I}{\sqrt{2\pi\tilde{r}}} \cos\left(\frac{\tilde{\theta}}{2}\right) \begin{bmatrix} 1-\sin\left(\frac{\tilde{\theta}}{2}\right)\sin\left(\frac{3\tilde{\theta}}{2}\right) \\ \sin\left(\frac{\tilde{\theta}}{2}\right)\cos\left(\frac{3\tilde{\theta}}{2}\right) \\ 1+\sin\left(\frac{\tilde{\theta}}{2}\right)\sin\left(\frac{3\tilde{\theta}}{2}\right) \end{bmatrix} \tag{3.56}$$

When the stress components are mapped back to the original (x_1,x_2) coordinate system, Equation (3.51) is obtained.

The stress components in Eqs. (3.56) and (3.51) are written in terms of the Mode I stress intensity factor, K_I, which is identical to the isotropic definition of stress intensity, Equation (3.53) when the rescaling factor is applied on the x_2 coordinate axis, as given by Equation (3.55a). The stress components are shown to differ from the isotropic solution by the rescaling parameter, *a*. When the rescaling parameter, a=1, the isotropic stress fields are recovered.

Electric Displacement Fields

The electric displacement components near a crack tip are determined for the limiting case of an impermeable crack (McMeeking 1999). This crack face boundary condition is not accepted as physical, but only used to compare the technique to Stroh's formalism. The homogeneous solution is first determined in terms of unknown constants

and then the particular solution is added to the result. The unknown constant is determined by applying the impermeable crack face boundary conditions and Equation (3.54). Since the stress concentration is decoupled from applied electrical loading, it is not necessary to obtain the stress solution simultaneously to determine the boundary condition constants.

Laplace's equation was obtained by rescaling the coordinate system according to Eqs. (3.35)-(3.37). The following equations relate the rescaled coordinate plane $(\bar{r},\bar{\theta})$ to the original coordinates (x_1, x_2),

$$\bar{r}^2 = x_1^2 + b^2 x_2^2 \tag{3.57a}$$

$$\bar{\theta} = \tan^{-1}\left(\frac{bx_2}{x_1}\right) \tag{3.55b}$$

The homogeneous component of the electric displacement potential is found using a complex potential,

$$\Psi_3^h = -C\bar{z}^{\lambda+1} = -(A_\lambda + iB_\lambda)\bar{r}^{\lambda+1}e^{(\lambda+1)\bar{\theta}} \tag{3.58}$$

where $\bar{z} = \bar{x}_1 + i\bar{x}_2 = \bar{r}\left[\cos(\bar{\theta}) + i\sin(\bar{\theta})\right]$.

The homogeneous components of the electric displacement are given in polar coordinates by the following equations,

$$D_{\bar{r}}^{h} = \mathrm{Re}\left\{\frac{1}{\bar{r}}\frac{\partial \Psi_3^{h}}{\partial \bar{\theta}}\right\} = (\lambda+1)\bar{r}^{\lambda}\left\{A_{\lambda}\sin\left[(\lambda+1)\bar{\theta}\right] + B_{\lambda}\cos\left[(\lambda+1)\bar{\theta}\right]\right\} \qquad (3.59)$$

$$D_{\bar{\theta}}^{h} = -\mathrm{Re}\left\{\frac{\partial \Psi_3^{h}}{\partial \bar{r}}\right\} = (\lambda+1)\bar{r}^{\lambda}\left\{A_{\lambda}\cos\left[(\lambda+1)\bar{\theta}\right] - B_{\lambda}\sin\left[(\lambda+1)\bar{\theta}\right]\right\} \qquad (3.60)$$

The particular solution must be added prior to applying the boundary conditions. The total electric displacement is given in the real coordinate system by the following equations by using Eqs. (3.8) and (3.34). For brevity, the field components are given in terms of Cartesian coordinates.

$$D_1 = D_1^{h} + D_1^{p} = D_1^{h} + d_{222}\sigma_{12} \qquad (3.61)$$

$$D_2 = D_2^{h} + D_2^{p} = D_2^{h} + d_{222}\sigma_{22} \qquad (3.62)$$

The impermeable crack is defined by setting $D_{\theta}\big|_{\theta=\pm\pi} = D_2\big|_{\theta=\pm\pi} = 0$. The particular solution is zero on the crack face ($\sigma_{22}\big|_{\theta=\pm\pi} = 0$), therefore only the homogeneous solution is needed to determine the unknown constants, A_{λ} and B_{λ}.

The asymptotic solution is found by ensuring finite electrical energy density and infinite electric displacement at the crack tip. This requires $\lambda = -1/2$ and B_λ=0. The constant, A_λ, is determined by using the boundary condition given by Equation (3.54).

$$D_2\big|_{\theta=0} = \frac{K_{IV}}{\sqrt{2\pi r}} = \frac{A_\lambda}{2\sqrt{r}} + d_{222}\frac{K_I}{\sqrt{2\pi r}} \tag{3.63}$$

$$A_\lambda = \sqrt{\frac{2}{\pi}}\left(K_{IV} - d_{222}K_I\right) \tag{3.64}$$

The electric displacement components can be written in terms of the stress intensity factors and a function of the two sets of rescaled coordinates, $(\tilde{r},\tilde{\theta})$ and $(\bar{r},\bar{\theta})$ as previously given by Equation (3.52).

Both rescaled coordinate systems were used in determining the electric displacement field quantities near the crack tip. The electric displacement in the x_2 direction decouples from the Mode I stress intensity directly in front of the crack tip as defined in Equation (3.63).

Stroh Approach

Asymptotic field solutions around a crack tip are determined using the Stroh formalism. The governing equations developed by Stroh furnish the relations for creating a numerical algorithm to determine the eigenvalues and eigenvectors for a given set of material parameters. Detailed numerical results of the eigenvalue problem are given in Appendix A. The eigenvectors are used together with a complex function and boundary conditions constants to determine the stress fields.

The complex function used in Eqs. (3.40) and (3.47) must be determined to find the field quantities around a crack tip. The function must ensure finite strain energy and infinite stress and electric displacement at the crack tip. The following function satisfies these constraints in the electro-elastic body.

$$f(z_j) = \sqrt{z_j} \tag{3.65}$$

The unknown vector quantity, q_j, given in Eqs. (3.40) and (3.47) is found in order to satisfy the boundary conditions. This vector consists of three components for two-dimensional in-plane piezoelectric problems. Since an asymptotic crack solution is utilized, an assumption about the electric boundary condition is made to simplify the analysis. An electrically impermeable crack is again assumed for comparison to the orthotropic rescaling. The following boundary conditions are utilized on the crack face.

$$\sigma_{ji} n_i = 0 \tag{3.66a}$$

$$D_i n_i = 0 \tag{3.66b}$$

The three boundary condition constants are complex; therefore, six equations are required to find both the real and imaginary components. According to Sih et al. (1965) the stress intensity factor applied to an isotropic material is equivalent to that in an orthotropic material. Suo, et al. (1992) extended this relation to piezoelectric material. Based on their results, Eqs. (3.67a) and (3.67b) are used to uniquely solve the boundary condition constants for Mode I and Mode IV loading. When the material is under symmetrical loading (Mode I and IV), an additional boundary condition for no rotation is applied ahead of the crack tip, (3.67c).

$$\sigma_{22}\big|_{\theta=0} = \frac{K_I}{\sqrt{2\pi r}} \tag{3.67a}$$

$$D_2\big|_{\theta=0} = \frac{K_{IV}}{\sqrt{2\pi r}} \tag{3.67b}$$

$$u_2\big|_{\theta=0} = 0 \tag{3.67c}$$

The field quantities near the crack tip are given below in terms of the eigenvector solution,

$$\begin{bmatrix} u_1 \\ u_2 \\ \phi \end{bmatrix} = 2\,\mathrm{Re}\left\{ \begin{bmatrix} A_{11}q_1\sqrt{z_1} + A_{12}q_2\sqrt{z_2} + A_{13}q_3\sqrt{z_3} \\ A_{21}q_1\sqrt{z_1} + A_{22}q_2\sqrt{z_2} + A_{23}q_3\sqrt{z_3} \\ A_{31}q_1\sqrt{z_1} + A_{32}q_2\sqrt{z_2} + A_{33}q_3\sqrt{z_3} \end{bmatrix} \right\} \tag{3.68}$$

$$\begin{bmatrix} \sigma_{21} \\ \sigma_{22} \\ D_2 \end{bmatrix} = \mathrm{Re}\left\{ \begin{bmatrix} B_{11}q_1/\sqrt{z_1} + B_{12}q_2/\sqrt{z_2} + B_{13}q_3/\sqrt{z_3} \\ B_{21}q_1/\sqrt{z_1} + B_{22}q_2/\sqrt{z_2} + B_{23}q_3/\sqrt{z_3} \\ B_{31}q_1/\sqrt{z_1} + B_{32}q_2/\sqrt{z_2} + B_{33}q_3/\sqrt{z_3} \end{bmatrix} \right\} \tag{3.69}$$

$$\begin{bmatrix} \sigma_{11} \\ \sigma_{21} \\ D_1 \end{bmatrix} = -\mathrm{Re}\left\{ \begin{bmatrix} B_{11}q_1p_1/\sqrt{z_1} + B_{12}q_2p_2/\sqrt{z_2} + B_{13}q_3p_3/\sqrt{z_3} \\ B_{21}q_1p_1/\sqrt{z_1} + B_{22}q_2p_2/\sqrt{z_2} + B_{23}q_3p_3/\sqrt{z_3} \\ B_{31}q_1p_1/\sqrt{z_1} + B_{32}q_2p_2/\sqrt{z_2} + B_{33}q_3p_3/\sqrt{z_3} \end{bmatrix} \right\} \tag{3.70}$$

Eqs. (3.69) and (3.70) are compared to the closed form solutions determined by the orthotropic rescaling technique in the following section. Exact solutions are found

when decoupling holds and $\rho' = 1$. Differences in the field quantities are compared using material coefficients for TRS600[1].

Comparison of Results

The orthotropic rescaling technique is directly compared to the Stroh formalism by evaluating changes in computed field quantities with respect to changes in material properties. The results are compared using an "idealized" set of material properties that satisfy the decoupling ratio and $\rho' = 1$; and a real set of material properties with ratios that do not satisfy the decoupling ratio and $\rho' = 1$. In addition, a parametric study illustrates differences in maximum principal stress when the decoupling ratio is greater or less than the ideal value. Contour plots are shown which plot stress components around the crack tip over a constant radius. Vector plots are used to compare electric displacement and electric fields near the crack tip.

The material properties employed in the analysis are based on TRS600. Material coefficients, s_{66}^{D}, g_{16}, and β_{11}^{σ}, were adjusted to satisfy the necessary ratios that gives the biharmonic equation. The material properties used in the orthotropic rescaling technique are given in Table 3.1. These coefficients were converted to the effective plane strain

[1] TRS Ceramics, Inc. State College, PA.

coefficients for direct comparison to the Stroh formalism, see Appendix A for details. The poling axis for the material is the x_2 direction.

Table 3.1: Piezoelectric material properties (plane strain coefficients) used to plot stress fields using the orthotropic rescaling technique. The material coefficients (s_{66}^{D}, g_{16}, and β_{11}^{σ}) have been adjusted to meet the necessary ratios given by the decoupling coefficient and $\rho' = 1$. The decoupling ratio has been given for the plane strain case.

TRS600	**ACTUAL**	**"IDEALIZED"**
β_{22}^{σ} (V^2/N)	2.72×10^{7}	2.72×10^{7}
β_{11}^{σ} (V^2/N)	2.54×10^{7}	3.74×10^{7}
g_{22} (m^2/C)	0.0167	0.0167
g_{21} (m^2/C)	-0.0128	-0.0128
g_{16} (m^2/C)	0.0216	0.0318
s_{11}^{D} (m^2/N)	9.49×10^{-12}	9.49×10^{-12}
s_{22}^{D} (m^2/N)	8.27×10^{-12}	8.27×10^{-12}
s_{12}^{D} (m^2/N)	-3.94×10^{-12}	-3.94×10^{-12}
s_{66}^{D} (m^2/N)	2.66×10^{-11}	2.34×10^{-11}
$\beta_{11}^{\sigma} / \beta_{22}^{\sigma}$	0.78	1.14
$(g_{211}+g_{16})/g_{222}$	0.53	1.14
ρ'	0.92	1.00

Since the Stroh formalism uses another form of the constitutive law, the material coefficients given in Table 3.1 are computed in terms of the coefficients given by Eqs. (3.12a, b). The equivalent material properties are found in Table 3.2.

Table 3.2: Material properties related to the coefficients in Table 3.1 which are used to calculate stress fields using the Stroh formalism. The material coefficients (c_{66}^{E}, e_{16} and $\kappa_{11}^{\varepsilon}$) correspond to the boldface coefficients that were adjusted in Table 3.1.

TRS600	**ACTUAL**	**"IDEALIZED"**
$\kappa_{22}^{\varepsilon}$ (N/V^2)	1.44×10^{-8}	1.44×10^{-8}
$\kappa_{11}^{\varepsilon}$ (N/V^2)	2.33×10^{-8}	$\mathbf{1.24\times10^{-8}}$
e_{22} (C/m^2)	30.38	30.38
e_{21} (C/m^2)	-3.73	-3.73
e_{16} (C/m^2)	18.89	**16.85**
c_{11}^{E} (N/m^2)	8.16×10^{10}	8.16×10^{10}
c_{22}^{E} (N/m^2)	5.97×10^{10}	5.97×10^{10}
c_{12}^{E} (N/m^2)	3.20×10^{10}	3.20×10^{10}
c_{66}^{E} (N/m^2)	2.22×10^{10}	$\mathbf{1.98\times10^{10}}$

Contour plots representing the stress components around the crack tip are first given for the “idealized” case and then compared to the “real” case. The angular dependence on stress is plotted over a region of constant radius and crack orientation as shown in Figure 3.1. Traction and surface charge are applied at the far-field boundary in

the x_2 direction. Mode I and Mode IV intensity factors are applied by letting $K_I = 1$ $MPa\sqrt{m}$ and $K_{IV} = 0.001$ $C/m^2\sqrt{m}$.

Figure 3.2 depicts the crack tip stress field for the maximum principal stress in the "idealized" piezoelectric material. The plot includes the isotropic solution for comparison to the orthotropic material behavior. The stress contour under applied surface charge was not included since it had no effect on the stress fields for the "idealized" case. The orthotropic rescaling technique and Stroh's formalism give identical stress fields.

Figure 3.3 represents how the orthotropic rescaling was less accurate when the actual material properties for TRS600 were used with Equation (3.51). The isotropic solution is not included in the figure. Since the electric field is no longer decoupled from the stress field, the effect of surface charge is included in Figure 3.3 by use of the Stroh formalism. The largest deviation from the exact solution was directly ahead of the crack tip. The lower accuracy of stress ahead of the crack tip was determined to emanate from the stress components σ_{11}.

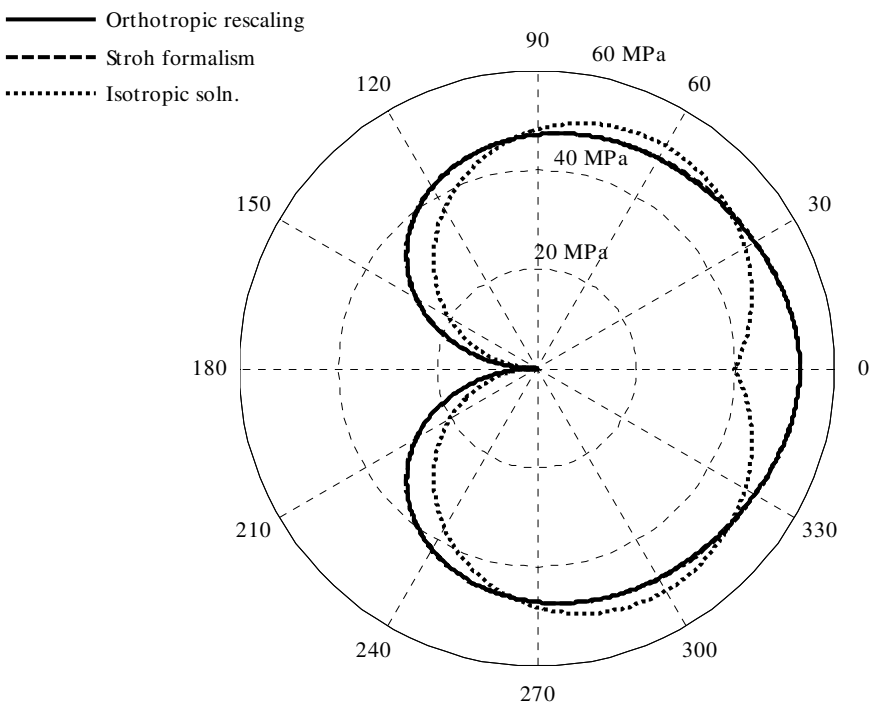

Figure 3.2: Stress contour around the crack tip when rescaling conditions are met for the maximum principal stress, σ_1, from $\theta = \pi$ to $\theta = -\pi$ when r=100 μm.

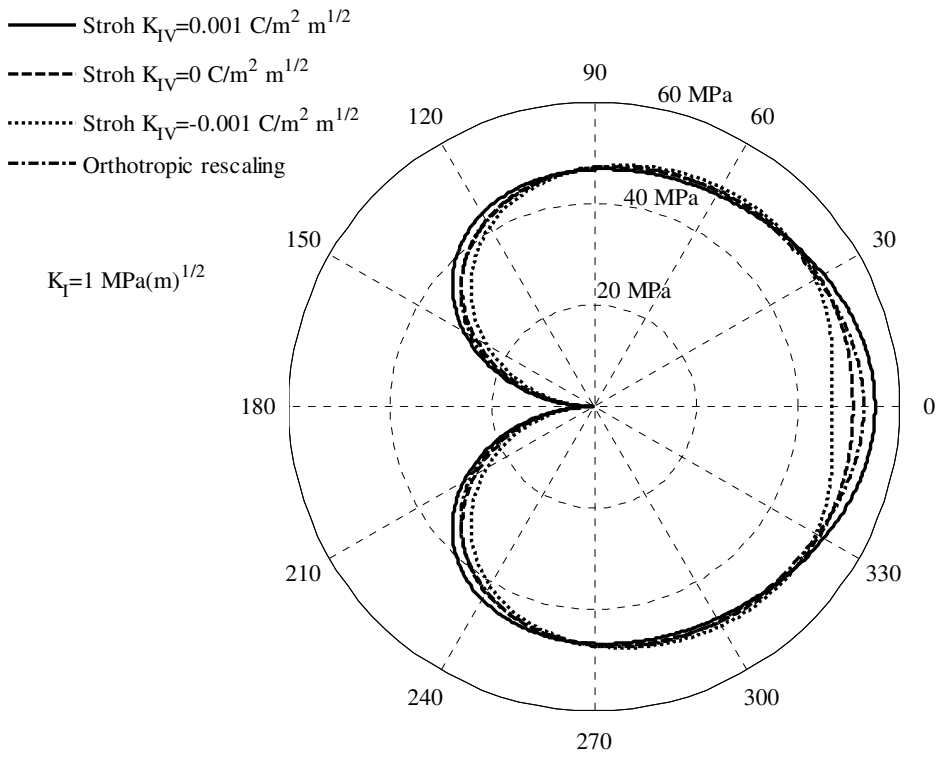

Figure 3.3: Resulting stress contour for the maximum principal stress, σ_1, when the actual material parameters are used; $\theta = \pi$ to $\theta = -\pi$ when r=100 μm.

The effects of the decoupling coefficient are illustrated in Figure 3.4 The maximum principal stress is shown to change when the permittivity ratio deviates from the "idealized" value if the material is under both Mode I and Mode IV loading. In the example, K_I= 1 $MPa\sqrt{m}$ and K_{IV}= 0.002 $C/m^2\sqrt{m}$ was used. If the permittivity ratio is greater than the "idealized" case, the maximum principal stress increases directly ahead of the crack tip. Conversely, if the ratio decreases, the maximum principal stress decreases ahead of the crack tip.

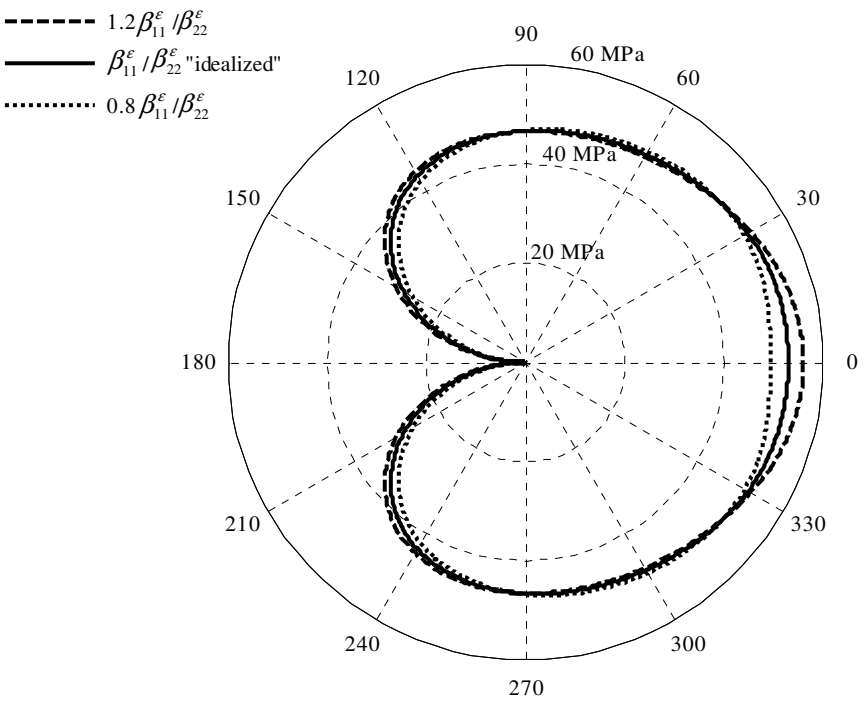

Figure 3.4: Parametric study describing the effects of the decoupling ratio on the maximum principal stress, σ_1, near the crack tip when $K_{IV}= 0.002\ C/m^2\sqrt{m}$. The decoupling ratio, $\beta_{11}^{\sigma}/\beta_{22}^{\sigma}$, was modified while holding the piezoelectric coefficients constant.

The changes in stress directly ahead of the crack tip can be described by the amount of electric displacement permitted by the dielectric constant (β_{11}^{σ}). As the permittivity constant in the x_1 direction increases, the electric field drives more strain in this direction causing an incompatibility. The strain incompatibility is compensated by larger stresses in the x_1 direction (σ_{11}) which alters the maximum principal stress at this point. A converse argument can be made when the permittivity coefficient decreases below the "idealized" case.

The electric displacement is evaluated under a combined Mode I and Mode IV loading (K_I= 1 $MPa\sqrt{m}$ and K_{IV}= 0.001 $C/m^2\sqrt{m}$). A vector plot is used to represent the direction of electric displacement in a confined region near the crack tip. The remnant polarization is not included in the plots. The crack tip is drawn on the plot as a reference point. Exact correlation was found for the electric displacement and electric field when using "idealized" material properties. Figure 3.5 qualitatively represents how the piezoelectric material responds to electro-mechanical loading for TRS600. Negligible differences in electric displacement were observed. Similar results were found for the electric field components.

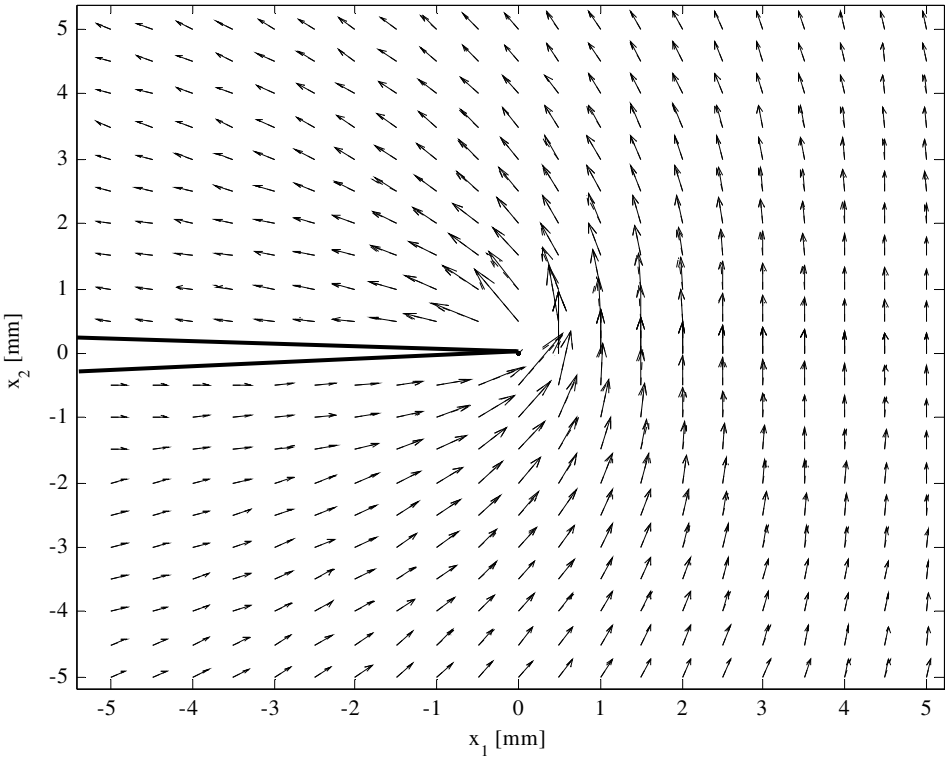

Figure 3.5: Vector plot of electric displacement for TRS600 material properties under Mode I and Mode IV loading ($K_I = 1\ MPa\sqrt{m}$, $K_{IV} = 0.001\ C/m^2\sqrt{m}$). The solutions are practically identical. The Stroh formalism is shown by dotted arrows; the orthotropic rescaling result is shown by solid arrows.

Conclusions

A generalized form of the Airy stress potential was used to formulate closed form solutions for linear piezoelectric boundary value problems. A new technique using

orthotropic rescaling was presented which identified certain ratios of elastic, piezoelectric, and dielectric material coefficients necessary to reduce the formulation to the biharmonic equation. Previously solved isotropic elasticity solutions were utilized to determine stress fields near the crack tip.

The orthotropic rescaling technique was verified using Stroh's formalism for an "idealized" set of material coefficients. The orthotropic rescaling technique gives exact correlation to Stroh's method for the "idealized" set of material coefficients. The technique was less accurate when an actual set of material properties was employed, although reasonable estimations were achieved under mechanical loading. The stress fields from the rescaling technique should be avoided when large electrical loading is present. Considerable deviations in stress were observed directly ahead of the crack tip when a surface charge was present.

The electric displacement and electric field determined from orthotropic rescaling matched well with the Stroh formalism under electro-mechanical loading for the "idealized" case and for TRS600 material properties. The orthotropic rescaling appears to be a robust technique for determining electric field and electric displacement components near a crack tip.

The decoupling coefficient was shown to influence the stress components near a crack tip, although only for a certain ratio of piezoelectric and dielectric coefficients, the stress components are independent of an applied electric field.

CHAPTER IV

MICROFRACTURE OF PIEZOELECTRIC MATERIALS UNDER ELECTRIC FIELD

Spatial variations in piezoelectric material properties can influence localized residual stresses under electro-mechanical loading. Residual stresses generated by electric field loading is believed to contribute to microfracture (Jiang et al. 1994; Lynch 1998; Wang et al. 1998). The onset for crack propagation requires consideration of both mechanical and electrical driving forces. When an electric field is applied perpendicular to a crack, positive and negative charges migrate to opposite crack faces. This tends to retard crack propagation, contradicting a significant portion of data currently available in the literature. This discrepancy motivates a need to evaluate other contributions that may affect microfracture in ferroelectric materials.

The heterogeneity influence on fracture mechanics is evaluated by modeling a piezoelectric elliptic inclusion embedded in a piezoelectric matrix with a crack emanating from the edge of the inclusion. Piezoelectric weight functions are used to assess changes in intensity factors and energy release rate when dissimilar material properties exist between the matrix and inclusion. Application of impermeable and permeable crack face boundary conditions illustrates significant differences in flaw-localized driving forces under electric fields.

Piezoelectric Microfracture

In the present chapter, residual stress generated from heterogeneities under electrical loading is determined to predict driving forces on microcrack growth. Residual stress at the grain level will be approximated by interactions between a piezoelectric elliptic inclusion embedded in a piezoelectric matrix with dissimilar properties. A crack is introduced at the edge of the inclusion as shown in Figure 4.1. A similar technique can be found in the literature for thermal mismatch problems with isotropic materials properties, (Green 1983; Lange 1978). To quantify microcrack driving forces in the electro-mechanically coupled material, piezoelectric weight functions are applied to ascertain the affects of the inclusion for different crack lengths and electrical loading. The driving force for crack propagation is determined by comparing the impermeable vs. permeable crack faces boundary conditions.

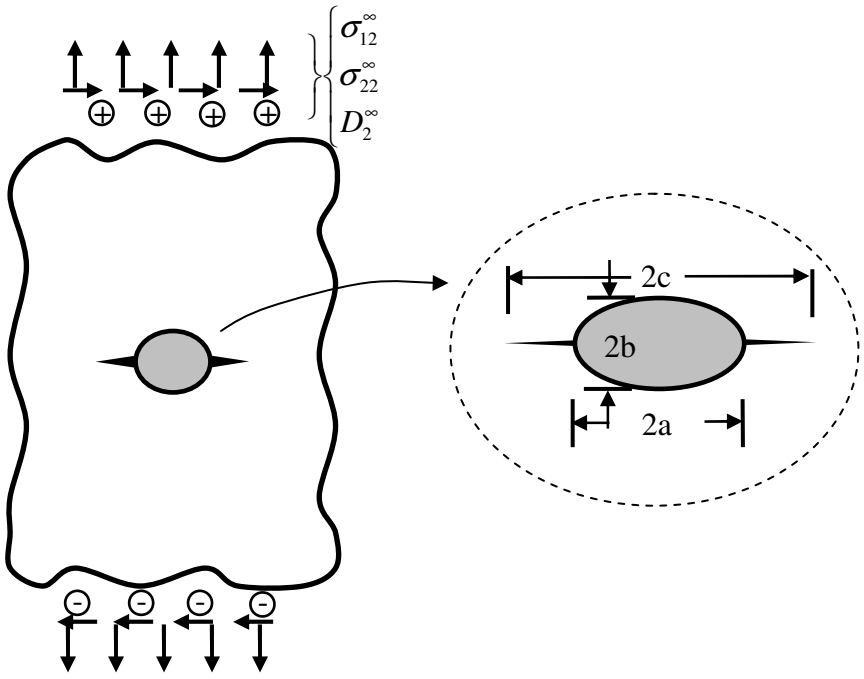

Figure 4.1: Piezoelectric microfracture problem model using an inhomogeneous elliptic inclusion. A crack of outer radius c (c>a) extends from the inclusion edge.

Linear superposition of the fields along the crack is used in the analysis. Once the elliptic inclusion problem is solved, field components acting along the crack plane are used to quantify intensity factors and energy release rate using the weight function method. This is illustrated in Figure 4.2. The method assumes the field concentrations will be greatest at the crack tip.

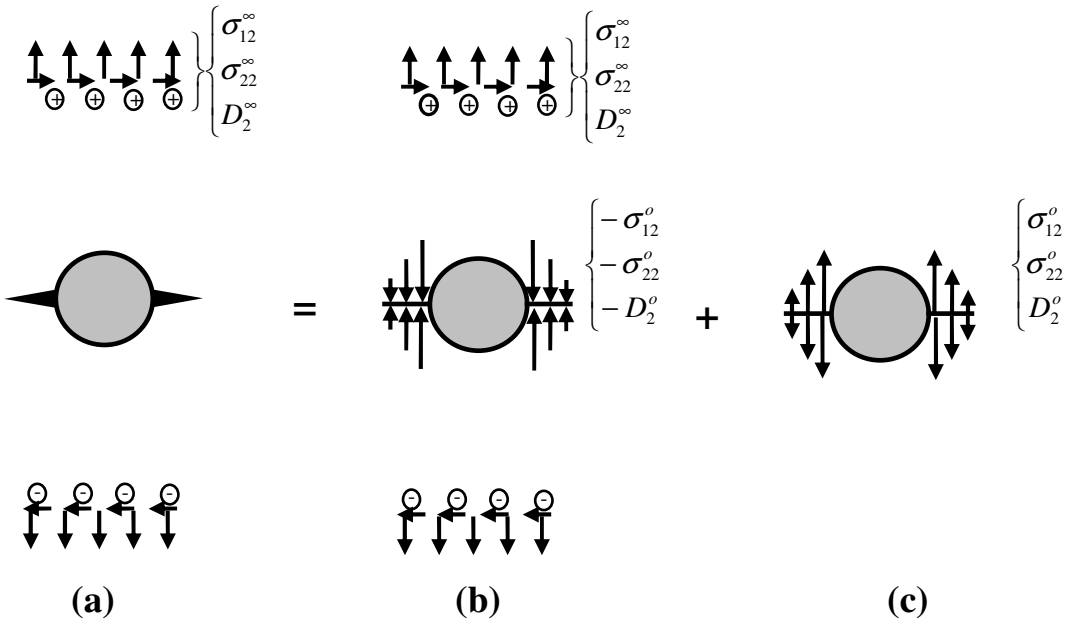

Figure 4.2: Linear superposition of the field components applied along the crack face. The superscript *o* on the stress and electric displacement refers to the field solution from the inclusion problem. Charges must also be applied to the crack face although not shown.

First the governing equations that lead to the solution of the piezoelectric inclusion problem are summarized based on previous work (Liang et al. 1995; Zhang et al. 2001). The piezoelectric weight function method (McMeeking and Ricoeur 2003) is then applied to quantify residual stress influences on the stress and electric displacement intensity factors. The crack face boundary conditions and energy release rate are discussed. Numerical results for a certain variation in composition of PZT are given and compared to experimental results.

Elliptic Piezoelectric Inclusion Subjected to Remote Loading

Governing Equations and Useful Identities

Stroh's formalism presented in Chapter III is used to solve the elliptic inclusion problem. The governing equations and several identities are first presented. A detailed derivation can be found in the literature for anisotropic elastic materials (Ting 1996) and piezoelectric materials (Liang et al. 1995). Figure 4.3 represents the inclusion problem and local coordinate system.

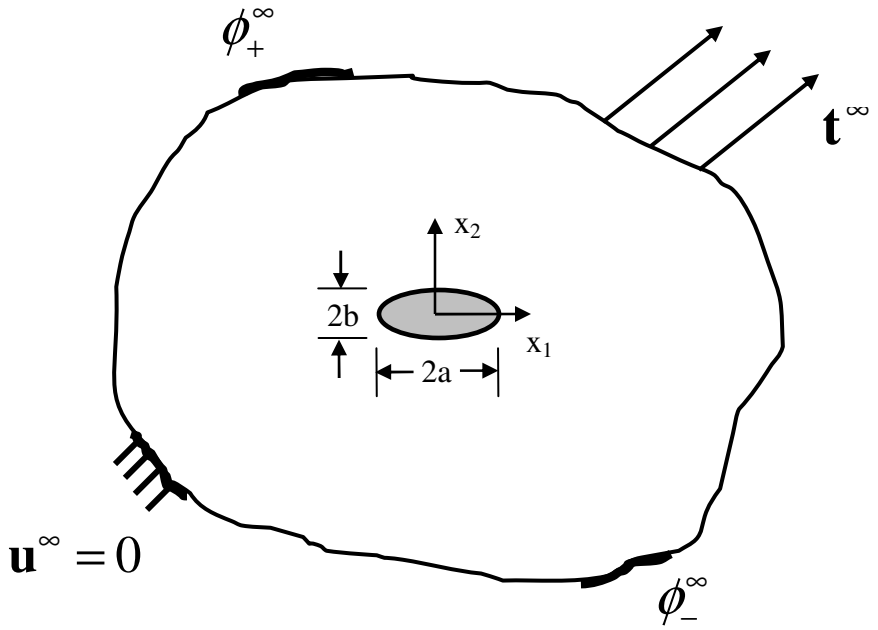

Figure 4.3: Piezoelectric elliptical inclusion problem. The inclusion and matrix contain differing piezoelectric material properties. Arbitrary electro-mechanical loading is represented by specifying some far-field difference in electric potential $(\phi_+^\infty - \phi_-^\infty)$ across the specimen and traction $\mathbf{t}^\infty$ boundary conditions.

As previously developed in Chapter III, Stroh's formalism assumes a displacement and electrical potential and solves mechanical equilibrium and charge compatibility through the use of a piezoelectric constitutive law. The fundamental equations are presented again for convenience.

$$\sigma_{ji,j} = 0 \tag{4.1}$$

$$D_{i,i} = 0 \tag{4.2}$$

$$\sigma_{ij} = C^{E}_{ijkl}\varepsilon_{kl} - e_{kij}E_k \tag{4.3}$$

$$D_i = e_{ikl}\varepsilon_{kl} + \kappa^{\varepsilon}_{ik}E_k \tag{4.4}$$

It was previously shown in Chapter II that the Stroh eigenvectors can be determined from Equations (3.48a,b). This approach required solving a six or eight order polynomial (depending on if anti-plane deformation is included) to determine the eigenvalues (p_i) and associated eigenvectors, **a**. The **b** eigenvectors can then be determined through a constitutive relation. The eigenvectors **a** and **b** can also be determined simultaneously.

Simultaneously solving the eigenvectors has an advantage in representing the solution in a compact form. The basic equations will be summarized here. The technique is illustrated by first expanding out Equations (3.48a,b) by eliminating the Kronecker deltas.

$$(C^{E}_{i1k1}a_k + e_{1i1}a_3) + p(C^{E}_{i1k2}a_k + e_{1i2}a_3 + C^{E}_{i2k1}a_k + e_{1i2}a_3) + p^2(C^{E}_{i2k2}a_k + e_{2i2}a_3) = 0 \tag{4.5}$$

$$(e_{1k1}a_k - \kappa^{\varepsilon}_{11}a_3) + p(e_{ki2}a_k - \kappa^{\varepsilon}_{12}a_3 + e_{2k1}a_k - \kappa^{\varepsilon}_{21}a_3) + p^2(e_{2k2}a_k - \kappa^{\varepsilon}_{22}a_3) = 0 \tag{4.6}$$

Equations (4.5) and (4.6) can be simplified by introducing the following matrix notation.

$$Q_{ik} = \begin{bmatrix} C^E_{i1k1} & e_{1i1} \\ e_{1k1} & -\kappa^{\varepsilon}_{11} \end{bmatrix} \qquad R_{ik} = \begin{bmatrix} C^E_{i1k2} & e_{1i2} \\ e_{2k1} & -\kappa^{\varepsilon}_{12} \end{bmatrix} \tag{4.7a,b}$$

$$R_{ki} = \begin{bmatrix} C^E_{i2k1} & e_{2i1} \\ e_{1k2} & -\kappa^{\varepsilon}_{21} \end{bmatrix} \qquad T_{ik} = \begin{bmatrix} C^E_{i2k2} & e_{2i2} \\ e_{2k2} & -\kappa^{\varepsilon}_{22} \end{bmatrix} \tag{4.8a,b}$$

By substituting the matrices in Equations (4.7) and (4.8) and comparing the result to the stress and electric displacement in terms of eigenvectors in Equation (3.47), a relation between the **a** and **b** eigenvectors can be established.

$$\begin{bmatrix} -\mathbf{Q} & \mathbf{0} \\ -\mathbf{R}^T & \mathbf{I} \end{bmatrix} \begin{bmatrix} \mathbf{a} \\ \mathbf{b} \end{bmatrix} = p \begin{bmatrix} \mathbf{R} & \mathbf{I} \\ \mathbf{T} & \mathbf{0} \end{bmatrix} \begin{bmatrix} \mathbf{a} \\ \mathbf{b} \end{bmatrix} \tag{4.9}$$

Through further manipulation, the eigenvectors **a** and **b** can be determined simultaneously by making use of the following relation,

$$\begin{bmatrix} \mathbf{0} & \mathbf{T}^{-1} \\ \mathbf{I} & -\mathbf{R}\mathbf{T}^{-1} \end{bmatrix} \begin{bmatrix} \mathbf{R} & \mathbf{I} \\ \mathbf{T} & \mathbf{0} \end{bmatrix} = \begin{bmatrix} \mathbf{I} & \mathbf{0} \\ \mathbf{0} & \mathbf{I} \end{bmatrix} \tag{4.10}$$

which leads to,

$$\mathbf{N}\xi = p\xi \tag{4.11}$$

$$\mathbf{N} = \begin{bmatrix} \mathbf{N}_1 & \mathbf{N}_2 \\ \mathbf{N}_3 & \mathbf{N}_1^T \end{bmatrix}, \qquad \xi = \begin{bmatrix} \mathbf{a} \\ \mathbf{b} \end{bmatrix} \tag{4.12a,b}$$

$$\mathbf{N}_1 = -\mathbf{T}^{-1}\mathbf{R}^T, \qquad \mathbf{N}_2 = \mathbf{T}^{-1}, \qquad \mathbf{N}_3 = \mathbf{R}\mathbf{T}^{-1}\mathbf{R}^T - \mathbf{Q} \tag{4.13a,b,c}$$

Equation (4.11) is in the standard eigenvector form which allows **a** and **b** to be solved simultaneously. Since **N** is not symmetric, the eigenvector ξ is a right eigenvector. The left eigenvector (η) can be determined by taking the transpose of **N**. It is known that the left and right eigenvectors associated with different eigenvalues are orthogonal (Weisstein 1999). Since eigenvectors are unique up to a constant multiplier, the left and right eigenvectors can be orthonormalized. Either the left or right

eigenvectors are multiplied by a constant since $\boldsymbol{\eta}$ and $\boldsymbol{\xi}$ are dependent through Equation (4.9).

Based on certain symmetry properties of **N**, it can be shown that,

$$\mathbf{b}_i^T \mathbf{a}_j + \mathbf{a}_j^T \mathbf{b}_i = \delta_{ij} \tag{4.14}$$

where *i* and *j* refer to different eigenvalues. This relation leads to the orthogonal and closure relations of the Stroh formalism. Certain real tensors can be extracted from Equation (4.14) which are often used in anisotropic boundary value problems. These tensors are called the Barnett-Lothe tensors (Barnett and Lothe 1973).

$$\mathbf{S} = i(\mathbf{A}\mathbf{B}^T - \mathbf{I}), \qquad \mathbf{H} = 2i\mathbf{A}\mathbf{A}^T, \qquad \mathbf{L} = -2i\mathbf{B}\mathbf{B}^T \tag{4.15a,b,c}$$

The Barnett-Lothe tensors are only valid when the eigenvectors have been orthonormalized according to Equation (4.14).

The Barnett-Lothe tensors will be used in determining the electro-elastic fields around a piezoelectric inclusion. The following sum rules will also be useful in solving the inclusion problem (Ting 1996),

$$2\mathbf{A}\langle z_* \rangle \mathbf{B}^T = x_1(\mathbf{I} - i\mathbf{S}) + x_2\{\mathbf{N}_1 - i(\mathbf{N}_1\mathbf{S} - \mathbf{N}_2\mathbf{L})\} \tag{4.16}$$

$$2\mathbf{A}\langle z_* \rangle \mathbf{A}^T = -ix_1\mathbf{H} + x_2\{\mathbf{N}_2 - i(\mathbf{N}_1\mathbf{H} - \mathbf{N}_2\mathbf{S}^T)\} \tag{4.17}$$

$$2\mathbf{B}\langle z_* \rangle \mathbf{B}^T = x_1\mathbf{L} + x_2\{\mathbf{N}_3 - i(\mathbf{N}_3\mathbf{S} - \mathbf{N}_1^T\mathbf{L})\} \tag{4.18}$$

$$2\mathbf{B}\langle z_* \rangle \mathbf{A}^T = x_1(\mathbf{I} - i\mathbf{S}^T) + x_2\{\mathbf{N}_1^{\mathbf{T}} - i(\mathbf{N}_3\mathbf{H} - \mathbf{N}_1^{\mathbf{T}}\mathbf{S}^T)\} \tag{4.19}$$

where the brackets $\langle \bullet \rangle$ refer to the diagonal matrix, $\langle z_* \rangle = diag[z_1 \quad z_2 \quad z_3]$.

Piezoelectric Inclusion

The generalized potentials that define the field components within the body consist of a linear superposition of the uniform fields applied far away from the inclusion and the disturbance near the inclusion. The uniform fields are given in vector form,

$$\Omega_1^\infty = \begin{bmatrix} \varepsilon_{11}^\infty \\ \varepsilon_{12}^\infty \\ -E_1^\infty \end{bmatrix}, \qquad \Omega_2^\infty = \begin{bmatrix} \varepsilon_{12}^\infty \\ \varepsilon_{22}^\infty \\ -E_2^\infty \end{bmatrix} \tag{4.20a,b}$$

$$\Sigma_1^\infty = \begin{bmatrix} \sigma_{11}^\infty \\ \sigma_{21}^\infty \\ D_1^\infty \end{bmatrix}, \qquad \Sigma_2^\infty = \begin{bmatrix} \sigma_{12}^\infty \\ \sigma_{22}^\infty \\ D_2^\infty \end{bmatrix} \tag{4.21a,b}$$

where the superscript ∞ refers to loading far away from the inclusion. Rigid body rotations are not included.

The generalized displacement and stress vector potential used in determining the field components in the matrix is cast in the following form,

$$\mathbf{u} = x_1\boldsymbol{\Omega}_1^{\infty} + x_2\boldsymbol{\Omega}_2^{\infty} + 2\,\mathrm{Re}\left\{\mathbf{A}\left\langle\zeta_*^{-1}\right\rangle\mathbf{q}\right\} \tag{4.22}$$

$$\boldsymbol{\varphi} = x_1\boldsymbol{\Sigma}_2^{\infty} - x_2\boldsymbol{\Sigma}_1^{\infty} + 2\,\mathrm{Re}\left\{\mathbf{B}\left\langle\zeta_*^{-1}\right\rangle\mathbf{q}\right\} \tag{4.23}$$

Where the generalized displacement vector **u** includes the in-plane displacement u_1, u_2 and electric potential, $u_3=\phi$. The generalized stress potential $\boldsymbol{\varphi}$ is related to the stress and electric displacement components previously given by Equations (3.45) and (3.46). This can easily be extended to anti-plane two-dimensional deformation, but is not included in the present analysis. The disturbance from the inclusion is determined from the complex set of Stroh eigenvectors ***A*** and ***B***, the complex function $\left\langle\zeta_*^{-1}\right\rangle$, and boundary condition constants ***q***. The brackets $\langle\bullet\rangle$ refer again to the diagonal matrix, $\left\langle\zeta_*^{-1}\right\rangle = diag\left[\zeta_1^{-1} \quad \zeta_2^{-1} \quad \zeta_3^{-1}\right]$.

A non-conformal mapping between the ellipse and a circle is used in determining the complex function ζ_*^{-1}. Using the complex variable $z_* = x_1 + p_* x_2$, the function is given in the following form,

$$\zeta_*^{-1} = \frac{z_* \pm \sqrt{z_*^2 - (a^2 + p_*^2 b^2)}}{a + ip_* b} \tag{4.24}$$

where a and b correspond to the major and minor axes of the elliptical inclusion (not to be confused with the Stroh eigenvectors **a** and **b**) and p_* are the eigenvalues. Two solutions exists in Equation (4.24), which requires a branch cut connecting two infinite sheets in the (x_1,x_2)-plane to the transformed ζ-plane. Since the mapping between the planes is not conformal, the angle between line elements in the (x_1,x_2)-plane and the ζ-plane is in general different. This requires appropriate selection of the positive or negative radical component for certain regions around the inclusion. Details describing the underlying mathematical identities associated with the complex function ζ_*^{-1} are given by Ting (1996).

The field components within the inclusion are uniform, therefore the generalized vector potentials within the inclusion are written in the following form,

$$\mathbf{u}^o = x_1 \mathbf{\Omega}_1^o + x_2 \mathbf{\Omega}_2^o \tag{4.25}$$

$$\boldsymbol{\varphi}^o = x_1 \mathbf{\Sigma}_1^o + x_2 \mathbf{\Sigma}_2^o \tag{4.26}$$

Where the constant field terms inside the inclusion are defined by,

$$\mathbf{\Omega}_1^o = \begin{bmatrix} \varepsilon_{11}^o \\ \varepsilon_{12}^o + \omega_{12}^o \\ -E_1^o \end{bmatrix}, \qquad \mathbf{\Omega}_2^\infty = \begin{bmatrix} \varepsilon_{12}^o + \omega_{21}^o \\ \varepsilon_{22}^o \\ -E_2^o \end{bmatrix} \tag{4.27a,b}$$

$$\mathbf{\Sigma}_1^\infty = \begin{bmatrix} \sigma_{11}^o \\ \sigma_{21}^o \\ D_1^o \end{bmatrix}, \qquad \mathbf{\Sigma}_2^\infty = \begin{bmatrix} \sigma_{12}^o \\ \sigma_{22}^o \\ D_2^o \end{bmatrix} \tag{4.28a,b}$$

It is assumed a rigid body rotation can occur in the inclusion, where $\omega_{ij} = \frac{1}{2}\left(u_{i,j} - u_{j,i}\right)$ for i and j=1,2.

It can be shown that the boundary condition constant **q** for the matrix can be written in the form,

$$\mathbf{q} = \mathbf{A}^T\mathbf{g} + \mathbf{B}^T\mathbf{h} \tag{4.29}$$

where **g** and **h** are real vectors.

Through the use of the sum rules given by Equations (4.16)-(4.19), a relation between material properties and the field quantities is attained.

$$\begin{bmatrix} \boldsymbol{\Omega}_2^{\infty} \\ -\boldsymbol{\Sigma}_1^{\infty} \end{bmatrix} = \mathbf{N} \begin{bmatrix} \boldsymbol{\Omega}_1^{\infty} \\ \boldsymbol{\Sigma}_2^{\infty} \end{bmatrix} \qquad \begin{bmatrix} \boldsymbol{\Omega}_2^{o} \\ -\boldsymbol{\Sigma}_1^{o} \end{bmatrix} = \mathbf{N} \begin{bmatrix} \boldsymbol{\Omega}_1^{o} \\ \boldsymbol{\Sigma}_2^{o} \end{bmatrix} \tag{4.30}$$

where **N** was given by Equation (4.12).

The boundary condition constants must be determined to match displacement and traction across the interface of the inclusion. The elliptic boundary Γ can be defined by some real parameter ψ such that the equation for an ellipse can be related to the Cartesian coordinates,

$$x_1 = a\cos\psi, \qquad x_2 = b\sin\psi \tag{4.31}$$

By making use of the mapping onto a circle in the ζ-plane, it can be shown that,

$$\zeta_*^{-1} = e^{-i\psi} \tag{4.32}$$

on the elliptic boundary.

Making use of several identities given in Ting (1996), the generalized potentials in the matrix and inclusion can be written in the following form on the elliptic boundary,

$$\begin{bmatrix} \mathbf{u}_\Gamma \\ \varphi_\Gamma \end{bmatrix} = a\cos\psi \begin{bmatrix} \Omega_1^\infty \\ \Sigma_2^\infty \end{bmatrix} + b\sin\psi \begin{bmatrix} \Omega_2^\infty \\ -\Sigma_1^\infty \end{bmatrix} + \cos\psi \begin{bmatrix} \mathbf{h} \\ \mathbf{g} \end{bmatrix} - \tilde{\mathbf{N}}\sin\psi \begin{bmatrix} \mathbf{h} \\ \mathbf{g} \end{bmatrix} \tag{4.33}$$

$$\begin{bmatrix} \mathbf{u}_\Gamma^o \\ \boldsymbol{\varphi}_\Gamma^{\mathbf{o}} \end{bmatrix} = a\cos\psi \begin{bmatrix} \Omega_1^o \\ \Sigma_2^o \end{bmatrix} + b\sin\psi \begin{bmatrix} \Omega_2^o \\ -\Sigma_1^o \end{bmatrix} \tag{4.34}$$

The matrix $\tilde{\mathbf{N}}$ is composed of the Barnett-Lothe tensors which are related to the Stroh eigenvectors by the following relation,

$$\tilde{\mathbf{N}} = \begin{bmatrix} \mathbf{S} & \mathbf{H} \\ -\mathbf{L} & \mathbf{S}^T \end{bmatrix} = 2i \begin{bmatrix} \mathbf{A}\mathbf{B}^T & \mathbf{A}\mathbf{A}^T \\ \mathbf{B}\mathbf{B}^T & \mathbf{B}\mathbf{A}^T \end{bmatrix} - i\mathbf{I} \tag{4.35}$$

This is a compact form of Equations (4.15a,b,c).

The interface along the elliptic boundary is assumed to be perfectly bonded, therefore the displacement and electric potential are continuous. The traction and normal component of electric displacement are also continuous across the boundary. This can be satisfied by forcing the generalized stress potential in the matrix and inclusion to be equal along the boundary. The integration constant that arises from integrating traction and electric displacement to find the potential can be set to zero. The boundary condition constants **h** and **g** are then satisfied by fulfilling Equation (4.36).

$$\begin{bmatrix} \mathbf{u}_\Gamma \\ \varphi_\Gamma \end{bmatrix} = \begin{bmatrix} \mathbf{u}_\Gamma^o \\ \varphi_\Gamma^o \end{bmatrix} \tag{4.36}$$

Once the boundary conditions are satisfied, the stress and electric displacement components previously given by Equations (3.45b) and (3.46b) can be applied to the microcrack problem. The stress and electric displacement that would act on the crack surface illustrated in Figure 4.1 is given by Equation (4.37).

$$\Sigma_{i2} = \varphi_{i,1} \quad \text{for } i=1 \text{ to } 3 \tag{4.37}$$

Equation (4.37) includes the uniform fields far away from the inclusion and the field concentration near the inclusion. In the following section, the stress and electric displacement from Equation (4.37) are applied to the piezoelectric weight function to ascertain the influence of heterogeneities on the intensity factors and energy release rate.

Piezoelectric Weight Functions

The utility of the piezoelectric weight function method is that it allows electro-mechanical loading to be applied onto a crack surface or some predefined contour

surrounding a crack so that contributions to intensity factors can be assessed. For the elastic case, the procedure uses two loading scenarios on the same crack geometry. In the first problem, traction is applied at the external boundary far removed from the crack and the crack tip displacement profile is determined. This solution is known from elasticity. In the second problem, the load is applied on the crack face which is related to some displacement on the external boundary. This solution is unknown. By comparing the two problems through the use of Maxwell's relations, the solution to the second problem is found. This is the weight function method given by Rice (1972) for elastic materials and extended to piezoelectrics by McMeeking and Ricoeur (2003). Key equations relevant to determining driving forces for crack propagation from an inclusion are presented.

The stress intensity factors are determined from the weight function ($k(x_i^S)$) by integrating the traction ($t_2(x_i^S)$) over some contour designated as S. The superscript S refers to points along the contour. This is given in Equation (4.38) for Mode I stress intensity in elastic materials.

$$K_I = \int_S k(x_i^S) t_2(x_i^S) dS \tag{4.38}$$

In the case of the center crack panel, the piezoelectric weight function can be represented in the following form,

$$\mathbf{k}(x_1) = \frac{\pm 1}{2\sqrt{\pi c}} \sqrt{\frac{c + x_1}{c - x_1}} \mathbf{I} \tag{4.39}$$

where 2c is the crack length in the center crack panel, **I** is the identity matrix and **k**~diag[k_1, k_2, k_3]. Thus the weight function in piezoelectric materials is independent of anisotropy for the two-dimensional case. The ± accounts for the top and bottom surface of the crack face. The x_1 coordinates are the same as the ones given in Figure 4.3. This function is only valid for loading on the crack face. Electro-mechanical loading along a contour introduces material dependence.

To determine the influence of heterogeneities on the fracture behavior, the stress and electric displacement from the inclusion solution given in Equation (4.37) is applied along the crack face shown in Figure 4.2. The intensity factors are determined by integrating along the crack face,

$$\begin{Bmatrix} K_{II} \\ K_I \\ K_{IV} \end{Bmatrix} = \frac{1}{\sqrt{\pi c}} \int_a^c \sqrt{\frac{c + x_1}{c - x_1}} \begin{Bmatrix} \sigma_{12}(x_1) \\ \sigma_{22}(x_1) \\ D_2(x_1) \end{Bmatrix} dx_1 + \frac{1}{\sqrt{\pi c}} \int_{-c}^{-a} \sqrt{\frac{c + x_1}{c - x_1}} \begin{Bmatrix} \sigma_{12}(x_1) \\ \sigma_{22}(x_1) \\ D_2(x_1) \end{Bmatrix} dx_1 \tag{4.40}$$

Crack Face Boundary Conditions

In the present analysis, it will be assumed that the cracks emanating from the edge of the inclusion can be modeled as a slit crack with no mechanical bridging between the crack face such that all stress components vanish, (Hao and Shen 1994; McMeeking and Ricoeur 2003). Equation (4.40) assumes the crack face boundary conditions are impermeable which have been stated to be unphysical. The inclusion of permittivity on in the crack volume requires a modification of the intensity factors and is given by Equation (4.41).

$$\begin{Bmatrix} K_{II} \\ K_{I} \\ K_{IV} \end{Bmatrix} = \frac{1}{\sqrt{\pi c}} \int_{a}^{c} \sqrt{\frac{c+x_1}{c-x_1}} \begin{Bmatrix} \sigma_{12}(x_1) \\ \sigma_{22}(x_1) \\ D_2(x_1) - D_2^*(x_1) \end{Bmatrix} dx_1 + \frac{1}{\sqrt{\pi c}} \int_{-c}^{-a} \sqrt{\frac{c-x_1}{c+x_1}} \begin{Bmatrix} \sigma_{12}(x_1) \\ \sigma_{22}(x_1) \\ D_2(x_1) - D_2^*(x_1) \end{Bmatrix} dx_1 \tag{4.41}$$

where $D_2^*(x_1)$ is the electric displacement normal to the permeable crack face ($D_2^* n_2 = -\omega_-^c$). Following the method of Hao and Shen (1994), the electric displacement inside the crack volume can be determined from the change in potential and mechanical displacement across the crack face. This gives the electric field inside the crack volume. The electric displacement can then be determined by multiplying the field by the

permittivity of the material in the gap. The gap is assumed to be in a vacuum such that the elastic stiffness is zero and the dielectric constant is the permittivity of free space.

The jump in displacement and electric potential across the crack face is represented in the following form,

$$\begin{bmatrix} \Delta u_1 \\ \Delta u_2 \\ \Delta \phi \end{bmatrix} = 4\sqrt{c^2 - x_1^2} \begin{bmatrix} H_{11} & H_{12} & H_{13} \\ H_{21} & H_{22} & H_{23} \\ H_{31} & H_{32} & H_{33} \end{bmatrix} \begin{bmatrix} \sigma_{12}(x_1) \\ \sigma_{22}(x_1) \\ D_2(x_1) - D_2^*(x_1) \end{bmatrix} \tag{4.42}$$

where [*H*] is the Irwin matrix and $\begin{bmatrix} \sigma_{12}(x_1) & \sigma_{22}(x_1) & D_2(x_1) \end{bmatrix}^T$ are the field components from Equation (4.37). The displacement and potential change across the crack face is defined as $\Delta u_i = u_i(x_1,+0) - u_i(x_1,-0)$.

The electric field is determined by the following relation,

$$E_2^*(x_1) = -\frac{\Delta \phi}{\Delta u_2} = -\left(\frac{H_{3i}\Sigma_{i2}(x_1) - H_{33}D_2^*(x_1)}{H_{2i}\Sigma_{i2}(x_1) - H_{23}D_2^*(x_1)} \right) \tag{4.43}$$

where the stress and electric displacement, $\Sigma_{i2}(x_1)$ along the crack face again refers to Equation (4.37).

The electric displacement inside the crack volume, $D_2^* = \kappa_o E_2^*$, can now be determined in terms of the applied loads from the relation given by,

$$D_2^*(x_1) = \frac{1}{2H_{23}}\left[H_{2i}\Sigma_{i2}(x_1) - \kappa_o H_{33} \pm \sqrt{(\kappa_o H_{33} - H_{2i}\Sigma_{i2}(x_1))^2 + 4\kappa_o H_{23}H_{3i}\Sigma_{i2}(x_1)}\right] \tag{4.44}$$

where the negative in front of the radical is used. For the material properties investigated, the plus sign in front of the radical gives a larger electric displacement on the crack surface relative to the applied surface charge which is deemed unphysical. Unlike the center crack problem described by Hao and Shen (1994), the electric field and electric displacement are not constant inside the crack volume due to the interaction with the inclusion. It should be noted that the field intensification at the interface where the crack face meets the inclusion was neglected. It is assumed that the field intensity at the crack tip dominates the fracture behavior.

Equations (4.40) and (4.41) are compared in the following section to quantify how inclusion-type flaws affect the intensity factors and energy release rate.

Numerical Results

Numerical analyses are presented to elucidate how electric fields can influence fracture when material inhomogeneities are present. A myriad of different combinations of material properties could be assessed. For example, rotations in material tensor to account for mismatch in grain orientation or proportional changes in material coefficients. Mismatch in grain orientation can induce mix-mode loading while a proportional increase in piezoelectric coefficients in the inclusion can increase or decrease Mode I loading. A proportional change in material coefficients is chosen for the numerical analysis such that the Mode I intensity increases near the inclusion. This was used to illustrate regions where microfracture may be more likely to occur.

Material properties for two different compositions of lead zirconate titanate were used. Tabulated piezoelectric and dielectric coefficients given by Jaffe et al. (1971) were used in the present work. It is assumed that the mole % of $PbZrO_3$ may range between 48% and 52%. PZT containing 52% $PbZrO_3$ is closer to the morphotropic boundary resulting in an increased number of variants which allows the material to be poled more completely thus providing stronger piezoelectric coupling. This change in composition resulted in an approximate 50% change in the d_{22} coefficient (again following the fracture mechanics literature by using the x_2 direction as the poling direction). The validity of applying these material properties at the microscopic scale within a small inclusion or grain is discussed in the following section. A complete list of the material properties used in the analysis is given in Table 4.1. The material coefficient for s_{12}^E was only given

for 52% $PbZrO_3$ by Jaffe et al. It was assumed to be the same for the composition with 48% $PbZrO_3$. Variations in elastic coefficients between the two compositions were found to have a minimal effect on the intensity factors and energy release rate.

Table 4.1: Material properties used in evaluating microfracture under applied electric fields. The matrix properties are assumed to possess 48% $PbZrO_3$ and the inclusion contains 52% $PbZrO_3$. Permittivity of free space is defined by κ_o.

PZT material coefficients	**48% $PbZrO_3$**	**52% $PbZrO_3$**
$\kappa_{22}^{\sigma} / \kappa_o$	700	750
$\kappa_{11}^{\sigma} / \kappa_o$	1300	1200
d_{22} 10^{-12} (C/N)	100	250
d_{21}	-50	-100
d_{16}	175	500
s_{11}^{E}, 10^{-12} (m^2/N)	11.1	14.3
s_{22}^{E}	11.1	16.7
s_{12}^{E}	-5.8	-5.8
s_{66}^{E}	28.6	50.0

In the first analysis, electro-mechanical loading is used to show changes in Mode I stress intensity due to residual fields near the inclusion when an electric field is present. The piezoelectric weight function given by Equation (4.40) is used. Unless otherwise

noted, all the analyses assume a circular inclusion to simplify the study. The inclusion is assumed to have the larger piezoelectric coupling as a worst case scenario. The stress intensity is normalized with respect to the center crack panel stress intensity ($K_I^{CCP} = \sigma_{22}^{\infty}\sqrt{\pi c}$).

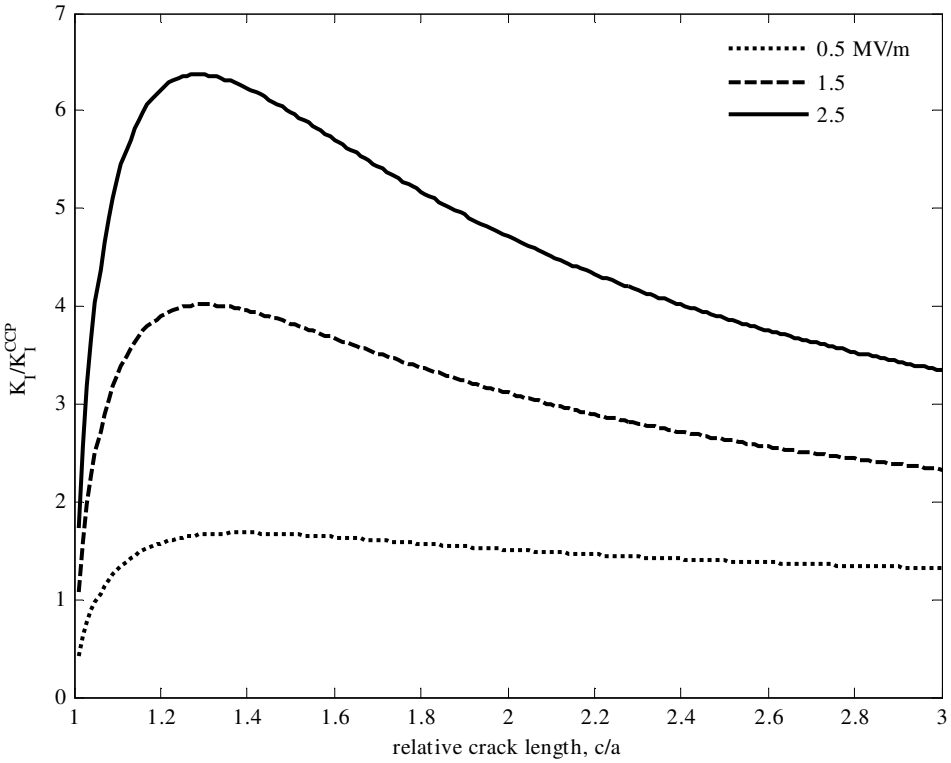

Figure 4.4: Normalized Mode I stress intensity factor vs. relative crack length given in Figure 4.1. The external loading consists of constant mechanical loading σ_{22}^{∞} while varying the electric field E_2^{∞} .

An increase in the Mode I stress intensity factor was predicted under positive electric field loading when the inclusion is present. As the crack length increases, the contribution from the inclusion asymptotically approaches zero and the stress intensity approaches the center crack panel value as expected. Although the Mode I stress intensity is coupled to electric field loading when an inhomogeneity is present, the result has neglected the negative driving force from charges on the crack face. A full assessment of the energy release rate is required to determine if certain an inhomogeneity provide a positive driving force for crack growth under electrical loading.

First, the impermeable crack is evaluated. Although this assumption is unphysical, it demonstrates the largest magnitude of negative driving force expected under electrical loading. Figure 4.5 illustrates the change in applied energy release rate (G_a) under an applied electric field. When impermeable boundary conditions are assumed, the applied energy release rate is always negative using the material properties in Table 4.1. This contradicts the majority of the data on electrically induced fracture which motivates the necessity for investigating the permeable crack.

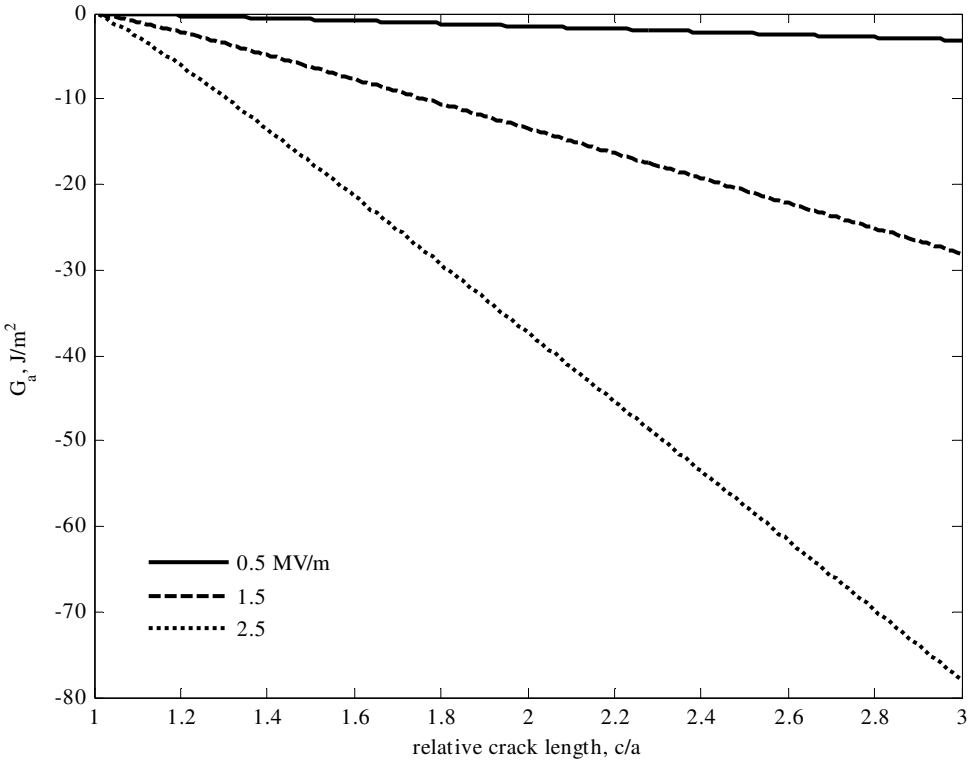

Figure 4.5: Driving force for crack propagation relative to crack length for the impermeable crack. Only electrical loading is considered. The applied energy release rate is always less than zero.

Permeable crack face boundary conditions create a significant difference in the applied energy release rate. The reduction in electric displacement intensity from charge compensation on the crack surface increases the flaw-localized driving force due to the dominance of Mode I intensity near the inclusion. Far away from the inclusion, the applied energy release rate becomes negative similar to Figure 4.5.

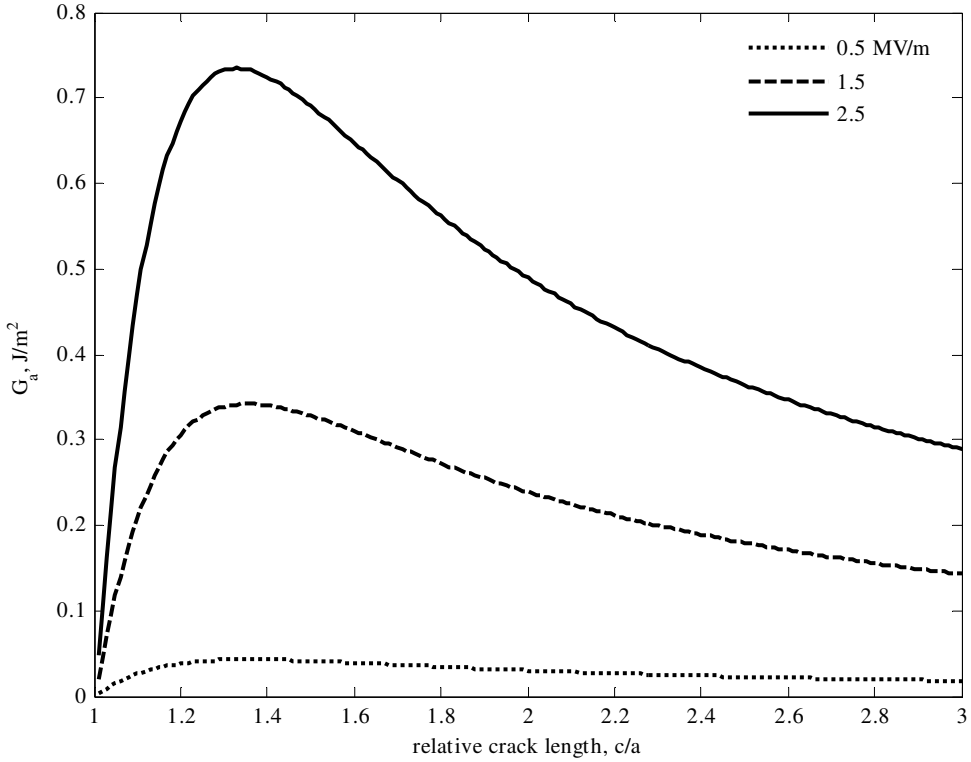

Figure 4.6: Driving force for crack propagation under electrical loading for the permeable crack. The applied energy release rate gives a positive driving force near the inclusion.

Figure 4.7 illustrates the influence of proportionally varying all three piezoelectric coefficients equally in the inclusion while holding all other coefficients constant. The energy release rate is reasonably sensitive to changes in piezoelectric coupling under an electric field of 1 MV/m, although the relative crack length at the minimum remains approximately constant.

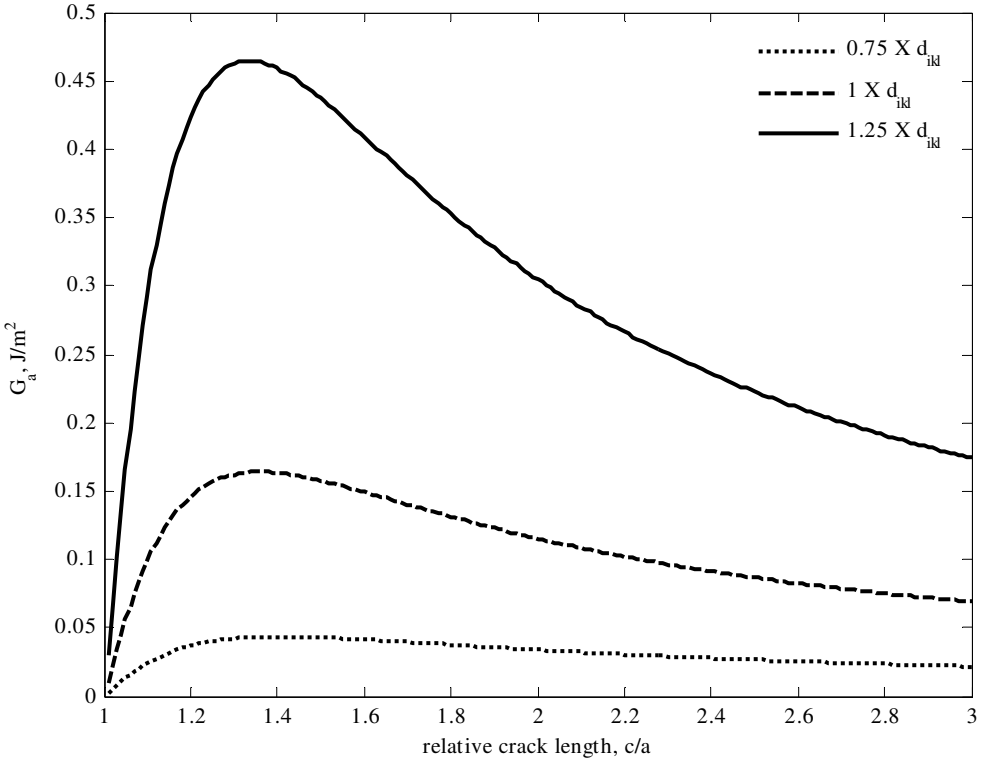

Figure 4.7: Change in energy release rate when the piezoelectric coefficients are varied in the inclusion. The coefficients were varied from 75% to 125% from the tabulated values given in Table 4.1. An electric field of 1 MV/m was used.

The effect of changes in aspect ratio of the elliptic inclusion (b/a) on the energy release rate is illustrated in Figure 4.8. As the aspect ratio increases the applied energy release increases. The relative crack length at the maximum value also increases.

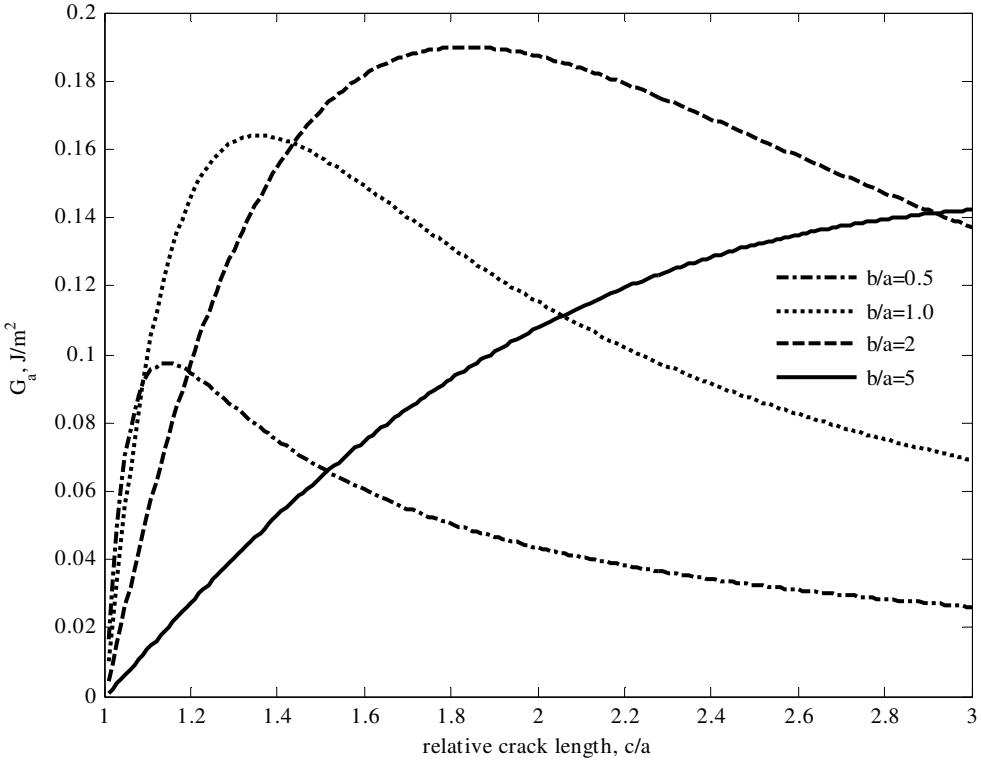

Figure 4.8: Effect of aspect ratio (b/a) on the critical inclusion size for cracks to form under an electric field of 1 MV/m.

Discussion

The theoretical model compares reasonably well with several experimental investigations found in the literature (Jiang et al. 1994; Lynch 1998; Wang et al. 1998). However, the role of material processes can lead to conflicting trends between grain size, piezoelectric properties, and intrinsic vs. extrinsic effects (Randall et al. 1998; Zhang and Raj 1995). In the present analysis, approximations on local properties are used which are

based on comparisons of macroscropic / microscopic constitutive behavior and micrographs of grain structures, (Hoffman et al. 2001; Wang et al. 1998).

Pores and foreign particles can also influence fracture toughness along grain boundaries. This was experimentally observed by Tan et al. (2000) in PZT TEM specimens and by Wang et al. (1998) in PZT transducers. Cracks tended to originate at pores or glassy phase inhomogeneities and propagate along grain boundaries. In Tan's result, the electric field within a pore was estimated by the ratio of dielectric permittivity in the piezoelectric material and the matrix. Using the piezoelectric inclusion model and substituting the glass material properties in the inclusion, significant increases in electric field are predicted within the inclusion. Under moderately low applied fields, the field within the inclusion approaches the dielectric breakdown of glass as the aspect ratio b/a shrinks. The field within the inclusion is approximately proportional to the inverse aspect ratio (a/b). For example, the field within the inclusion is approximately 100 MV/m for an applied field of 1 MV/m with a/b=100. If dielectric breakdown occurs, dynamic effects from rapid electric discharge could potentially contribute to intergranular or transgranular crack propagation. Large electrical currents during electric discharge may also lead to high thermal gradients which could severely reduce the interface fracture energy.

The critical energy release rate at the onset of fracture in PZT is approximately 7 J/m^2 For comparison, the critical energy release rate in glass is approximately 1 J/m^2 (Lawn 1975). This may reduce the interfacial fracture energy in regions where glassy phase particles are present. The applied energy release rate shown in Figure 4.6 does not

approach the critical energy release rate at fields as high as 2.5 MV/m. The present analysis neglected any initial residual stress that may be present from phase transformations from paraelectric cubic to ferroelectric rhombohedral or tetragonal. Moreover, inhomogenous switching during the poling process may contribute to localized stress concentrations. More work is required to quantify how phase transformations and localized domain switching contribute to flaw-localized driving forces.

The aspect ratio of the inclusion was shown to also play an important role in microfracture under electric fields (Figure 4.8). The driving force for crack propagation is affected by the aspect ratio (b/a). The energy release rate reaches a maximum near b/a=2 and then reduces and broadens as the aspect ratio continues to increase. The aspect ratio has implications on the development of textured ceramics. The templated grain growth process has recently been investigated by Sabolsky et al. (2003) on PMN-PT textured ceramics which provided piezoelectric coupling close to the single crystal value. The grains contained within these materials are elongated in the direction of poling (b/a>1). An increase in hysteresis on the strain vs. electric field unipolar cycling was observed after 50,000 cycles. The large anisotropy and aspect ratio of grains suggest microfracture may play a dominant role in the observed hysteretic behavior.

Conclusions

Microfracture induced by electric field was shown to increase the Mode I fracture toughness as well as the energy release rate for the permeable crack. This was due to

residual stress under electric fields when an inclusion with dissimilar piezoelectric matrix properties is present. The more "physical" permeable crack face boundary condition was necessary to achieve a positive flaw-localized driving force for microcracking. Additionally, the aspect ratio of the inclusion appears to affect microfracture which may have a strong impact on reliability of textured ferroelectrics.

CHAPTER V

SUBCRITICAL CRACK GROWTH IN FERROELECTRIC CERAMICS

Subcritical crack growth in terms of velocity – stress intensity factor (v-K) curves in lead zirconate titanate (PZT) has been experimentally characterized on poled and unpoled compact tension specimens. The poled specimens were tested under open and short circuit electrical boundary conditions, which resulted in an increase in fracture toughness of 0.2 MPa m ^{½} for the accessible velocity range (v=10^{-9} to 10^{-4} m/s) in the open circuit case. Subcritical crack growth of unpoled specimens was obtained under ambient (relative humidity=35%) and very dry conditions (relative humidity≅0.02%). The crack tip velocity increased by approximately one order of magnitude while exposed to ambient conditions for all applied stress intensity values.

Measurement Procedure

For materials where the shielding term is related to the magnitude of the stress intensity factor at the crack tip (process zone toughening), special care has to be taken to measure a unique v-K curve. This problem has been addressed in subcritical crack growth of transformation toughened materials (Knechtel et al. 1993), by ensuring that the relevant regions of the crack wake have been developed under a crack tip stress intensity identical in numerical magnitude to the current applied crack tip stress intensity. A

steady state crack velocity is obtained, once the part of the process zone relevant for crack tip shielding has been grown completely by the same crack velocity. This approach has been utilized by Lucato (2000) to obtain the first steady state crack velocities in unpoled PZT.

Crack velocity vs. stress intensity factor curves for PZT 151 (PI Ceramics, Lederhose, Germany, $Pb_{0.99}[Zr_{0.45}Ti_{0.47}(Ni_{0.33}Sb_{0.66})_{0.08}]O_3$) were measured using compact tension specimens in a fracture device mounted on the stage of an optical microscope. The specimens were unpoled plates of dimension 50 x 48 x 3 mm^3 that were polished to a 1 μm finish. The CT-samples were made from the polished PZT-plates. A chevron notch was placed in each specimen and a Vickers indentation was applied directly ahead of the notch to create a sharp precrack. The crack was initiated in a custom designed loading device (Rödel et al. 1991) and propagated through the chevron notch to obtain a constant crack length through the thickness of the specimen, see Figure 5.1.

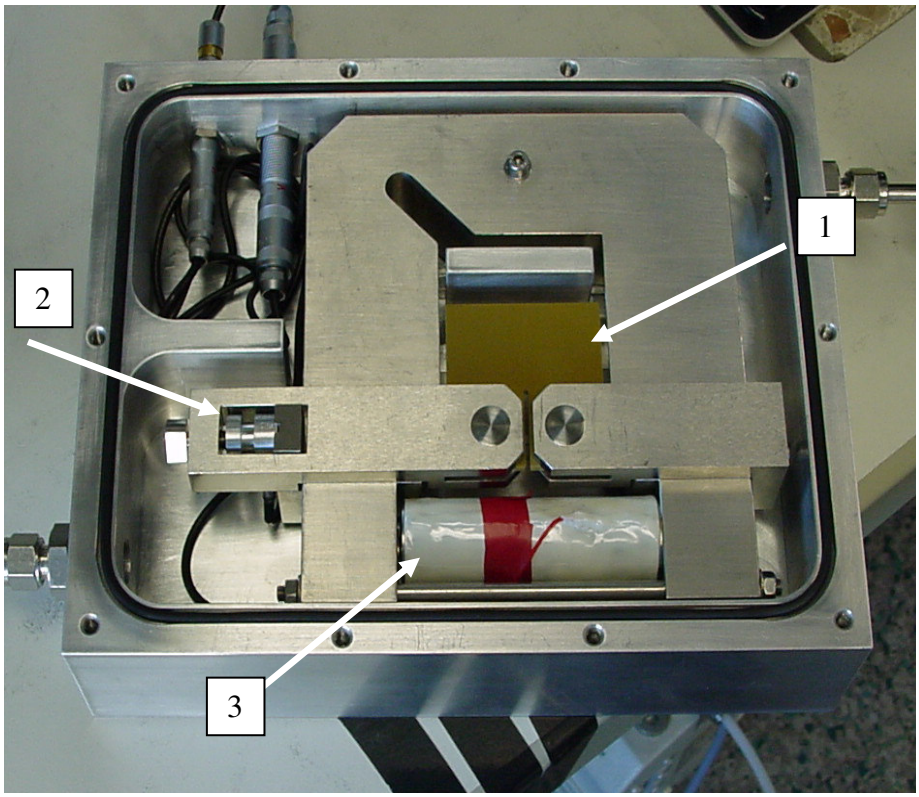

Figure 5.1: Custom design loading frame used to characterize subcritical crack growth in PZT PIC 151. Label (1) is the compact tension specimen, label (2) is the load cell, and label (3) is a piezoelectric stack actuator used to load the specimen. The outer casing was used to control the environmental conditions.

One measurement sequence was used to acquire a complete set of v-K data for one specimen. Initially, a load was applied to obtain the lowest velocity measured ($v \cong 10^{-10}$ m/s). The load was continuously adjusted to obtain constant crack velocity. The increase in toughness by going up the R-curve was measured by acquiring points in increments of 20 μm during crack propagation, thereby minimizing scatter due to the spatial variation in microstructure. Once the stress intensity factor was constant, the crack velocity required no further adjustment and several additional data points were

acquired. The procedure was repeated for each velocity, going step-wise to higher velocities. As the velocity was increased, a wider process zone was obtained, providing increased toughening. The stress intensity factor was evaluated according to the ASTM standard (1979).

Electrical Boundary Conditions

The electrical boundary condition experiments were conducted on poled specimens in ambient air (T=23°C and RH=35%). Electrodes were sputtered on the large faces of each short circuit specimen. Electrodes were painted on the open circuit specimens using silver paint and then removed after poling. The specimens were poled at 2 MV/m in the thickness direction. The electric field was applied in silicone oil in order to avoid electrical breakdown or arcing during poling.

The electrical boundary conditions were controlled by removing the electrodes in the open circuit case. In the short circuit case, the sputtered electrodes remained on the top and bottom surfaces. Once the short circuit specimens were inserted into the fracture device, the metallic loading arms short circuited the specimen through the thickness.

Relative Humidity

The "dry" air (RH≅0.02%) experiments were conducted in a sealed container with Argon (99.998% of purity) gas flowing through the system, see Figure 5.2. Prior to

testing, the fracture device and sealed container were cleaned with methanol. After inserting the specimen into the device, the system was evacuated and purged with Argon several times. The gas was filtered to reduce the amount of water by approximately an order of magnitude. A pressure regulator was used to control the Argon flow rate.

Unpoled PZT specimens were used in characterizing crack velocity dependence on stress intensity factor. The specimens were exposed to normal laboratory conditions (T=23°C and RH=35%) and "dry" air conditions (T=23°C and RH≅0.02%). All tests were conducted using the same loading device. v-K curves were run on two glass specimens and compared to Wiederhorn's published curves (Wiederhorn 1974) to approximate the relative humidity. Two unpoled PZT specimens were measured under ambient laboratory conditions. One of the specimens was tempered at 400°C for 8 hours and one was tested without tempering. The specimen tempered at 400°C was exposed to ambient conditions for 24 hours prior to testing. Three specimens tested in "dry" air conditions were tempered at 400°C for 8 hours. After tempering, each specimen was directly inserted into the fracture device to minimize water absorption on the specimen surface.

Figure 5.2: Sealed container and microscope set-up used to characterize environmental sensitivity on the contact tension specimens. Argon flowed through the device to control the relative humidity.

Two additional specimens were tested in "dry" air after tempering the specimens at 180°C for 8 hours. The specimens were stored in desiccant under a vacuum prior to testing. Table 5.1 summarizes the tests conducted.

Table 5.1: Test matrix for the v-K measurements conducted on poled and unpoled PZT compact tension specimens.

PZT PIC 151	Unpoled			Poled	
Electric Boundary Conditions	--	--	--	Short Circuit	Open Circuit
Tempering conditions (~8 hrs.)	No heat treatment	180°C	400°C	No heat treatment	No heat treatment
Ambient conditions (T=23°C, RH=35%)	1		1	1	2
"Dry" air (T=23°C, RH≅0.02%)		2	3		

Results and Discussion

General Observations

One specimen yielded a complete v-K curve. This was accomplished by adjusting the applied load to run the crack at a constant velocity until the plateau of the R-curve was reached. Once the plateau was reached and data recorded, the load was increased to obtain faster crack growth. After some length of growth a new R-curve plateau was reached and data was recorded. The data set recorded for a single specimen is shown in Figure 5.3 for an unpoled specimen exposed to ambient environmental conditions. Only the last two points from each velocity were plotted on the v-K curve for clarity.

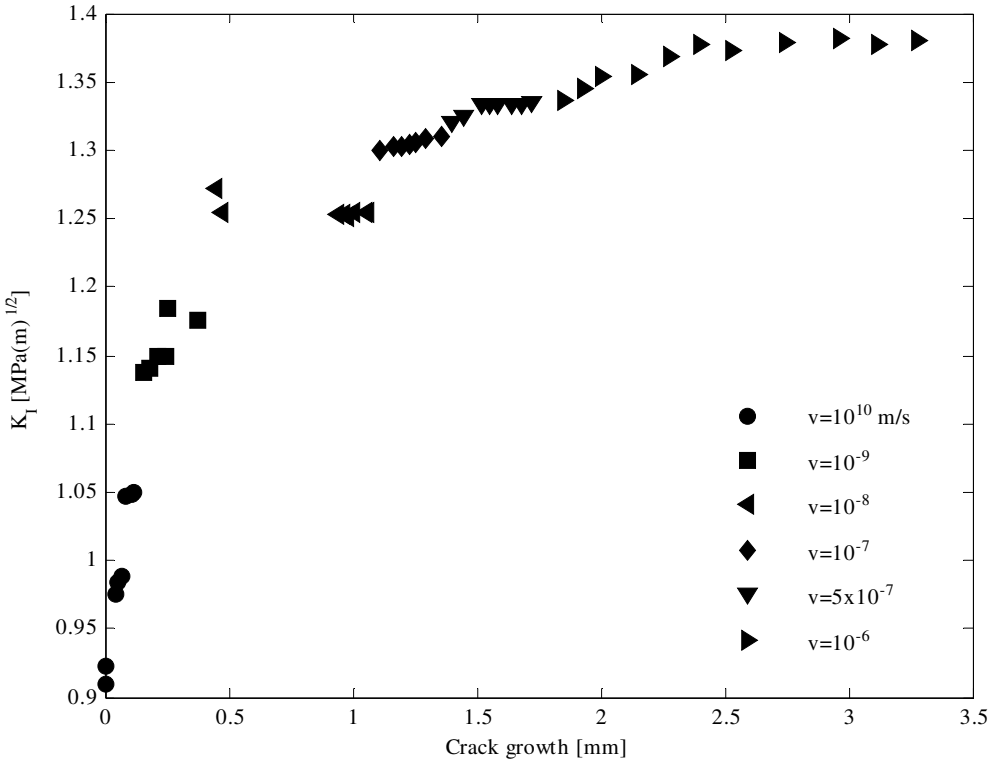

Figure 5.3: This graph quantifies the method to obtain a steady state process zone. Each new chosen velocity required attainment of a new steady state process zone. The data represents toughening behavior measured during a v-K measurement on one unpoled PZT compact tension specimen exposed to ambient laboratory conditions (T=23°C and RH=35%).

The obtained experimental results were analyzed using a power law relation, Equation 5.1. A linear regression model was used in log space to calculate the variance (square of the standard deviation σ^2) (Hayter 1996). The fitting parameters (A, n) and variance are provided in Table 5.2.

$$v(K) = AK^n \tag{5.1}$$

Table 5.2: Measurement uncertainty using a linear regression model in log space for the power law dependence, $v(K) = AK^n$.

Test conditions	specimens tested	specimen characteristics	A	n	σ^2
T=23°C, RH=35%	1	poled, short circuit	$6.53 \cdot 10^{-9}$	27.7	0.56
T=23°C, RH=35%	2	poled, open circuit	$9.42 \cdot 10^{-12}$	35.8	1.87
T=23°C, RH=35%	2	unpoled*	$3.55 \cdot 10^{-10}$	28.8	1.23
T=23°C, RH≅0.02%	2	unpoled, heat treated 180°C	$1.50 \cdot 10^{-9}$	25.2	1.44
T=23°C, RH≅0.02%	3	unpoled, heat treated 400°C	$2.57 \cdot 10^{-11}$	24.0	1.50

*One specimen was heat treated at 400°C. The other specimen was not heat treated.

Electrical Boundary Conditions

The v-K curves for the electric boundary conditions in ambient environment are given in Figure 5.4. An increase in fracture toughness was observed in the open circuit case for the crack velocity range 10^{-10} to 10^{-4} m/s.

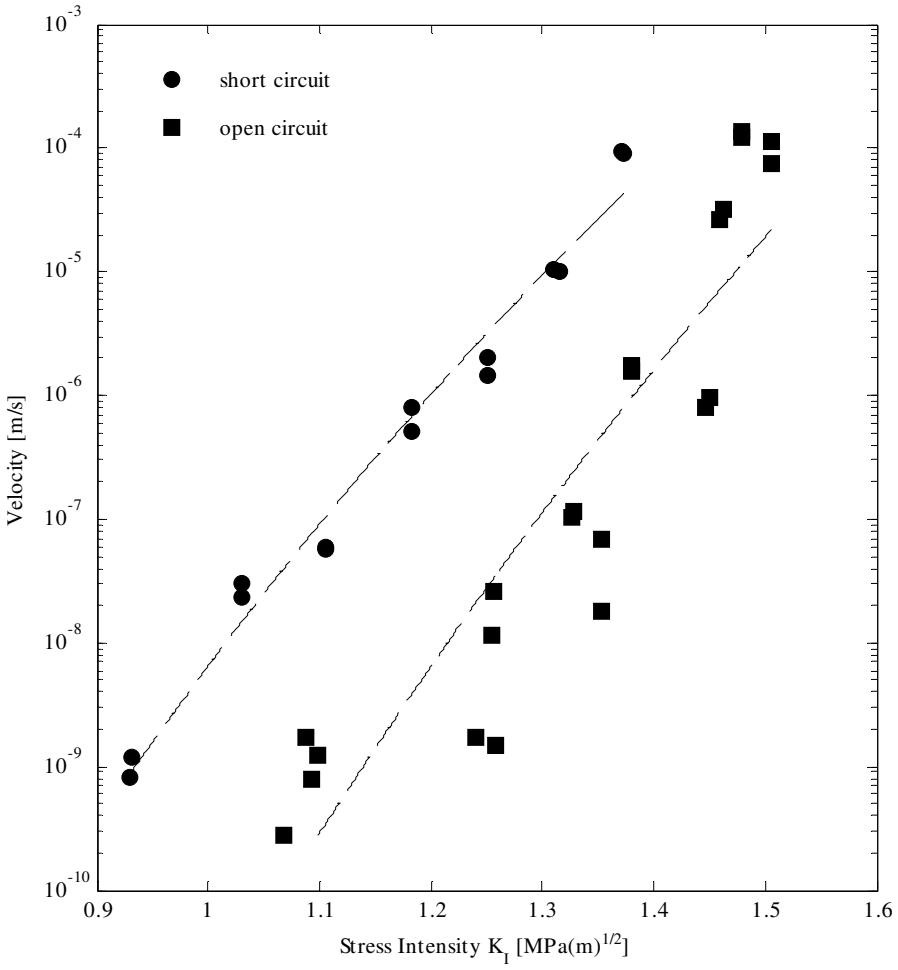

Figure 5.4: Crack velocity curves for poled (thickness direction) PZT compact tension specimens exposed to open and short circuit boundary conditions (T=23°C and RH=35%). Regression curves are provided as fits through the data.

The compact tension specimen can be considered short circuit in all directions when electrodes are applied perpendicular to the thickness direction. The electrodes provide enough free charge carriers to compensate for charge build up through the specimen thickness due to ferroelastic switching near the crack tip. In the open circuit

case, a positive depolarization field develops in the poling direction as domains switch perpendicular to the crack surface.

The switching criterion developed by Hwang et al. (1995) is utilized to illustrate how a depolarization field under open circuit boundary conditions will affect the switching behavior. Only a ferroelastic switching barrier is considered,

$$\sigma_{ij}\Delta\varepsilon_{ij} + E_i\Delta P_i \geq \Psi_c \tag{5.2}$$

where σ_{ij} are the stress components, $\Delta\varepsilon_{ij}$ are the increments of strain, E_i is the electric field, ΔP_i is the change in polarization, and Ψ_c is the energy barrier required to mechanically switch domains.

The coercive stress necessary to switch domains is expected to rise under open circuit boundary conditions. As the polarization is reduced, a positive depolarization field develops, which requires additional mechanical work to switch additional domains against the depolarization field. The lower coercive stress under short circuit boundary conditions should lead to a larger process zone and higher toughness. Just the opposite was noted and verified with all specimens tested. It should be noted that these conclusions are based on one short circuit specimen and two open circuit specimens, although additional experiments were conducted by Njiwa (2003) who observed the same trend in toughness.

Wang and Landis (2004) recently identified a change in toughening mechanisms between unpoled specimens and short circuit specimens using nonlinear finite element simulations. It was shown that the additional variants available for switching in the thickness-poled short circuit specimen lead to a stronger plane strain effect than in the unpoled case. The plane strain condition lead to a slightly lower toughness in short circuit which corresponds to the trend observed in Figure 5.4. More work is required to assess the change in toughness for the open circuit case.

Relative Humidity

The v-K curves in Figure 5.5 represent the difference in fracture toughness between ambient laboratory conditions (RH=35%) and "dry" air conditions (RH≅0.02%). A constant shift on the K-axis of about 0.2 MPa $m^{1/2}$ at constant velocity can be observed. However, there is no manifestation of a plateau (regime II), as observed in glass at comparably low humidity (Wiederhorn 1974).

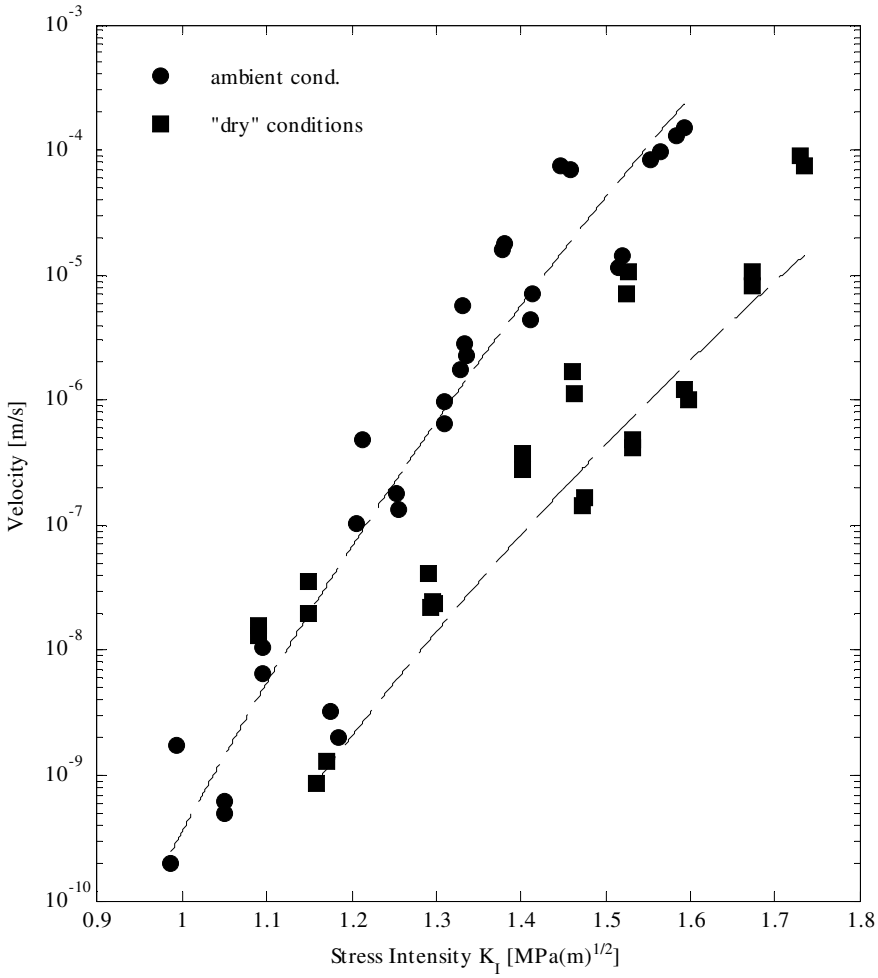

Figure 5.5: Crack velocity curves for unpoled PZT compact tension specimens exposed to ambient laboratory conditions (T=23°C and RH=35%) and "dry" air conditions (T=23°C and RH≅0.02%). The "dry" air specimens and one ambient specimen were heat treated at 400°C before testing. Regression curves are fit through the data.

An increase in stress intensity factor was observed when the material was tempered at 400°C and tested in "dry" air conditions at room temperature. The v-K measurements that were conducted on specimens tempered at 180°C resulted in no

difference in stress intensity factor relative to the virgin specimens. This may possibly be attributed to localized polarization occurring within each grain when the material transforms from cubic to the polar tetragonal and/or rhombohedral crystal structure. The Curie temperature for PZT is approximately 250°C (Moulson and Herbert 1990); therefore the energy barrier necessary to remove physically and chemically absorbed water molecules may be reduced at temperatures above the Curie point.

Conclusions

Crack kinetics in PZT was shown to be affected by electrical boundary conditions and relative humidity. Subcritical crack growth in poled PZT was shifted to higher stress intensity factors under open circuit conditions as compared to short circuit conditions. Higher stress intensity factors for the same crack velocity were also required when unpoled specimens were tempered to 400°C and tested in "dry" air conditions. Heat treatment above the Curie temperature may play an important role in eliminating chemically and physically absorbed water molecules in the material.

CHAPTER VI

ANISOTROPIC FRACTURE OF FERROELECTRIC SINGLE CRYSTALS

This chapter focuses on fracture behavior in unpoled and poled PZN-4.5%PT single crystal relaxor ferroelectrics cut along the crystal planes; [100], [010], and [001]. An assessment of anisotropy in both electro-elastic material coefficients and fracture toughness is made. The crack tip toughness (K_{tip}) measured from Vickers indentations was compared to the applied stress intensity using the Single Edge V-Notch Beam (SEVNB) method. Several of the SEVNB fracture experiments resulted in cracks forming and propagating under mixed mode loading (K_I and K_{II}) along the [110] crystal plane. Other specimens formed cracks at 0° along the [010] plane. To assess the fracture energy on the [010] and [110] planes, the local and global critical energy release rate was determined using Stroh's formalism. The result intimates a weak cleavage plane exist along the [110] crystal plane.

Experimental Methods

The fracture behavior of PZN-4.5%PT single crystals grown and cut by TRS[2] was characterized under mechanical loading. The specimens were cut into bend bars of nominal dimension 2.7 X 3.8 X 22 mm^3 along the [001], [010], and [100] crystallographic planes. Several specimens were poled by applying an electric field of 0.75 MV/m in the 2.7 mm direction while submersing the specimens in silicone oil. The specimens were polished to a 0.05 μm finish on the 3.8 X 22 mm^2 sides and tested using Vickers indentations and the Single Edge V-Notch Beam (SEVNB) method, (Kübler 1997). All experiments were conducted in open circuit.

The crack tip toughness and local energy release rate were compared to the applied stress intensity and global energy release rate from SEVNB measurements. Crack tip toughness has previously been shown to be invariant with specimen geometry based on crack profile comparisons in compact tension specimens and radial indentations of alumina (Seidel and Rödel 1997). It is assumed in the present analysis that Vickers indentations can be directly compared to the SEVNB method.

Crack Opening Profile Measurements

The crack opening profile was measured using scanning electron micrographs of Vickers indentations. The indentations were applied to two poled specimens using a load

[2] TRS Ceramics, Inc. State College, PA.

that ranged from 4.9 N to 9.8 N. The orientation of the Vickers indenter was rotated such that the diagonals of the indenter were parallel to the [110] direction in one specimen and the [100] direction in the other specimen, as shown in Figure 6.1. The crack opening profile was measured near the crack tip to determine crack tip toughness and local energy release rate. The measurements were taken within two hours of applying the indentation to minimize potential effects of subcritical crack growth.

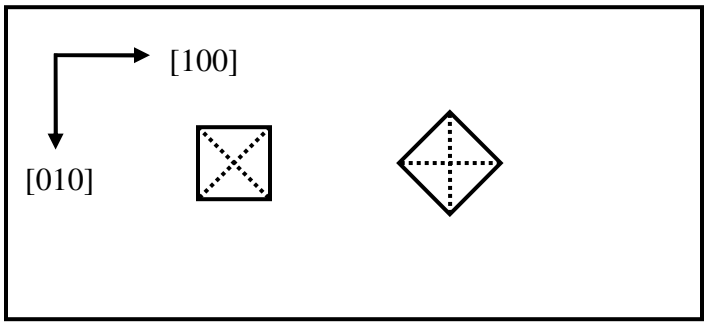

Figure 6.1: Configuration of the single crystal and Vickers indentation orientation used in quantifying the crack tip toughness and local energy release rate. The diagonals of the Vickers indentation were aligned along the [110] and [100] directions.

R-Curve Measurement Technique

PZN-4.5%PT single crystal bend bar specimens were notched using the (SEVNB) method, (Kübler 1997). A notch approximately 1.2 mm deep was machined into the 2.5 X 22 mm^2 side of the PZN-4.5%PT single crystal bend bar using a razor blade. Diamond paste with one micron particle size was used in the cutting procedure. A notch tip radius

of approximately 20 μm was obtained on all specimens. The bend bar specimens were inserted into a custom made four point bending device (Stech and Rödel 1996) having inner and outer spans of 10 mm and 20 mm and prestressed with a mechanical screw, see Figure 6.2.

In situ crack propagation was observed by mounting the loading device and specimen onto the X-Y positioning stage previously shown in Figure 5.2. Figure 6.3 illustrates the experimental arrangement. The load was slowly adjusted while viewing the notch under a high power optical microscope using transmitted polarized light. PZN-4.5%PT is transparent after polishing; therefore both 3.8 X 22 mm^2 sides were polished to aid in observation of subsurface incipient crack formation and growth. Once a crack formed, the load was continuously adjusted to maintain a nominal crack tip velocity of 1 μm/s. Load cell data was recorded as a function of crack length.

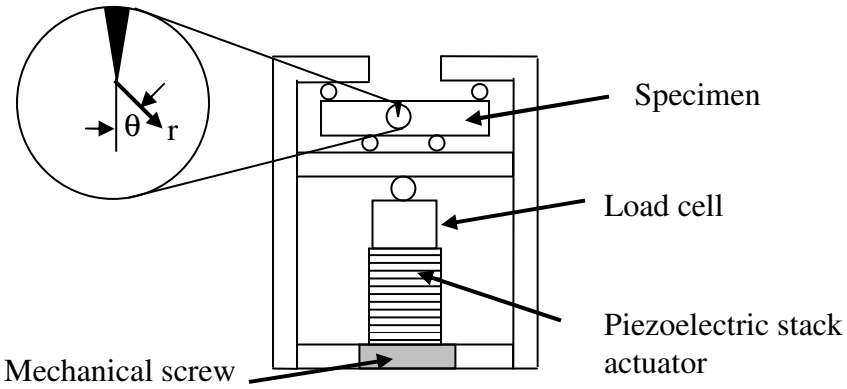

Figure 6.2: Four point loading device used in conducting fracture experiments on PZN-4.5%PT. The specimen is preloaded with a mechanical screw located underneath the piezoelectric stack actuator. The stack actuator controls the load applied to the bend bar.

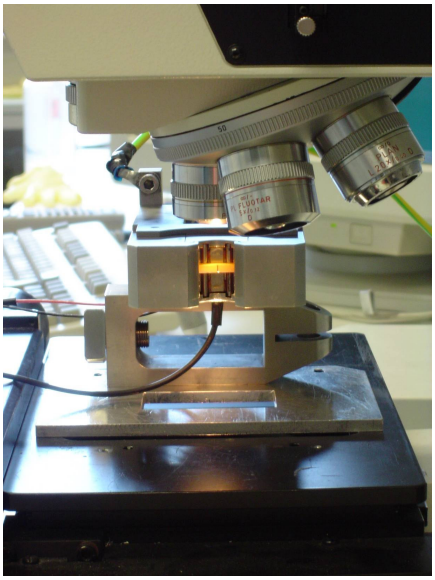

Figure 6.3: Experimental set-up for the SEVNB method. The four point bending device was placed on its side to view crack propagation in the bend bar specimens under the optical microscope using transmitted polarized light.

The stress intensity for cracks growing at 0° in SEVNB specimens is given by Equations (6.1) and (6.2), (Kübler 1997)

$$K_I = \frac{F}{B\sqrt{W}} \frac{S_1 - S_2}{W} \frac{3\sqrt{\alpha}}{2(1-\alpha)^{1.5}} Y^* \tag{6.1}$$

$$Y^* = 1.9887 - 1.326\alpha - (3.49 - 0.68\alpha + 1.35\alpha^2)\alpha(1-\alpha)(1+\alpha)^{-2} \tag{6.2}$$

where F is the load, B is the specimen width, W is the height, S_1 and S_2 are the outer and inner loading spans, respectively. The ratio of total notch and crack length is given by $\alpha=(a_N+a)/W$ where a_N is the notch length, a is the crack length starting at the notch. Y* is the geometric factor. The geometric factor given by Equation (6.2) was verified using the finite element package FRANC2D[3] for a notch radius of 20 μm. Linear elastic, quadrilateral elements with eight nodes were used in the model. Since anisotropy does not affect the intensity factor calculation (Sih et al. 1965; Ting 1996), isotropic properties were used to determine K_I and K_{II}. The error between the finite element analysis and the geometric function given by Kübler was less than 1.5% as long as the crack had extended more than 40 μm from the notch.

The mixed mode stress intensity factors, K_I and K_{II}, were determined for cracks oriented at 45°. The local coordinate system describing the crack growth direction is illustrated in Figure 6.2. Previous work by Munz and Fett (1999) determined the mixed

[3] FRANC2D vol. 3.1 Cornell University, www.cfg.cornell.edu/software/software.htm

mode stress intensity factors for bend bars with oblique cracks at various angles under four point bending. Their analysis did not include the effects of a notch. FRANC2D was used to assess the presence of a notch with a 45° crack. An illustration of the finite element model used is shown in Figure 6.4. A crack was inserted at the notch of the SEVNB specimen at a 45° angle. The crack was grown incrementally in FRANC2D to determine the functional dependence of crack length on the stress intensity. Tabular results for a given notch length are given in Appendix B.

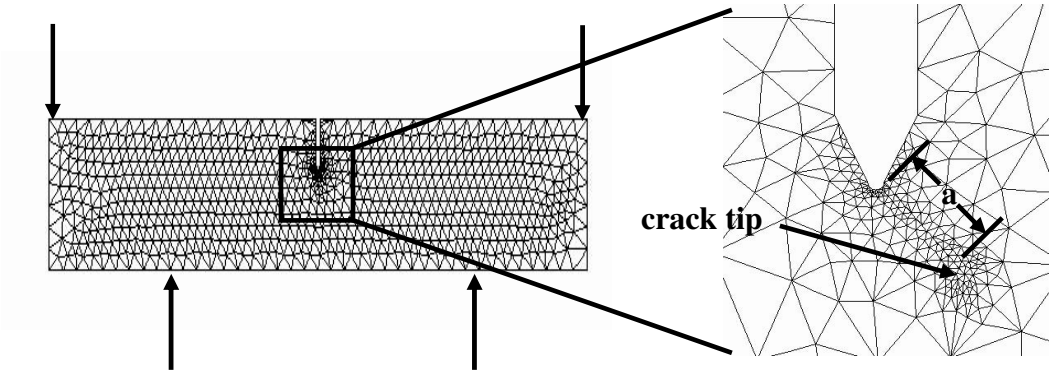

Figure 6.4: Finite element model used in determining the stress intensity factors K_I and K_{II} under four point bending.

Experimental Results

Crack Tip Toughness

The crack opening profile was measured from scanning electron micrographs of Vickers indentations. Images of the two indentations are given in Figure 6.5. The crack opening profile was found to be invariant to the two indentation orientations tested.

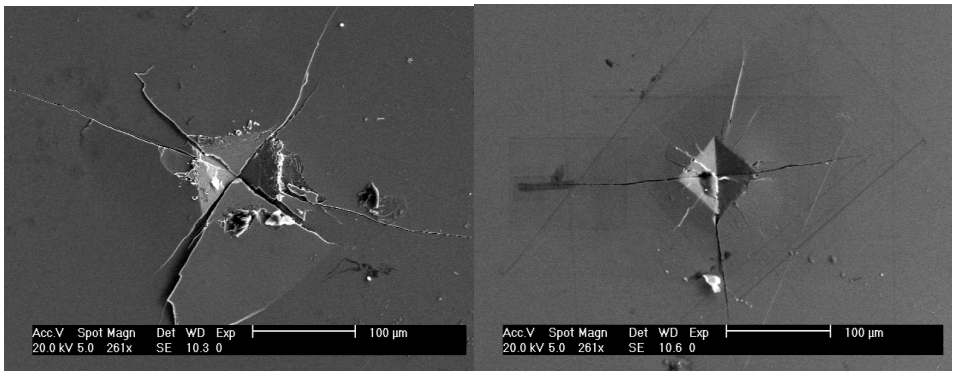

(a) (b)

Figure 6.5: Scanning electron micrographs of Vickers indentations in PZN-4.5%PT single crystals. A 9.8 N load was applied to the indentation in (a) with the diagonal aligned in the [100] direction. In (b), a 4.9 N load was applied with the diagonals aligned in the [110] direction.

SEVNB Measurements

R-curve behavior was characterized on five SEVNB specimens; three poled in the 2.7 mm direction and two unpoled specimens. Two poled specimens and one unpoled

specimen formed cracks at a ±45° angle ([110] or $[1\bar{1}0]$ plane). The remaining two specimens (one unpoled and one poled) formed cracks that propagated at a 0° angle ([010] plane). Optical images of the fracture behavior under transmitted polarized light are shown in Figures 6.6 and 6.7.

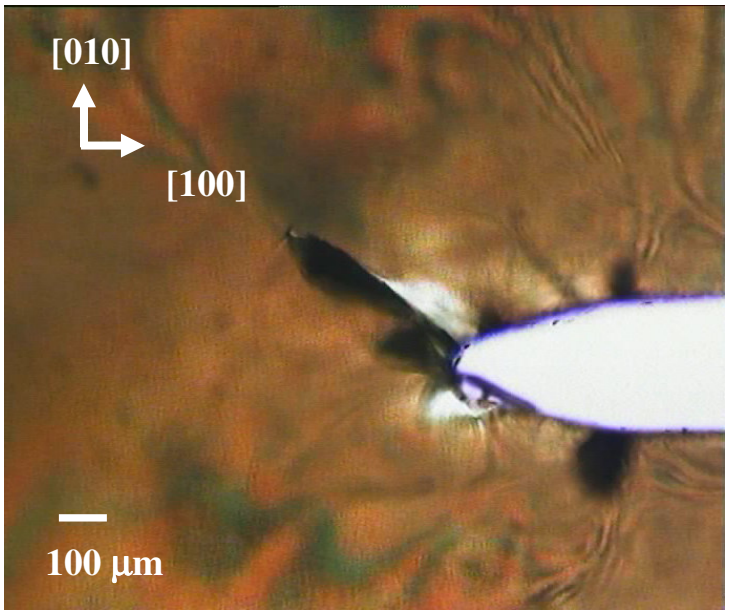

Figure 6.6: PZN-4.5%PT poled single crystal SEVNB specimen with a crack formed at 45° ([110] plane).

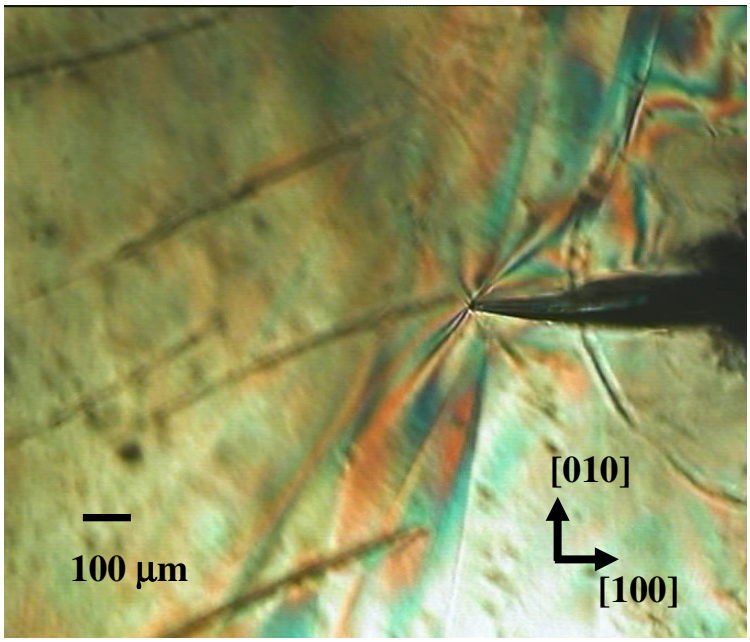

Figure 6.7: Unpoled PZN-4.5%PT single crystal SEVNB specimen with a crack formed at 0° ([010] plane).

Using the geometric functions from finite element analysis, the fracture toughness of angled cracks was quantified and compared to the toughness of cracks growing at a 0° angle. The Mode I fracture resistance (K_{IR}) vs. crack length for the poled and unpoled specimens is shown in Figure 6.8. A minimal amount of R-curve behavior was observed in the poled specimen with 0° crack propagation. All other specimens resulted in approximately flat R-curve behavior.

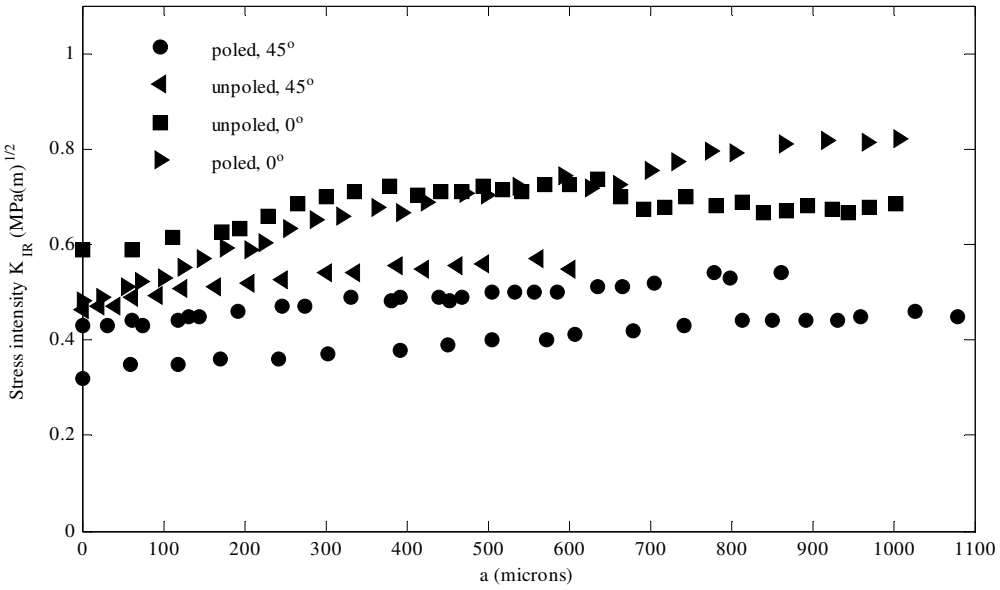

Figure 6.8: Mode I fracture resistance for SEVNB PZN-4.5%PT single crystal specimens. The angle represents the direction of crack propagation. The data includes two poled and one unpoled specimen with cracks growing at an angle of 45°. One poled and unpoled specimen formed cracks that propagated at 0°.

Although Mode I fracture toughness was significantly lower on the [110] plane, a full assessment of the fracture resistance requires the inclusion of the Mode II contribution. The Mode II fracture resistance corresponding to the specimens with angled cracks from Figure 6.8 is presented in Figure 6.9. A root mean square calculation of the toughness ($K_{RMS} = \sqrt{K_{IR}^2 + K_{IIR}^2}$) shows a 24% reduction in toughness on the [110] plane. Further evaluation using energy release rate given in the Analysis section supports this result.

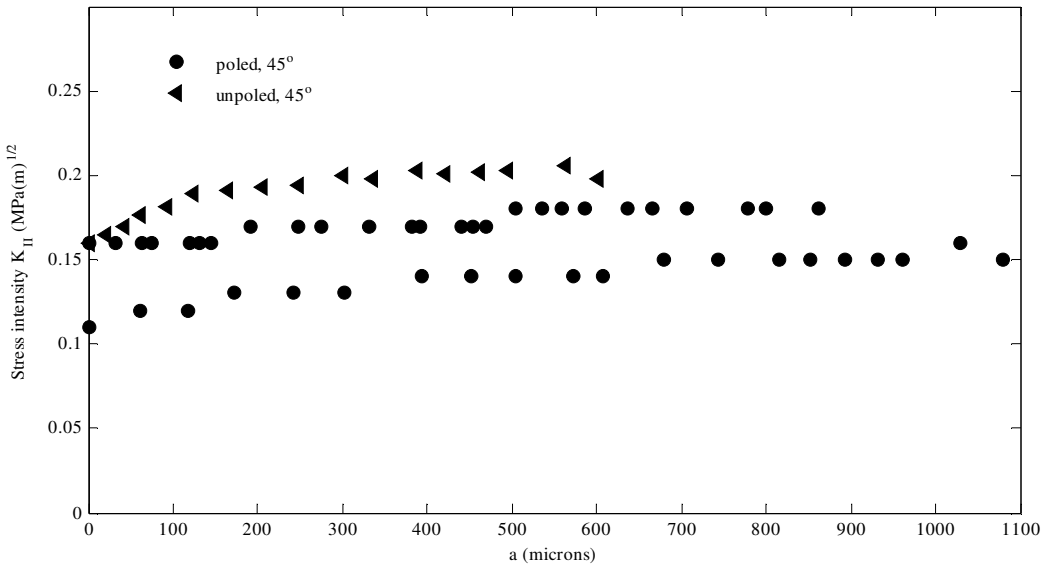

Figure 6.9: Mode II fracture resistance for SEVNB PZN-4.5%PT single crystal specimens. The data includes the two poled and one unpoled specimen previously shown in Figure 6.8 with cracks growing at an angle of 45°.

Analysis

Crystal Anisotropy

Material anisotropy in PZN-4.5%PT single crystals creates a significant departure from the crack tip field behavior in isotropic materials. An accurate description of material anisotropy is required to determine the local and global energy release rate and the crack tip toughness. First, a brief review of crystal anisotropy and how it is related to domain structures in PZN-4.5%PT is given.

The crystal symmetry of PZN-4.5%PT is rhombohedral *3m*. In the unpoled state, an equal volume fraction of eight polarization variants is oriented towards the corners of the unit cell. When the specimen is poled in the [001] direction, the number of polarization variants is reduced to four variants partially aligned with the applied field (see Figure 1.4). The crystal symmetry in the [001] poled state is typically approximated as pseudo-tetragonal having four domain states. This assumption has recently been questioned by Yin and Cao (2002) who suggest an "effective" crystal symmetry different than tetragonal is present.

Erhart and Cao (1999) theoretically determined that poled crystals may possess effective orthorhombic or monoclinic symmetry. This was later investigated in PZN-4.5%PT single crystal using optical micrographs of domain structures, Yin and Cao (2002). Several crystals were observed to contain a two domain state instead of the volume averaged four domain state. The highest symmetry possible in the two domain state was found to be orthorhombic *mm2*. Monoclinic symmetry is also possible if the ratio of two domain states is different.

The large crystal anisotropy raises a question in how to compare toughness and energy release rates on different crystallographic planes. Previous work has shown that the stress intensity factor is independent of orthotropic material properties in elastic materials, (Sih et al. 1965). This was later extended to piezoelectric materials by Suo et al. (1992). The displacement on the crack face was also theoretically proven to be invariant to crack orientation in anisotropic elastic solids for a given traction on the crack

face, (Qu and Li 1991). The invariance in displacement was experimentally verified using Vickers indentations in the present work, as will be shown in the following section (Figure 6.11). The invariance in energy release rate is also valid in piezoelectric materials, which allows the critical energy release rate to be directly compared on any crystallographic plane without rotation of material tensors. Only knowledge of toughness on each cleavage plane is required.

The material properties measured by Yin and Cao (2002) are used in the present analysis to determine the crack tip fields and critical energy release rate. The unpoled specimens have an equal volume fraction of polarization variants which results in zero piezoelectric effect. In the poled SEVNB specimens, the poling direction is out-of-plane resulting in no piezoelectric coupling in the plane of loading when pseudo-tetragonal symmetry is assumed. The effective orthorhombic symmetry includes coupling between in-plane shear and out-of-plane normal deformation through the elastic constant c_{36} and the piezoelectric shear coupling d_{36}. This requires solving a three-dimensional problem which was not performed in the present analysis. The material coefficients for both pseudo-tetragonal and effective orthorhombic crystal symmetry given by Yin and Cao are presented in Table 6.1 in Voight notation. The difference in fracture properties induced by using the two different sets of material coefficients was evaluated using Stroh's formalism in the following section.

Piezoelectric materials have different elastic coefficients under open circuit and short circuit boundary conditions. Since the experiments were conducted in open circuit,

the elastic coefficients at a constant electric displacement must be used in the poled specimens. No piezoelectric coupling exists in the unpoled specimens, therefore the short circuit modulus can be used in this case.

Table 6.1: Comparison between the elastic tensor at constant electric field in PZN-4.5%PT single crystal. The elastic coefficients are given in GPa units, the piezoelectric coefficients (pm/V), and the dielectric coefficients are multiplied by permittivity of free space, ε_o. The orthorhombic material properties have been rotated by 45° around [001] to directly compare with the tetragonal case, (Yin and Cao 2002).

Effective Orthorhombic (mm2)	Pseudo-Tetragonal (4mm)
$c^{(mm2)E} = \begin{bmatrix} 103 & 96 & 99 & 0 & 0 & -7 \\ 96 & 103 & 99 & 0 & 0 & -7 \\ 99 & 99 & 107 & 0 & 0 & -2 \\ 0 & 0 & 0 & 67.5 & 0.5 & 0 \\ 0 & 0 & 0 & 0.5 & 67.5 & 0 \\ -7 & -7 & -2 & 0 & 0 & 63.5 \end{bmatrix}$	$c^{(4mm)E} = \begin{bmatrix} 111 & 102 & 101 & 0 & 0 & 0 \\ 102 & 111 & 101 & 0 & 0 & 0 \\ 101 & 101 & 105 & 0 & 0 & 0 \\ 0 & 0 & 0 & 64 & 0 & 0 \\ 0 & 0 & 0 & 0 & 64 & 0 \\ 0 & 0 & 0 & 0 & 0 & 63 \end{bmatrix}$
$d^{mm2} = \begin{bmatrix} 0 & 0 & 0 & 0 & 140 & 0 \\ 0 & 0 & 0 & 140 & 0 & 0 \\ -970 & -970 & 2000 & 0 & 0 & 187 \end{bmatrix}$	$d^{4mm} = \begin{bmatrix} 0 & 0 & 0 & 0 & 140 & 0 \\ 0 & 0 & 0 & 140 & 0 & 0 \\ -970 & -970 & 2000 & 0 & 0 & 0 \end{bmatrix}$
$\kappa^{(mm2)\varepsilon} = \begin{bmatrix} 3100 & 0 & 0 \\ 0 & 3100 & 0 \\ 0 & 0 & 5200 \end{bmatrix} \varepsilon_o$	$\kappa^{(4mm)\varepsilon} = \begin{bmatrix} 3100 & 0 & 0 \\ 0 & 3100 & 0 \\ 0 & 0 & 5200 \end{bmatrix} \varepsilon_o$

Fracture Mechanics

Stroh's formalism was implemented to gain insight into the fracture behavior observed in single crystal PZN-4.5%PT. First, the crack tip toughness is determined by fitting the anisotropic crack tip displacement solution to the crack opening profile measurements. The difference in anisotropic elastic coefficients given in Table 6.1 is shown to have a minor effect on determining crack tip toughness. The local and global energy release rates are then determined based on the crystal anisotropy given in Table 6.1 together with the crack tip toughness and fracture toughness from the SEVNB method.

Theoretical predictions of the crack profile near the crack tip can be determined using Equation (3.40). It is assumed that bridging stresses are absent on the crack faces in the single crystal specimens, therefore the anisotropic asymptotic crack tip displacement profile can be directly applied to quantify crack tip toughness without the added complexity of weight function analyses, (Seidel and Rödel 1997). The crack opening profile measurements were taken very close to the crack tip to avoid additional higher order terms in the theoretical prediction. The equation describing the crack profile is expanded out in terms of the Stroh eigenvectors given previously by Equation (3.49). The plane strain solution is used in the analysis.

$$u_2(x_1) = -2\sqrt{|x_1|}\,\mathrm{Im}\{A_{21}q_1 + A_{22}q_2 + A_{23}q_3\} \tag{6.1}$$

where A_{2i} (i=1 to 3) are components of the eigenvector solution and q_1 and q_2 are the boundary condition constants. The origin of the coordinate system is located at the crack tip with x_1 parallel to the crack face. The imaginary part of the solution is used (in comparison to Equation (3.40)) because x_1<0 on the crack face.

The crack profile predicted from Stroh's formalism was determined using the elastic coefficients from Table 6.1. Figure 6.10 illustrates the difference in crack profiles when *4mm* or *mm2* crystal symmetry is assumed. The crack opening profile prediction is also compared to the isotropic solution using the in-plane modulus (E) and Poisson ratio (ν) from the 4mm symmetry. The crack profile for isotropic materials is given by Equation (6.2). The plane strain solution is employed.

$$u_2(x_1) = K_I \frac{(1-\nu^2)}{E}\sqrt{\frac{8|x_1|}{\pi}} \tag{6.2}$$

The difference in the in-plane shear modulus between isotropic materials and the single crystal produces significant deviations in crack opening profile. Minor differences are observed when *4mm* or *mm2* crystal symmetry is applied. A constant Mode I stress intensity of 0.5 $MPa\sqrt{m}$ was used in Figure 6.10.

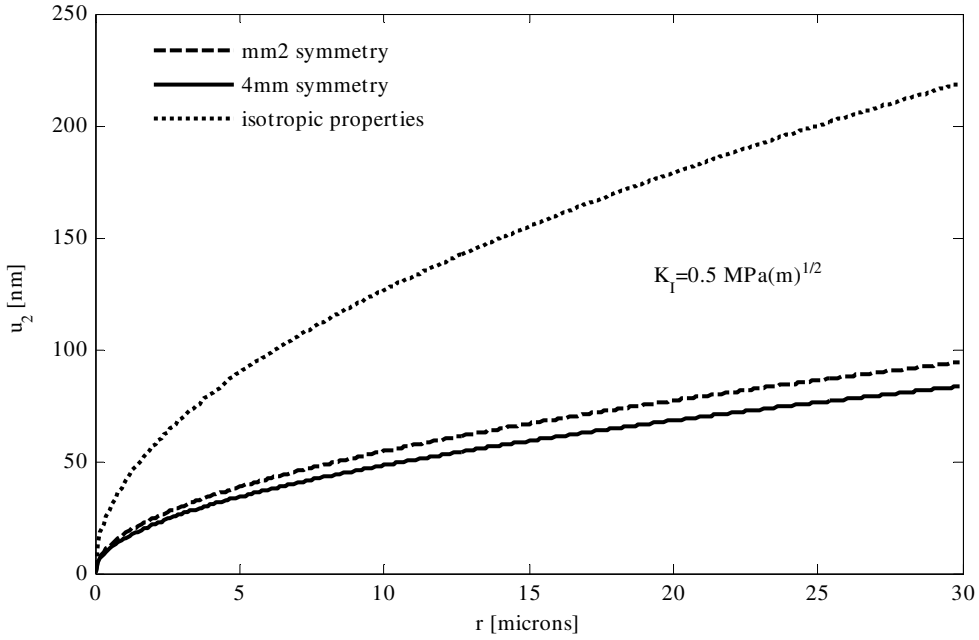

Figure 6.10: Crack profile predictions for pseudo-tetragonal (4mm) and effective orthorhombic (mm2) material properties under the same K_I. A large difference was observed between the anisotropic material properties and the isotropic solution due to the difference in the shear modulus.

The crack opening profile measured from the scanning electron micrographs of Vickers indentations is presented in Figure 6.11. A least squares fit using the anisotropic crack profile prediction for both *4mm* and *mm2* symmetry resulted in an average crack tip toughness ranging between 0.49 $MPa\sqrt{m}$ and 0.53 $MPa\sqrt{m}$. The effective orthorhombic crystal symmetry material properties gave the lower of the two average values.

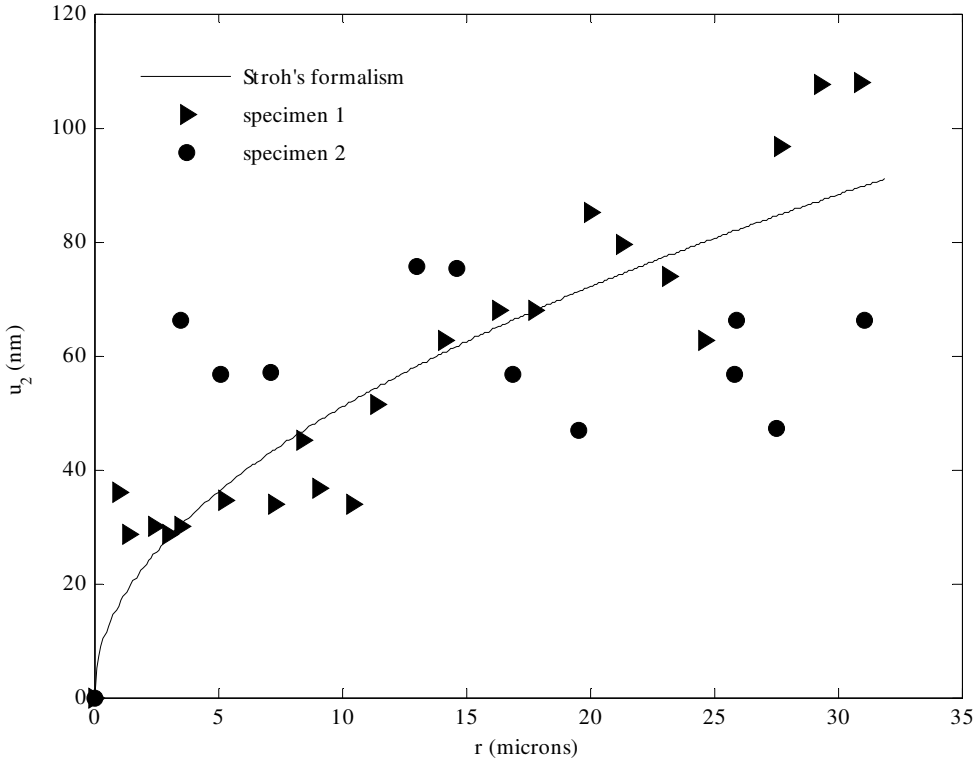

Figure 6.11: Crack tip toughness (K_{tip}) prediction using Stroh's formalism. The Vickers indentation diagonals were aligned in the [110] direction in specimen 1 and in the [100] direction in specimen 2. K_{tip} was predicted to be 0.49 $MPa\sqrt{m}$ assuming *mm2* symmetry and 0.53 $MPa\sqrt{m}$ assuming *4mm* symmetry.

Once the crack tip toughness is known, the local and global energy release rate can be calculated. Details of the energy release rate derivation using Stroh's formalism can be found in the literature (Suo et al. 1992; Ting 1996). The calculation requires computing the Stroh eigenvectors previously given by Equations (3.49) and (3.50). The Irwin matrix can then be computed to determine the energy release rate. The Irwin matrix which was previously given in Chapter II (Equation (2.2)) is given here again,

$$\mathbf{H} = \frac{1}{2}\mathrm{Re}\left\{i\mathbf{A}\mathbf{B}^{-1}\right\} \tag{6.3}$$

where $i = \sqrt{-1}$, and **A** and **B** are the set of eigenvectors in matrix form .

The final equation defining the energy release rate is given by,

$$G = \mathbf{k}^T \mathbf{H}\mathbf{k} \tag{6.4}$$

where $\mathbf{k}^T = \begin{bmatrix} K_{II} & K_I & K_{IV} \end{bmatrix}$ is the stress intensity factors represented in vector form. The Mode IV electric displacement intensity factor was set to zero since the experiments were conducted in open circuit. The critical energy release rate can be determined from the toughness measurements.

The Irwin matrix given by Equation (6.3) is dependent on material properties. The numerical results for the two crystal symmetries for the poled and unpoled state are given in Table 6.2. The off diagonal nonzero terms are due to elastic shear coupling.

Table 6.2: Irwin matrix computed for *mm2* and *4mm* crystal symmetry properties is given in Table 4.2. The units are N, mm, MV. The Irwin matrix for the poled material was computed using open circuit elastic coefficients, while the short circuit modulus was used for the unpoled specimens.

	Effective Orthorhombic (mm2)	Pseudo-Tetragonal (4mm)
Poled material:	$H^{mm2} = \begin{bmatrix} 2.074 & 0.039 & 0 \\ 0.039 & 2.074 & 0 \\ 0 & 0 & -1.914 \end{bmatrix} 10^{-5}$	$H^{4mm} = \begin{bmatrix} 1.904 & 0 & 0 \\ 0 & 1.904 & 0 \\ 0 & 0 & -1.909 \end{bmatrix} 10^{-5}$
Unpoled material:	$H^{mm2} = \begin{bmatrix} 2.161 & 0.093 & 0 \\ 0.093 & 2.161 & 0 \\ 0 & 0 & -1.914 \end{bmatrix} 10^{-5}$	$H^{4mm} = \begin{bmatrix} 1.923 & 0 & 0 \\ 0 & 1.923 & 0 \\ 0 & 0 & -1.909 \end{bmatrix} 10^{-5}$

The local (G_{tip}) and global critical (G_c) energy release rates are computed using the Irwin matrices in Table 6.2 together with the crack tip toughness and fracture toughness from the SEVNB experiments, respectively. The nominal value for G_{tip} was determined to range between 4.98 N/m and 5.35 N/m for *mm2* and *4mm* crystal symmetry, respectively. The global energy release rate along the [110] and [010] cleavage plane is presented in Table 6.3.

Table 6.3: Comparison of the global critical energy release rate for PZN-4.5%PT assuming pseudo-tetragonal crystal symmetry (*4mm*) and effective orthorhombic symmetry (*mm2*). The units are given in J/m^2.

Specimen	crack angle	G_c (*4mm*)	G_c (*mm2*)
poled	0^o	8.55	9.32
unpoled	0^o	8.91	10.04
poled	45^o	4.29	4.73
unpoled	45^o	5.92	6.67

Discussion

Minimal R-curve behavior was observed in the SEVNB fracture experiments. R-curve behavior in ferroelectric materials has been predominantly attributed to ferroelastic switching of local polarization variants. This behavior results in local residual stress in the crack wake that shield the crack tip from external loading. In the [001] cut, the rhombohedral crystal structure is stable under mechanical loading, therefore minimal ferroelastic switching is expected in PZN-4.5%PT. This does not necessarily preclude phase transformations occurring. Liu (2004) has characterized nonlinear stress / strain behavior in poled [001] cut PZN-4.5%PT under large compressive loading in the direction of polarization. Under this loading configuration, the polarization variants most likely rotate from the [111] direction to the [001] (tetragonal phase), [110] (orthorhombic phase) or some intermediate monoclinic phase. More work is required to quantify which phase(s) are present. Upon unloading, the nonlinear deformation was recovered. This

intimates that the phase transformation was unstable. A similar response is expected under tensile loading near a crack tip. As the crack forms and propagates, the lack of remanent strain in the crack wake gives rise to minimal crack tip shielding, hence minimal R-curve behavior.

A weak cleavage plane was identified along [110]. The local energy release rate (G_{tip}) correlated closely to the global critical energy release rate along the [110] crystal plane although some variability in toughness was observed between each angled crack specimen. The poled specimen shown in Figure 6.6 formed a smooth fracture surface along the [110] plane. This specimen resulted in the lowest fracture toughness for the entire crack length shown in Figure 6.8. In the other poled specimen and the unpoled specimen, some crack branching was observed which most likely contributed to the slightly higher toughness measurement. The out-of-plane coupling may also contribute to uncertainty if an effective orthorhombic symmetry is present. Since the experiments were conducted in open circuit, a large out-of-plane electric field may be induced which will influence the in-plane shear strain through the piezoelectric coefficient d_{36}.

Theoretical predictions of displacement fields in piezoelectric solids produce crack opening profiles that are independent of crystal orientation for the same traction and electric displacement on the crack face. This theoretical prediction fits remarkably well with the crack profile measurements from scanning electron micrographs shown in Figure 6.11.

The weak cleavage plane in PZN-4.5%PT motivates the need for assessing length scales at the domain and crystal structure level. The rhombohedral crystal structure in PZN-4.5%PT gives rise to domain walls along the [001] and [110] plane. Domains form to minimize the total energy of the crystal. Fluctuations in local residual energy near twinned domain structures may give rise to a preferred orientation for crack growth along the [110] plane. In addition, jumps in material properties across the domain wall can lead to large localized electric fields and stress under external loading which may provide a sufficient driving force for cracks to form and propagate on the [110] plane.

Conclusions

A weak cleavage plane was identified in single crystal PZN-4.5%PT. Large fracture anisotropy was observed between cracks growing along the [010] and [110] planes. The local energy release rate was found to correlate reasonably well to the global energy release rate on the [110] plane. This may suggest the reversible phase transformation investigated by Liu (2004) may not occur when cracks grow along the [110] plane. Further analysis is required to quantify how K-fields contribute to phase transformations and domain wall motion.

CHAPTER VII

CONCLUSIONS

The burgeoning development of ferroelectric material systems has resulted in novel aerospace, industrial and biomedical devices. The recent push for implementing active materials in high power systems such as morphing aircraft structures has met resistance due to inherent brittleness. The complexity of ferroelectric fracture is embedded in the number of active coupled mechanisms affecting crack growth. This has motivated the current research in advancing theoretical techniques and characterization of ferroelectric fracture. From this research, the following conclusions have been made:

1. In Chapter III, a new anisotropic elasticity technique was developed that explicitly solves the crack tip fields in terms of material coefficients. The technique was found to be in exact agreement to Stroh's formalism when certain restrictions on material coefficients were met. The technique lead to the realization that a certain ratio of piezoelectric and dielectric material coefficients decoupled electric field induced stress concentrations near a crack tip in piezoelectric materials. It was further demonstrated that if this ratio is adjusted above or below the "idealized" decoupling value, the maximum principal stress increases or decreases directly ahead of the crack tip.

2. Chapter IV extends anisotropic elasticity to include the effects of inhomogeneities on microfracture. Recent microstructural material characterizations have verified material inhomogeneities in PZT (Hoffman et al. 2001). Additionally, microfracture has been observed after electric field loading (Tan and Shang 2002; Wang et al. 1998). This prompted the development of a theoretical model that predicts microfracture from variations in piezoelectric material properties. The model applied local field concentrations from an elliptical inclusion to an edge crack extending into the piezoelectric matrix material with dissimilar properties. A positive driving force was determined when a local 4% change in PZT composition was considered based on material coefficients given by Jaffe et al. (1971). This suggests microfracture may occur in ferroelectric actuators even if an external compressive load is applied. The work reemphasized the need to include permeable crack face boundary conditions. When the "un-physical" impermeable crack was employed, a negative driving force for crack growth under an applied electric field was determined.

3. In Chapter V, critical mechanisms affecting subcritical crack growth in PZT were characterized over the accessible velocity range ($v=10^{-9}$ to 10^{-4} m/s). A technique was adopted to ensure a unique v-K (velocity vs. toughness) curve was measured on PZT compact tension specimens. This required attainment of steady state toughness prior to recording v-K behavior. It was experimentally shown that electric boundary conditions and environmental effects can lead to changes in fracture toughness. The short circuit boundary conditions lead to over an order of

magnitude increase in crack tip velocity relative to open circuit conditions in thickness poled compact tension specimens for the same applied K. In the unpoled specimens, ambient environmental conditions (relative humidity≅35%, temperature≅23°C) lead to approximately an order magnitude increase in crack tip velocity relative to very "dry" conditions (relative humidity≅0.02%, temperature≅23°C) for the same applied K. Heat treatment prior to testing played a role in increasing the toughness in "dry" air. A heat treatment temperature above the Curie temperature was required to increase toughness which suggests the ferroelectric to paraelectric phase transformation plays a role in removal of physically or chemically absorbed water molecules in the material.

4. Chapter VI explored fracture mechanisms in the ferroelectric relaxor single crystal PZN-4.5%PT. A weak cleavage plane along the [110] direction was identified from Single Edge V-Notch Bend (SEVNB) specimens. A comparison of the energy release rate for cracks propagating along [110] showed that toughness was nearly half the value of the toughness on the [010] crystallographic plane. Scanning electron micrographs of Vickers indentations were used to determine crack tip toughness and the local energy release rate (G_{tip}). The global energy release rate on the [110] plane was determined to be close to the G_{tip} value. The local energy release rate and crack tip toughness were independent of the crack orientation for [010] and [110] directions which was found to be consistent with theoretical predictions from anisotropic elasticity.

OPEN ISSUES

The theoretical analyses have identified several important mechanisms contributing to fracture in ferroelectric material, although several open issues remain. The orthotropic rescaling identified a certain ratio of dielectric and piezoelectric coefficients decouple stress concentrations from electric field concentrations near a crack tip. A ferroelectric composition that closely matches these properties has not been identified. More work is required to determine if such a material exists. Heterogeneities were shown to influence microfracture. A positive driving force was determined for a certain fluctuation in material properties between an inclusion and matrix. The dissimilar material properties used in the model were based macroscopic properties with small changes in composition. Determining local material properties is challenging due to variation in process variables, inhomogeneous switching, local phase transformations, and other extraneous variables. Although good progress has recently been made in determining local material behavior on a crystal surface using AFM, new theoretical techniques will be useful in predicting material heterogeneity in the bulk material.

Fracture characterization of ferroelectric ceramics and single crystals lead to identifying several important mechanisms that reduce the toughness. Environmental effects were shown to reduce the fracture toughness in PZT PIC 151. Heat treatment above the Curie temperature was required to achieve higher toughness after the material cooled back to room temperature. This presents a challenge in poling the material for actuator use. Less free charge carriers are expected to be available in a dry environment

which makes the poling procedure more difficult. A better understanding of the role that the ferroelectric to paraelectric phase transformation plays in removing water previously absorbed in the ceramic may be useful in obtaining higher toughnesss. Higher toughness was also observed in open circuit. This electric boundary condition introduced a depolarization field which will require three dimensional nonlinear analyses which has not been done. Fracture toughness of single crystal PZN-4.5%PT was found to be lower than PZT. Phase transformations and crystal structure are believed to affect the fracture toughness. R-curve behavior of other single crystal compositions should be characterized to determine if higher toughness exists in a composition with similar enhanced piezoelectric coupling. This will be important in developing reliable single crystal devices.

APPENDIX A

PLANE STRAIN COEFFICIENTS

A set of plane strain coefficients were used to directly compare the orthotropy rescaling technique to the Stroh formalism in Chapter II. The coordinate axis is assumed to be aligned with the material coordinates. For transverse isotropic piezoelectric materials poled in the two direction, the constitutive law is written in the following form.

$$\begin{bmatrix}\gamma_1\\ \gamma_2\\ \gamma_3\\ \gamma_4\\ \gamma_5\\ \gamma_6\end{bmatrix} = \begin{bmatrix} s_{11}^D & s_{12}^D & s_{13}^D & 0 & 0 & 0\\ s_{12}^D & s_{22}^D & s_{12}^D & 0 & 0 & 0\\ s_{13}^D & s_{12}^D & s_{11}^D & 0 & 0 & 0\\ 0 & 0 & 0 & s_{66}^D & 0 & 0\\ 0 & 0 & 0 & 0 & s_{55}^D & 0\\ 0 & 0 & 0 & 0 & 0 & s_{66}^D \end{bmatrix}\begin{bmatrix}\sigma_1\\ \sigma_2\\ \sigma_3\\ \sigma_4\\ \sigma_5\\ \sigma_6\end{bmatrix} + \begin{bmatrix} 0 & g_{21} & 0\\ 0 & g_{22} & 0\\ 0 & g_{21} & 0\\ g_{16} & 0 & 0\\ 0 & 0 & 0\\ 0 & 0 & g_{16}\end{bmatrix}\begin{bmatrix}D_1\\ D_2\\ D_3\end{bmatrix} \tag{A1}$$

$$\begin{bmatrix}E_1\\ E_2\\ E_3\end{bmatrix} = -\begin{bmatrix} 0 & 0 & 0 & 0 & 0 & g_{16}\\ g_{21} & g_{22} & g_{21} & 0 & 0 & 0\\ 0 & 0 & 0 & g_{16} & 0 & 0\end{bmatrix}\begin{bmatrix}\sigma_1\\ \sigma_2\\ \sigma_3\\ \sigma_4\\ \sigma_5\\ \sigma_6\end{bmatrix} + \begin{bmatrix} \beta_{11}^\sigma & 0 & 0\\ 0 & \beta_{22}^\sigma & 0\\ 0 & 0 & \beta_{11}^\sigma\end{bmatrix}\begin{bmatrix}D_1\\ D_2\\ D_3\end{bmatrix} \tag{A2}$$

The following effective elastic constants were used in the orthotropic rescaling for the plane strain problem, where the plane of interest is (x_1, x_2). All other material coefficients were equivalent to the plane stress case.

$$s_{11}^{D'} = s_{11}^{D} - \frac{s_{13}^{D} s_{13}^{D}}{s_{11}^{D}} \tag{A3}$$

$$s_{22}^{D'} = s_{22}^{D} - \frac{s_{12}^{D} s_{12}^{D}}{s_{11}^{D}} \tag{A4}$$

$$s_{12}^{D'} = s_{12}^{D} - \frac{s_{12}^{D} s_{13}^{D}}{s_{11}^{D}} \tag{A5}$$

$$g_{22}^{'} = g_{22} - \frac{s_{12}^{D}}{s_{11}^{D}} g_{21} \tag{A6}$$

$$g_{21}^{'} = g_{21} - \frac{s_{13}^{D}}{s_{11}^{D}} g_{21} \tag{A7}$$

$$\beta_{22}^{\sigma'} = \beta_{22}^{\sigma} + \frac{g_{21} g_{21}}{s_{11}^{D}} \tag{A8}$$

STROH EIGENSOLUTION

The Stroh eigenvalues/eigenvectors are presented for both the “idealized” case and real set of material properties used in the analysis. For the decoupled case, a degeneracy exists where two of the eigenvalues/eigenvectors are repeated. The boundary

condition constants (corresponding to $K_I = 1\ MPa\sqrt{m}$ and $K_{IV} = 0.001\ C/m^2\sqrt{m}$) is included in the boundary condition constants.

Idealized properties:

$$\begin{aligned} p_1 &= 1.152i \\ p_2 &= 1.152i \\ p_3 &= 0.935i \end{aligned} \tag{A9}$$

$$\mathbf{A} = \begin{bmatrix} -1.51i\times10^{-11} & -1.51i\times10^{-11} & 36.48i\times10^{-11} \\ 1.25\times10^{-11} & 1.25\times10^{-11} & 50.90\times10^{-11} \\ 0.01 & 0.01 & -1.00 \end{bmatrix} \tag{A10}$$

$$\mathbf{B} = \begin{bmatrix} 0.76 & 0.76 & (-5.30+2.20i)\times10^{-13} \\ 0.66i & 0.66i & (-2.40-5.80i)\times10^{-13} \\ 3.34i\times10^{-10} & 3.34i\times10^{-10} & -2.86\times10^{-8} \end{bmatrix} \tag{A11}$$

$$\mathbf{q} = \begin{bmatrix} (96.80+6.17i)\times10^{11} \\ (-96.80-6.17i)\times10^{11} \\ 9.14\times10^{-6}-6.86i\times10^{3} \end{bmatrix} \tag{A12}$$

Actual material properties:

$$
\begin{aligned}
p_1 &= -0.31 + 1.06i \\
p_2 &= 0.31 + 1.06i \\
p_3 &= 1.23i
\end{aligned}
\tag{A13}
$$

$$
\mathbf{A} = \begin{bmatrix}
(0.26 - 1.44i)\times 10^{-11} & (-0.26 - 1.44i)\times 10^{-11} & -0.73i \times 10^{-11} \\
(1.26 - 0.28i)\times 10^{-11} & (1.26 + 0.28i)\times 10^{-11} i & 0.27 \times 10^{-11} \\
0.01 - 0.01i & 0.01 + 0.01i & 0.027
\end{bmatrix}
\tag{A14}
$$

$$
\mathbf{B} = \begin{bmatrix}
0.74 & 0.74 & 0.78 \\
0.19 + 0.64i & -0.19 + 0.64i & 0.63i \\
(-0.93 + 3.45i)\times 10^{-10} & (0.93 + 3.45i)\times 10^{-10} & -3.38 \times 10^{-10}
\end{bmatrix}
\tag{A15}
$$

$$
\mathbf{q} = \begin{bmatrix}
(9.67 - 4.33i)\times 10^{5} \\
(-9.67 - 4.33i)\times 10^{5} \\
-7.42 \times 10^{-10} + 8.27i \times 10^{5}
\end{bmatrix}
\tag{A16}
$$

APPENDIX B

SEVNB ANGLED CRACK GEOMETRIC FUNCTIONS

The geometric functions for mixed mode fracture in SEVNB specimens are given in Table A1. The notch radius was 20 μm. The stress intensity factors were determined using the following equations.

$$K_I = F_I \sigma \sqrt{\pi a} \tag{B1}$$

$$K_{II} = F_{II} \sigma \sqrt{\pi a} \tag{B2}$$

where a is the crack length from the edge of the notch and σ is the bending stress at the top of the bend bar.

$$\sigma = \frac{3(S_1 - S_2)}{2W^2 B} F \tag{B3}$$

The bending stress is defined by the load F, the specimen width B, the height W, and the outer and inner loading spans S_1 and S_2, respectively.

Table B1: Geometric functions determined using FRANCD2D for the 45° crack orientation in the SEVNB specimens.

a (mm)	$a+a_N$	$(a+a_N)/W$	F_I	F_{II}
0.12	1.54	0.41	3.45	1.14
0.20	1.62	0.43	2.81	0.98
0.30	1.72	0.45	2.42	0.87
0.40	1.82	0.48	2.20	0.79
0.50	1.92	0.51	2.08	0.75
0.60	2.02	0.53	2.01	0.72
0.75	2.17	0.57	1.96	0.69
0.90	2.32	0.61	1.96	0.68
1.05	2.47	0.65	2.00	0.68
1.20	2.62	0.69	2.06	0.70

REFERENCES

Annual Book of ASTM Standards. (1979). American Society for Testing and Materials, Philadelphia, PA, 3.01, E-399-83 480-504.

IEEE Standard on Piezoelectricity. (1987). The Institute of Electrical and Electronic Engineers, Inc., New York.

Anstis, G. R., Chantikul, P., Lawn, B. R., and Marshall, D. B. (1981). "A Critical Evaluation of Indentation Techniques for Measuring Fracture Toughness: I, Direct Crack Measurements." *J. Am. Ceram. Soc.*, 64(9), 533-538.

Barnett, D. M., and Lothe, J. (1973). "Synthesis of the sextic and the integral formalism for dislocations, Greens function and surface waves in anisotropic elastic solids." *Phys. Norv.*, 7, 13-19.

Bechet, A. (2003). *Ultrasonic detection of debonding within a gradient enhanced piezoelectric actuator (GEPAC)*, Masters Thesis. The Georgia Institute of Technology, Atlanta, GA.

Benveniste, Y. (1994). "Exact Results Concerning the Local Fields and Effective Properties in Piezoelectrtic Composites." *Trans. of the ASME*, 116, 260-267.

Braun, L. M., Bennison, S. J., and Lawn, B. R. (1992). "Objective Evaluation of Short-Crack Toughness Curves Using Indentation Flaws: Case Study on Alumina-Based Ceramics." *J. Am. Ceram. Soc.*, 75(11), 3049-3057.

Budiansky, B., Hutchinson, J. W., and Lambropoulos, J. C. (1983). "Continuum Theory of Dilatant Transformation Toughening in Ceramics." *Int. J. Solids Structures*, 19(4), 337-355.

Chen, W., Lupascu, D. C., Rödel, J., and Lynch, C. S. (2001). "Short Crack R-curves in Ferroelectric and Electrostrictive PLZT." *J. Am. Ceram. Soc.*, 84(3), 593-597.

Cho, Y., Fujimoto, K., Hiranaga, Y., Wagatsuma, Y., Onoe, A., Terabe, K., and Kitamura, K. (2003). "Terabit inch-2 ferroelectric data storage using scanning nonlinear dielectric microscopy nanodomain engineering system." *Nanotechnology*, 14, 637-642.

Christoffel, J. (2002). "Ceramic Muscle." *Automot. Eng.*, 27(1), 52-54.

Cleveland, J. J., and Bradt, R. C. (1978). "Grain Size/Microcracking Relations for Pseudobrookite Oxides." *J. Am. Ceram. Soc.*, 61(11-12), 478-481.

Cunefare, K. A., and Graf, A. J. (2002). "Experimental active control of automotive disc brake rotor squeal using dither." *J. Sound Vib.*, 250(4), 579-590.

Dunn, M., and Wienecke, H. A. (1996). "Green's functions for Transversely Isotropic Piezoelectric Solids." *Int. J. Solids Structures*, 33(30), 4571-4581.

Erhart, J., and Cao, W. (1999). "Effective material properties in twinned ferroelectric crystals." *J. Appl. Phys.*, 86(2), 1073-1081.

Erhart, J., and Cao, W. (2003). "Permissible symmetries of multi-domain configurations in perovskite ferroelectric crystals." *J. Appl. Phys.*, 94(5), 3436-3445.

Evans, A. G. (1978). "Microfracture from Thermal Expansion Anisotropy - I. Single Phase Systems." *Acta. Metall. Mater.*, 26, 1845-1853.

Fang, F., and Yang, W. (2002). "Indentation-induced cracking and 90^o domain switching pattern in barium titanate ferroelectric single crystals under different poling." *Mater. Lett.*, 57, 198-202.

Fett, T., Kamlah, M., Munz, D., and Thun, G. (2000). "Strength of a PZT ceramic under different test conditions." *Proc. SPIE--Inter. Soc. Opt. Eng.*, 3992, 197-208.

Förderreuther, A., Thurn, G., Zimmermann, A., and Aldinger, F. (2002). "R-curve effect, influence of electric field and process zone in $BaTiO_3$ ceramics." *J. Euro. Ceram. Soc.*, 22, 2023-2031.

Freiman, S. W., McKinney, K. R., and Smith, H. L. (1974). "Slow crack growth in polycrystalline ceramics." *Fract. Mech. Ceram.*, 2, 659-676.

Green, D. J. (1983). "Microcracking Mechanisms in Ceramics." *Fract. Mech.Ceram.*, 5, 457-493.

Grunderson, S. A., and Lothe, J. (1987). "A new method for numerical calculation in anisotropic elasticity problems." *Phys. Status Solidi*, B143, 73-85.

Gruverman, A., and Tokumoto, H. (2001). "On the imaging mechanism of ferroelectric domains in scanning force microscopy." *Nano. Lett.*, 1(2), 93-95.

Hao, T. H., and Shen, Z. Y. (1994). "A new electric boundary condition of electric fracture mechanics and its applications." *Eng. Fract. Mech.*, 47, 793-802.

Hayter, A. J. (1996). *Probability and Statistics for Engineers and Scientists*, PWS Publishing Company, Boston, MA.

Hoffman, M. J., Hammer, M., Endriss, A., and Lupascu, D. C. (2001). "Correlation Between Microstructure, Strain Behavior, and Acoustic Emission of Soft PZT Ceramics." *Acta. Mater.*, 49, 1301-1310.

Hosono, Y., Harada, K., Shimanuki, S., Saitoh, S., and Yamashita, Y. (1999). "Crystal growth and mechanical properties of Pb[(Zn1/3Nb2/3)0.91Ti0.09< /sub>]O3 single crystal produced by solution Bridgman method." *Jpn. J. Appl. Phys.*, 38(9B), 5512-5515.

Hwang, S. C., Huber, J. E., McMeeking, R. M., and Fleck, N. A. (1998). "The simulation of switching in polycrystalline ferroelectric ceramics." *J. Appl. Phys.*, 84(3), 1530-1540.

Hwang, S. C., Lynch, C. S., and McMeeking, R. M. (1995). "Ferroelectric/Ferroelastic Interactions and a Polarization Switching Model." *Acta. Metall. Mater.*, 43, 2073.

Jaffe, Cook, and Jaffe. (1971). *Piezoelectric Ceramics*, Academic Press Inc., London.

Jiang, Q., Subbarao, E. C., and Cross, L. E. (1994). "Grain Size Dependence of Electric Fatigue Behavior of Hot Pressed PLZT Ferroelectric Ceramics." *Acta. Metall. Mater.*, 42(11), 3687-3694.

Kamlah, M. (2001). "Ferroelectric and ferroelastic piezoceramics-modeling of electromechanical hysteresis phenomena." *Continuum Mech. Thermodyn.*, 13, 29-268.

Karastamatis, T., Lupascu, D. C., Lucato, S. L., Rödel, J., and Lynch, C. S. (2002). "R-curves of lead zirconate titanate (PZT)." *J. Euro. Ceram. Soc.*, 23, 1401-1408.

Knechtel, M. C., Garcia, D. E., Rödel, J., and Claussen, N. (1993). "Subcritical crack growth in Y-TZP and Al_2O_3-toughened Y-TZP." *J. Am. Ceram. Soc.*, 76(10), 2681-2684.

Kolleck, A., Schneider, G. A., and Meschke, A. (2000). "R-curve behavior of $BaTiO_3$ and PZT ceramics under the influence of an electric field appied parallel to the crack front." *Acta. Mater.*, 48, 4099-4113.

Kübler, J. (1997). "Fracture Toughness of Ceramics Using the SEVNB Method: Preliminary Results." *Ceram. Eng. Sci. Proc.*, 18(4), 155-162.

Lange, F. F. (1978). "Fracture Mechanics and Microstructural Design." *Fracture Mechanics of Ceramics*, 4, 799-819.

Lawn, B. (1975). *Fracture of Brittle Solids*, Cambridge University Press, Cambridge, UK.

Liang, J., Han, J., Wang, B., and Du, S. (1995). "Electroelastic modelling of anisotropic piezoelectric materials with an elliptic inclusion." *Int. J. Solids Structures*, 32(20), 2989-3000.

Lines, M. E., and Glass, A. M. (1977). *Principles and Applications of Ferroelectric and Related Materials*, Clarendon Press, Oxford.

Liu, S.-F., Park, S.-E., Shrout, T. R., and Cross, L. E. (1999). "Electric field dependence of piezoelectric properties for rhombohedral $0.955Pb(Zn_{1/3}Nb_{2/3})O_3$-$0.045PbTiO_3$ single crystals." *J. Appl. Phys*, 85(5), 2810-2814.

Liu, T. (2004). unpublished data.

Liu, T., and Lynch, C. S. (2003). "Ferroelectric properties of [110], [001], and [111] poled relaxor single crystals: measurements and modeling." *Acta. Mater.*, 51, 407-416.

Liu, T., Oates, W. S., Wan, S., and Lynch, C. S. (2004). "Effect of partial electrodes on the fracture of ferroelectric relaxor single crystal PZN-4.5%PT." *submitted to J. Intel. Mat. Syst. Str.*

Lucato, S. L. (2003). "Crack growth velocity dependent R-curve behavior in lead zirconate titanate." *J. Am. Ceram. Soc.*, 86(6), 1037-1039.

Lucato, S. L., Lupascu, D. C., and Rödel, J. (2000). "Effect of poling direction on R-curve behavior in lead zirconate titantate." *J. Am. Ceram. Soc.*, 83(2), 424-426.

Lupascu, D. C., Kreuzer, M., Lucato, S. L., Rödel, J., and Lynch, C. S. (2001). "A Liquid Crystal Display of Stress Fields in Ferroelectrics." *Appl. Phys. Lett.*, 78(17), 2554-2556.

Lynch, C. S. (1996). "The effect of uniaxial stress on the electro-mechanical response of 8/65/38 PLZT." *Acta. Mater.*, 44(10), 4137-4148.

Lynch, C. S. (1998). "Fracture of Ferroelectric and Relaxor Electro-ceramics: Influences of Electric Field." *Acta. Mater.*, 46(2), 599-608.

Lynch, C. S., and Oates, W. S. (2004). "Orthotropic Rescaling for Crack Tip Fields in Linear Piezoelectric Materials." *Int. J. Solids Structures*, in press.

Malvern, L. E. (1969). *Introduction to the Mechanics of a Continuous Medium*, Prentice-Hall, Inc., Up Saddle River, NJ 07458.

Mani, R., Lagoudas, D. C., and Rediniotis, O. K. (2003). "MEMS based Active Skin for Turbulent Drag Reduction." *proc. of SPIE*, 5056, 9-20.

Maugin, G. A., and Epstein, M. (1991). "The electroelastic energy-momentum tensor." *Proc. R. Soc. Lond. A*, 433, 299-312.

McHenry, K. D., and Koepke, B. G. (1983). "Electric Field Effects on Subcritical Crack Growth in PZT." *Fract. Mech. Ceram.*, 5(337-352).

McLaughlin, B., Liu, T., and Lynch, C. S. (2004). "Relaxor ferroelectric PMN-32%PT crystals under stress and electric field loading: I-32 mode measurements." *Acta. Mater.*, in press.

McMeeking, R. M. (1999). "Crack tip energy release rate for a piezoelectric compact tension specimen." *Eng. Fract. Mech.*, 64, 217-244.

McMeeking, R. M. (2003). "The energy release rate for a Griffith crack in a piezoelectric material." *Eng. Fract. Mech.*, 71(7-8), 1169-1183.

McMeeking, R. M., and Evans, A. G. (1981). "Mechanics of Transformation-Toughening in Brittle Materials." *J. Am. Ceram. Soc.*, 65(5), 242-246.

McMeeking, R. M., and Ricoeur, A. (2003). "The weight function for cracks in piezoelectrics." *Int. J. Solids Structures*, 40, 6143-6162.

Moon, R., Bowman, K., Trumble, K., and Rödel, J. (2000). "Comparison of R-curves from Single-Edge V-Notched Beam (SEVNB) and Surface-Crack-in-Flexure (SCF) Fracture-Toughness Tests Methods on Multilayer Alumina-Zirconia Composites." *J. Am. Ceram. Soc.*, 83(2), 445-447.

Moulson, A. J., and Herbert, J. M. (1990). *Electroceramics*, Chapman & Hall, London, UK.

Munz, D., and Fett, T. (1999). *Ceramics: Mechanical Properties, Failure Behaviour, Materials Selection*, Springer-Verlag, Berlin, Germany.

Njiwa, A. B. K. (2003). unpublished data.

Noheda, B., Zhong, Z., Cox, D. E., Shirane, G., Park, S.-E., and Rehrig, P. (2002). "Electric-field-induced phase transitions in rhombohedral $Pb(Zn_{1/3}Nb_{2/3})_{1-x}Ti_xO_3$." *Phys. Rev. B*, 65, 224101-1-224101-7.

Oates, W. S. (2001). *Piezoelectric Pump Design and System Dynamic Model*, Masters Thesis. The Georgia Institute of Technology, Atlanta, GA.

Oates, W. S., Lynch, C. S., Lupascu, D. C., Njiwa, A. B. K., Aulbach, E., and Rödel, J. (2004). "Subcritical Crack Growth in Lead Zirconate Titanate." *J. Am. Ceram. Soc.*, in press.

Panofsky, W. K. H., and Phillips, M. (1962). *Classical Electricity and Magnetism*, Addison-Wesley Publishing Company, Inc., Reading, MA.

Park, S. B., and Sun, C. T. (1995). "Effect of electric field on fracture of piezoelectric ceramics." *Int. J. Fracture*, 70, 203-216.

Park, S.-E., and Shrout, T. R. (1997). "Ultrahigh strain and piezoelectric behavior in relaxor based ferroelectric single crystals." *J. Appl. Phys.*, 82(4), 1804-1811.

Qu, J., and Li, Q. (1991). "Interfacial dislocation and its application to interface crack in anisotropic bimaterials." *J. Elasticity*, 26, 167-195.

Randall, C. A., Kim, N., Kucera, J.-P., Cao, W., and Shrout, T. R. (1998). "Intrinsic and Extrinsic Size Effects in Fine-Grained Morphotropic-Phase-Boundary Lead Zirconate Titanate Ceramics." *J. Am. Ceram. Soc.*, 81(3), 677-688.

Reich, G. W., and Sanders, B. (2003). "Structural Shape Sensing for Morphing Aircraft." *proc. of SPIE*, 5056, 134-141.

Rice, J. R. (1972). "Some Remarks on Elastic Crack-Tip Stress Fields." *Int. J. Solids Structures*, 8, 751-758.

Rice, R. W., and Phohanka, R. C. (1978). "Grain-size Dependence of Spontaneous Cracking in Ceramics." *J. Am. Ceram. Soc.*, 62, 559-563.

Roberts, D. C., Hagood, N. W., Su, Y.-H., Li, H., and Carretero, J. A. (2000). "Design of a piezoelectrically-driven hydraulic amplification microvalve for high pressure, high frequency applications." *proc. of SPIE*, 3985, 616-628.

Rödel, J., Kelly, J. F., Stoudt, M. R., and Bennison, S. J. (1991). "A Loading Device for Fracture Testing of Compact Tension Specimen in the SEM." *Scanning Microscopy*, 5(1), 29-35.

Sabolsky, E. M., Trolier-McKinstry, S., and Messing, G. L. (2003). "Dielectric and piezoelectric properties of <001> fiber-textured $0.675Pb(Mg_{1/3}Nb_{2/3})O_3$-$0.325PbTiO_3$ ceramics." *J. Appl. Phys.*, 93(7), 4072-4080.

Schneider, G. A., Felten, F., and McMeeking, R. M. (2003). "The electrical potential difference across cracks in PZT measured by Kelvin Probe Microscopy and the implications for fracture." *Acta. Mater.*, 51, 2235-2241.

Schuh, C., Steinkopff, T., Wolff, A., and Lubitz, K. (2000). "Piezoceramic multilayer actuators for fuel injection systems in automotive area." *proc. of SPIE*, 3992, 165.

Seidel, J., and Rödel, J. (1997). "Measurement of Crack Tip Toughness in Alumina as a Function of Grain Size." *J. Am. Ceram. Soc.*, 80(2), 433-438.

Shang, J. K., and Tan, X. (2001). "Indentation-induced Domain Switching in $Pb(Mg_{1/3}Nb_{2/3})O_3$-$PbTiO_3$ Crystal." *Acta. Mater.*, 49, 2993-2999.

Sih, G. C., Paris, P. C., and Irwin, G. R. (1965). "On cracks in rectilinearly anisotropic bodies." *Int. J. Fracture Mech.*, 1, 189-203.

Stech, M., and Rödel, J. (1996). "Method for Measuring Short-Crack R-Curves without Calibration Parameters: Case Studies on Alumina and Alumina/Aluminum Composites." *J. Am. Ceram. Soc.*, 79(2), 291-297.

Stroh, A. N. (1958). "Dislocations and cracks in anisotropic elasticity." *Phil. Mag.*, 7, 625-646.

Suo, Z., Bao, G., Fan, B., and Wang, T. C. (1991). "Orthotropy Rescaling and Implications for Fracture in Composites." *Int. J. Solids Structures*, 28(2), 235-248.

Suo, Z., Kuo, C.-M., Barnett, D. M., and Willis, J. R. (1992). "Fracture Mechanics for Piezoelectric Ceramics." *J. Mech. Phys. Solids*, 40(4), 739-765.

Tan, X., and Shang, J. K. (2002). "In situ transmission electron microscopy study of electric-field-induced grain boundary cracking in lead zirconate titanate." *Phil. Mag. A.*, 82(8), 1463-1478.

Tan, X., Xu, Z., and Shang, J. K. (2000). "Direct observations of electric field-induced domain boundary cracking in <001> oriented piezoelectric $Pb(Mg_{1/3}Nb_{2/3})O_3$-$PbTiO_3$ single crystal." *Appl. Phys. Lett.*, 77(10), 1529-1531.

Ting, T. C. T. (1996). *Anisotropic Elasticity*, Oxford University Press, New York.

Tobin, A. G., and Pak, E. (1993). "Effect of Electric Fields on Fracture Behavior of PZT Ceramics." *Proc. SPIE--Inter. Soc. Opt. Eng.*, 1916, 78-86.

Valasek, J. (1921). "Piezo-electric and Allied Phenomena in Rochelle Salt." *Phys. Rev.*, 17, 475-481.

van der Laag, N. J., Dortmans, L. J. M. G., and de With, G. (2002). "Influence of relative humidity on mechanical properties of alumina, PZT, and zirconia." *Key Eng. Mat.*, 206-213, 751-754.

Wang, H., and Singh, R. N. (1997). "Crack Propagation in piezoelectric ceramics: Effects on applied electric fields." *J. Appl. Phys.*, 81(11), 7471-7479.

Wang, J., and Landis, C. M. (2004). "On the fracture toughness of ferroelectric ceramics with electric field applied parallel to the crack front." *Acta. Mater.*, accepted for publication.

Wang, Z., Jiang, Q., White, G. S., and Richardson, A. K. (1998). "Processing Flaws in PZT Transducer Rings." *Smart Mater. Struct.*, 7, 867-873.

Weisstein, E. W. (1999). *CRC Concise Encyclopedia of Mathematics*, CRC Press, Boca Raton.

Weitzing, H., Schneider, G. A., Steffens, J., Hammer, M., and Hoffman, M. J. (1999). "Cyclic Fatigue due to Electric Loading in Ferroelectric Ceramics." *J. Euro. Ceram. Soc.*, 19, 1333-1337.

Wiederhorn, S. M. (1974). "Subcritical crack growth in ceramics." *Fract. Mech. Ceram.*, Plenum Publishing Corporation, New York, 613-646.

Wiederhorn, S. M., Freiman, S. W., Fuller Jr., E. R., and Simmons, C. J. (1982). "Effects of water and other dielectrics on crack growth." *J. Mat. Sci.*, 17, 3460-3478.

Wiederhorn, S. M., Fuller Jr., E. R., and Thomson, R. (1980). "Micromechanims of crack growth in ceramics and glasses in corrosive environments." *Met. Sci.*, 14, 450-458.

Xiao, Z. M., and Bai, J. (1999). "On piezoelectric inhomogeneity related problem--part I: a closed-form solution for the stress field outside a circular piezoelectric inhomogeneity." *Int. J. Eng. Sci.*, 37, 945-959.

Xu, Z., Tan, X., and Shang, J. K. (2000). "In situ transmission electron microscopy study of electric-field-induced microcracking in single crystal $Pb(Mg_{1/3}Nb_{2/3})O_3$-$PbTiO_3$." *Appl. Phys. Lett.*, 76(25), 3732-3734.

Yi, J. W., Shih, W. Y., Mutharasan, R., and Shih, W.-H. (2003). "In situ cell detection using piezoelectric lead zirconate-stainless steel cantilevers." *J. Appl. Phys.*, 93(1), 619-625.

Yin, J., and Cao, W. (2002). "Effective macroscopic symmetries and materials properties of multidomain $0.955Pb(Zn_{1/3}Nb_{2/3})O_3$-$0.045PbTiO_3$ single crystals." *J. Appl. Phys.*, 92(1), 444-448.

Zhang, Q. Q., Gross, S. J., Tadigadapa, S., Jackson, T. N., Djuth, F. T., and Trolier-McKinstry, S. (2003). "Lead zirconate titanate films for d_{33} mode cantilever actuators." *Sensors and Actuators A*, 105, 91-97.

Zhang, T.-Y., Zhao, M., and Tong, P. (2001). "Fracture of Piezoelectric Ceramics." *Adv. Appl. Mech.*, 38, 147-289.

Zhang, Z., and Raj, R. (1995). "Influence of Grain Size on Ferroelastic Toughening and Piezoelectric Behavior of Lead Zirconate Titanate." *J. Am. Ceram. Soc.*, 78(12), 3363-3368.